Sheffield
Hallam
University

Development of nanostructured PVD coatings for total knee replacement joints using HIPIMS.

SUGUMARAN, Arunprabhu A.

Available from the Sheffield Hallam University Research Archive (SHURA) at:

http://shura.shu.ac.uk/19288/

A Sheffield Hallam University thesis

This thesis is protected by copyright which belongs to the author.

The content must not be changed in any way or sold commercially in any format or medium without the formal permission of the author.

When referring to this work, full bibliographic details including the author, title, awarding institution and date of the thesis must be given.

Please visit http://shura.shu.ac.uk/19288/ and http://shura.shu.ac.uk/information.html for further details about copyright and re-use permissions.

Adsetts Centre, City Campus
Sheffield S1 1WD

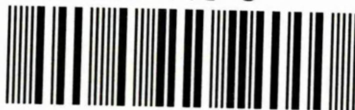

Sheffield Hallam University
Learning and Information Services
Adsetts Centre, City Campus
Sheffield S1 1WD

REFERENCE

ProQuest Number: 10694168

All rights reserved

INFORMATION TO ALL USERS
The quality of this reproduction is dependent upon the quality of the copy submitted.

In the unlikely event that the author did not send a complete manuscript
and there are missing pages, these will be noted. Also, if material had to be removed,
a note will indicate the deletion.

ProQuest 10694168

Published by ProQuest LLC (2017). Copyright of the Dissertation is held by the Author.

All rights reserved.
This work is protected against unauthorized copying under Title 17, United States Code
Microform Edition © ProQuest LLC.

ProQuest LLC.
789 East Eisenhower Parkway
P.O. Box 1346
Ann Arbor, MI 48106 – 1346

Development of Nanostructured PVD Coatings for Total Knee Replacement Joints using HIPIMS

Arunprabhu Arunachalam Sugumaran

A thesis submitted in partial fulfilment of the requirements of Sheffield Hallam University for the degree of Doctor of Philosophy

July 2014

அர்ப்பணிப்பு: பாப்பா, அம்மா மற்றும் அப்பா
To: Jayaselvi, Thangameenakshi and Sugumaran

Acknowledgements

At first, I would like to thank my Director of Studies Prof. Papken Hovsepian for his invaluable guidance and encouragement throughout the course of my studies without which, I would have not been able to produce this piece of work. I would also like to thank Prof. Arutiun Ehiasarian (Supervisor II) for his help in plasma analysis and writing research articles. I am grateful to Dr. Imran Khan (Supervisor II), Director of Research, Biomet, UK for providing me with the test components.

Special thanks to Dr. Yashodhan Purandare for his assistance in handling the PVD system and other analytical instruments. I greatly appreciate Mr. Gary Robinson for his technical support in preparing the test samples. Special thanks to Mr. Daniel Loch also for his help in plasma diagnostics and other useful suggestions.

I acknowledge the MERI for providing me with the lab facilities and financial support to carry out this research work. I thank Mr. Stuart Creasy and Mr. Vinay Patel for their support in handling the electron microscope. I am grateful to all my teachers and professors who helped me to grow up to this stage.

Thanks to fellow MERI members Dr. Vikas Kumar, Ms. Anna Oniszczuk, Dr. Chinh Nguyen, Mr. Sampan Seth, Ms. Paranjayee Mandal, Mr. Thomas Morton, Mr. Stephen Dodds, Mr. Itai Vutabwarova, Mrs. Trinh Pham and Dr. Ganesh Kamath for their support.

It's a pleasure to thank my beloved grandparents for their everlasting love and support. Special thanks to my uncles, Mr. S. Ramachandran, Mr. M. Thangarajan who have been very helpful and supportive throughout my career. I would like to thank my friends Dr. K. Sasipriya and Ms. P. Kiruthika Devi for their moral support. Finally, I would like to thank all my well-wishers.

Abstract

The aim of this study was to develop thin film coatings for total knee replacement joints using high power impulse magnetron sputtering (HIPIMS). An industrial size four cathode magnetron sputtering system equipped with direct current (DC) and HIPIMS power supplies was used for this purpose. Initially, Plasma diagnostics were carried out using optical emission spectroscopy (OES) while sputtering Ti target in Ar + N_2 atmosphere by utilizing various HIPIMS/conventional DCMS (henceforth UBM) source combinations by varying the process parameters such as coil current and N_2 flow. Then, single layer titanium nitride (TiN) coating was deposited by varying the degree of HIPIMS utilisation and the process parameters such as bias voltage and coil current to thoroughly understand the effect of degree of HIPIMS utilisation on the microstructure, residual stress, texture, mechanical, tribological and corrosion properties of such coatings. The degree of HIPIMS utilisation was altered by increasing the number of HIPIMS targets used for the deposition. Four different source combinations were used for this purpose, as follows: 4 cathodes in conventional DCMS mode to deposit pure UBM coating, 1HIPIMS + 3UBM and 2HIPIMS + 2UBM cathodes to deposit combined HIPIMS/UBM coatings and 2HIPIMS cathodes to deposit pure HIPIMS coatings. TiN/NbN, TiCN/NbCN and CrN/NbN multilayer coatings were deposited on CoCr alloy test buttons along with other (HSS, SS and Si) substrates since our intended application is on total knee replacement joints made of CoCr alloy. The knowledge gained by investigating the TiN (Ar + N_2) plasma and the properties of TiN was used to determine the process parameters for depositing the multilayer coatings. X- ray diffraction (XRD) technique was used for calculating the texture, residual stress and bilayer thickness of the coatings. Nanoindentation method was used to determine the nano hardness of the coatings. The adhesion strength of the coatings was estimated by scratch and Rockwell indentation tests. Pin on disc method was used for the tribological studies such as coefficient of friction and coefficient of wear. Surface roughness measurements were carried out using a surface profiler. Microstructural characterisation of the coatings was carried out using scanning electron microscope (SEM) and transmission electron microscope (TEM). Potentiodynamic polarisation method was utilised to study the corrosion performance of the coatings. Raman spectroscopy was used to study the constituents of the corrosion products and evaluate the corrosion damage. OES measurements revealed that the degree of metal ions (Ti^{1+}) increased with increasing degree of HIPIMS utilisation. The hardness, tribological and corrosion properties of TiN coatings improved with increasing degree of HIPIMS utilisation. TiN and multilayer coatings deposited by HIPIMS exhibited a smooth columnar microstructure without any voided region along the column boundaries. TiN/NbN, TiCN/NbCN and CrN/NbN multilayer coatings deposited on CoCr alloy, HSS and SS test buttons exhibited superior mechanical, tribological and corrosion properties as compared to the underlying substrate.

Contents

Acknowledgements .... **I**

Abstract .... **II**

Contents .... **III**

List of Acronyms .... **VII**

Chapter 1 .... **1**

1 Introduction **1**

1.1 Motivation 1

1.1.1 Human knee joint 1

1.1.2 Knee replacement joints 2

1.1.3 Limitations of existing metallic biomedical materials 3

1.2 Surface engineering of implants 4

1.2.1 High Power Impulse Magnetron Sputtering 5

1.3 Present research work 6

1.3.1 Aims & Objectives 6

References 8

Chapter 2 .... **11**

2 Literature Review **11**

2.1 Plasma & Glow discharge 11

2.1.1 Ionisation 12

2.1.2 Excitation 13

2.1.3 Relaxation 13

2.1.4 Recombination 14

2.1.5 Classical DC glow discharge 14

2.2 Thin film deposition techniques 15

2.2.1 Physical Vapour Deposition 15

2.3 Cathodic arc deposition 29

2.4 Microstructure evolution during coating growth 31

2.4.1 Effect of sputtering parameters on microstructure evolution 33

2.5 Nanostructured coatings for implants 38

References 43

Chapter 3 .... **53**

3 Materials and Methods **53**

3.1 Materials, Substrate preparation and deposition of various coatings 53

3.1.1 Substrate materials 53

3.1.2 Substrate preparation prior to coating deposition 54

3.1.3 Industrial size coating machine enabled with HIPIMS technology 54

3.1.4 Protocol followed for the experiments 56

3.1.5 Deposition of TiN coatings 57

3.1.6 Deposition of TiN/NbN multilayer coatings 60

3.1.7 Deposition of TiCN/NbCN multilayer coating 61

3.1.8 Deposition of CrN/NbN multilayer coating 62

3.2 Plasma diagnostics 63

3.3 Thin film characterisation techniques 66

3.3.1 X-ray Diffraction analysis 66

3.3.2 Determination of adhesion strength of thin films 69

3.3.3 Nanohardness measurement 71

3.3.4 Tribological characterisation 73

3.3.5 Determination of surface roughness 75

3.3.6 Energy Dispersive X- ray spectroscopy 76

3.3.7 Microstructural analysis 77

3.3.8 Electrochemical corrosion testing 80

3.3.9 Raman spectroscopy 82

References 85

Chapter 4 .... **88**

4 Results and Discussion **88**

4.1 Plasma analysis using Optical emission spectroscopy 88

4.1.1 Effect of different HIPIMS/UBM source combinations on $\{Ti^{1+}\}$ and $\{Ti^{0}\}$.... 89

4.1.2 Effect of coil current on the degree of metal flux in the plasma generated by utilising different source combinations 90

4.1.3 Effect of N_2 flow on the degree of metal flux and N_2^{0} in the plasma generated by utilising different source combinations 92

4.2 Energy dispersive X-ray spectroscopy analysis 94

4.3 Effect of HIPIMS utilisation on the deposition rate of TiN coatings 98

4.4 Adhesion strength of TiN coatings 99

4.5 Mechanical and tribological properties of TiN coatings 101
4.5.1 Nano-hardness test 101
4.5.2 Coefficient of friction and wear coefficient 102
4.6 Microstructure evolution 106
4.6.1 Effect of the degree of HIPIMS utilisation on the microstructure of TiN coatings 106
4.6.2 Effect of bias voltage on the microstructure of TiN coatings 107
4.6.3 Effect of coil current on the microstructure of TiN coatings 108
4.7 Determination of residual stress in TiN coatings 110
4.7.1 Effect of the degree of HIPIMS utilisation on residual stress in TiN coatings 110
4.7.2 Effect of coil current on residual stress in TiN coatings 112
4.7.3 Effect of bias voltage on residual stress in TiN coatings 114
4.8 Effect of bias voltage on the texture evolution of TiN coatings 118
4.9 Effect of degree of HIPIMS utilisation on the surface roughness of TiN coatings 122
4.10 Effect of the degree of HIPIMS utilisation on corrosion resistance of TiN coatings 124
4.10.1 Potentiodynamic polarisation measurements 124
4.10.2 SEM investigation of corroded samples 125
4.10.3 Raman spectroscopy 126
4.10.4 Transmission electron microscopy 130
4.11 Investigation of corrosion performance of TiN coatings deposited by arc evaporation and HIPIMS techniques 131
4.11.1 Potentiodynamic polarisation measurements of TiN coatings deposited using cathodic arc evaporation and 2HIPIMS + 2UBM source combination....... 132
4.11.2 SEM analysis of TiN coatings deposited by arc evaporation method 134
4.11.3 Raman analysis of TiN coatings deposited by arc evaporation method and combined HIPIMS/UBM coating 137
4.12 Summary of TiN coatings 139
4.13 Characterisation of TiN/NbN multilayer coatings 141
4.13.1 Adhesion strength 141
4.13.2 X-ray diffraction analysis 142
4.13.3 Bilayer thickness 143
4.13.4 Energy dispersive X-ray spectroscopy analysis 144

4.13.5 Microstructure analysis 145
4.13.6 Mechanical and tribological properties 146
4.13.7 Corrosion properties 147
4.14 Characterisation of TiCN/NbCN multilayer coatings 148
4.14.1 X-ray diffraction analysis 148
4.14.2 Bilayer thickness 149
4.14.3 Energy dispersive X-ray spectroscopy analysis 149
4.14.4 Mechanical and tribological properties 150
4.14.5 Corrosion properties 152
4.15 Characterisation of CrN/NbN multilayer coatings 153
4.15.1 Adhesion strength 153
4.15.2 X-ray diffraction analysis 154
4.15.3 Energy dispersive X-ray spectroscopy analysis 155
4.15.4 Microstructure analysis 156
4.15.5 Investigation of thickness distribution across the sample holder 156
4.15.6 Mechanical and tribological properties 158
4.15.7 Corrosion properties 160
4.16 Summary of multilayer coatings 161
References 162
Chapter 5 166
5 Conclusions 166
Future work 171
Scientific Contributions 172

List of Acronyms

PVD	Physical Vapour Deposition
DCMS	Direct Current Magnetron Sputtering
UBM	Unbalanced Magnetron
HIPIMS	High power impulse Magnetron sputtering
TKR	Total Knee joint Replacement
UHMWPE	Ultra-High Molecular Weight Polyethylene
CVD	Chemical Vapour Deposition
E-beam	Electron beam
AC	Alternating Current
RF	Radio Frequency
DLC	Diamond Like Carbon
DI	De-Ionized
HSS	High Speed Steel
SS	Stainless Steel
OES	Optical Emission Spectroscopy
CCD	Charge-Coupled Device
PMT	Photo Multiplier Tube
EDS	Energy Dispersive X-ray Spectroscopy
XRD	X-Ray Diffraction
BB	Bragg-Brentano
GA	Glancing Angle
LA	Low Angle
COF	Coefficient of Friction
COW	Coefficient of Wear
SEM	Scanning Electron Microscope
TEM	Transmission Electron Microscope

Chapter 1

1 Introduction

1.1 Motivation

1.1.1 Human knee joint

Human knee joint is the largest hinge type and most complex synovial joint in the body. It is formed by the tibia (shinbone), femur (thighbone) and patella (knee cap). In addition, two fibrocartilaginous menisci improve congruency between the femur and tibia during joint movements. The knee joint is reinforced by collateral ligaments and two very strong cruciate ligaments that help provide smooth motion to the joint. A salient feature of synovial joint is the existence of lubricating synovial fluid in the synovial cavity around the articulating surfaces [1, 2].

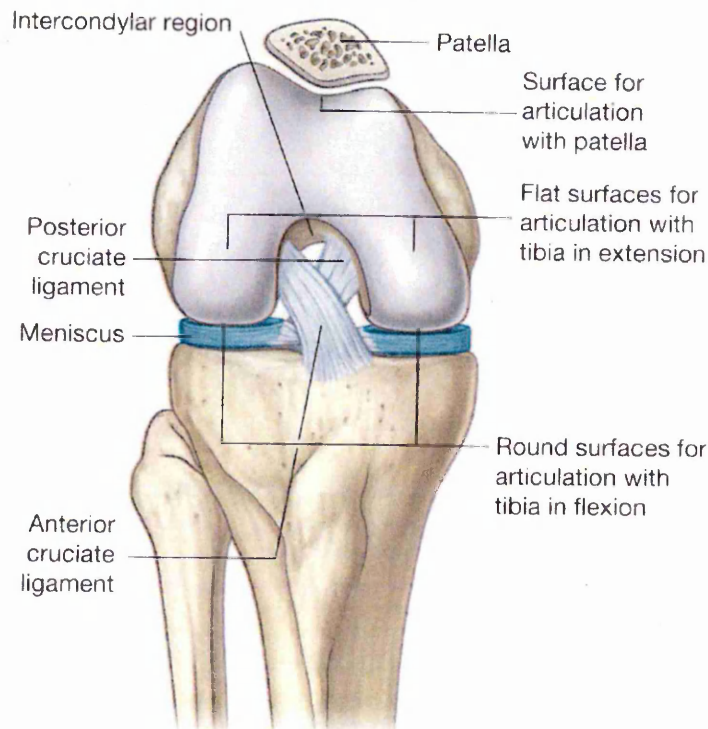

Figure 1.1 Anatomy of human knee joint [2]

1.1.2 Knee replacement joints

A human knee joint affected by degenerative diseases such as osteoarthritis (inflammation, pain and loss in function) loses its inherent mechanical properties due to the excessive loading or lack of natural biological self-curing process. Moreover diseases like osteoporosis (weakening of the bones) and trauma can also affect the normal functioning of the knee [3]. These diseases may lead to knee arthroplasty which is a surgical procedure to replace the diseased weight-bearing surfaces of the knee joint with artificial biocompatible implants to ease pain and restore its normal functions. Two types of knee replacement procedures are being practiced depending on the extent of the joint damage. Partial knee arthroplasty is prescribed when one of the problematic knee components needs to be replaced. On the other hand total knee arthroplasty is performed when two or more components of the knee joints are damaged [4].

An ideal knee implant should be extremely biocompatible with excellent corrosion resistance in vivo, best combination of high strength and low modulus, high fatigue and wear resistance, high ductility and without any cytotoxicity [5, 6]. Main components of a total knee joint Replacement (TKR) prosthesis are femoral head, tibial bearing and tibial plate [7].

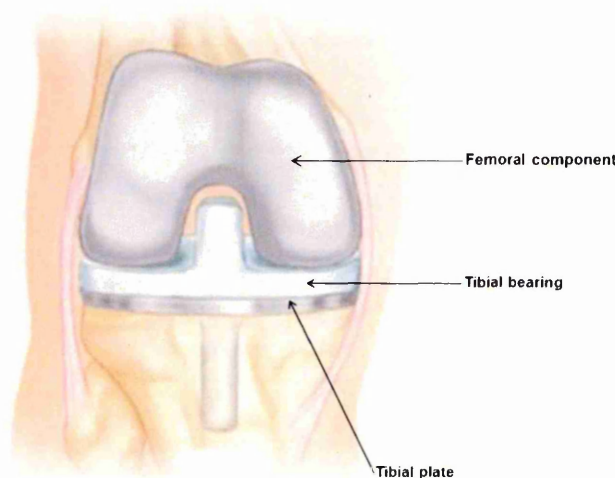

Figure 1.2 Main components of a total knee implant replacement [4]

Normally, femoral component is a metal; either 316L stainless steel (SS) or CoCrMo (cobalt-chromium-molybdenum) alloy or titanium alloy. The tibial bearing is made of Ultra-High Molecular Weight Polyethylene (UHMWPE) and tibial plate is made of CoCrMo alloy or titanium alloy [4]. This type of prosthesis is called as metal-on- polymer total knee replacement implant [Fig. 2]. The metal-on-polymer implant has been widely used in knee arthroplasty.

1.1.3 Limitations of existing metallic biomedical materials

Unfortunately, artificial knee implants may also fail after a certain period of time due to various causes like wear, corrosion, fibrous encapsulation, low fracture toughness, low fatigue strength, mismatch in modulus of elasticity between bone and implant and loosening of the implant [3]. The materials used for the manufacturing of implants and their limitations due to various reasons are listed in Table 1.

Table. 1.1 Reasons for implant failure

Material	Reasons for failure	Complications
316L SS	release of Ni and Cr elements due to corrosion in vivo [8].	toxic [9] and dermatitis [10].
CoCrMo alloys	release of Cr and Co elements due to corrosion in vivo [8].	toxic [9] and carcinogenicity [10].
Ti alloys	release of Al and V ions [11, 12], poor shear strength, excessive wear [13] and high coefficient of friction [14].	Alzhemier, neuropathy & ostemomalacia [11, 12], inflammation, pain, loosening of implants due to osteolysis [14].

The failure of implants leads to revision surgery which is a complex procedure that requires meticulous preoperative planning, specialized implants and tools, and an expert knee surgeon to achieve a good result. However the success rate of revision surgeries is very small. [15] According to S. Kurtz et al., by 2030, the number of total

knee replacement surgeries is projected to grow by 673% to 3.48 million procedures and the number of knee revisions surgeries is expected to increase by 607% [16]. Nowadays, implants available in the market could last up to 20 years after the replacement surgery [17]. However, it is very difficult to determine the life time of an implant due to number of different types of patients and implants available in the market. Moreover, the longevity of the implants seems to be affected by the certain factors such as age (age < 50; may require revision surgery), patient activities (excessive stress on the implants due to inappropriate day today activities), certain complicated medical conditions that affect the knee implants [15]. Therefore implant manufacturers are constantly endeavouring to develop a better implant with increased longevity.

1.2 Surface engineering of implants

The performance enhancement of implants can be achieved by depositing a biocompatible coating with better adhesion, mechanical, tribological and corrosion properties. To develop an ideal coating for a particular application, a suitable material and deposition technique have to be considered since they heavily determine the performance of the coatings. Magnetron sputtering, a variant of physical vapour deposition (PVD) technique has been widely preferred for the deposition of thin film coatings as the coatings prepared by this method outperform the coatings prepared by utilising other physical and chemical deposition techniques. A detailed review on selected thin film deposition techniques to date is presented in Chapter 2.

In 1987, the corrosion resistance of the CoCrMo alloy hip femoral component was enhanced by depositing a TiN (titanium nitride) coating using PVD technique. The release of harmful metal ions from the CoCrMo alloy was also found to be reduced. However the release of titanium ions from the coating was observed [18]. The Ti ions were considered to be less harmful as compared to CoCrMo metal ions as the former is

completely inert to the body environment [19]. J.I. Onate et al. showed that the deposition of diamond like carbon coating (DLC on CoCrMo alloy - knee component) and nitrogen ion implantation (on CoCrMo alloy or UHMWPE) improved the wear behaviour of UHMWPE compared to TiN coating (on CoCrMo alloy) [20]. However PVD coatings are known for growth related structural defects such as micro cracks, pores, pinholes and grain boundaries which deteriorate the performance of the coatings [21]. Hence the highly dense microstructure without any such defects is necessary to achieve better performance. Most of the PVD techniques exploit ion bombardment during the deposition. It has been proved that the high flux ion irradiation improves the density of the coatings. In addition, the process parameters such as bias voltage, substrate temperature and total pressure may also participate in the microstructure evolution.

1.2.1 High Power Impulse Magnetron Sputtering

HIPIMS, relatively a new pulse power technique, is a type of unbalanced magnetron sputtering that produces highly dense plasma containing more metal ions than neutrals in front of the target unlike conventional magnetron sputtering. The high flux ion bombardment increases the ad-atom mobility on the surface of the growing coating which eventually leads to the microstructure densification [22]. This technology was first described by Mozgrin et al. [23] and later developed and patented by Kouznetsov et al [24, 25]. The micro structural studies by A. P. Ehiasarian et al. revealed that the structure densification of TiN can be achieved by high energy ion bombardment during HIPIMS deposition [26]. It has been reported that that the surface pre-treatment using metal ion rich HIPIMS plasma considerably enhanced the adhesion strength of the coating by providing a clean, well defined crystalline coating-substrate interface which promotes localized epitaxial growth on large areas [27]. Thus HIPIMS is found to be a promising thin film deposition technique to deposit high density

coatings on knee implants with superior properties. A detailed discussion on HIPIMS is presented in Chapter 2

1.3 Present research work

1.3.1 Aims & Objectives

- Based on the above mentioned motivations, our aim is to develop PVD coatings with excellent adhesion, mechanical, tribological and corrosion properties to increase the longevity of total knee replacement joints. HIPIMS has been utilised to deposit coatings since it is proven to be a right tool for tailoring the microstructure and properties of a coating. An industrial size four cathode magnetron sputtering system enabled with HIPIMS technology at Sheffield Hallam University is used for this study. Metal nitride coatings have been chosen since it exhibits excellent mechanical, tribological and corrosion properties.
- To begin with, plasma diagnostics will be carried out using optical emission spectroscopy (OES) while sputtering Ti target in Ar + N_2 atmosphere by utilizing various HIPIMS/UBM sources by varying the process parameters such as coil current and N_2 flow.
- Then, single layer TiN coating will be deposited by varying the degree of HIPIMS utilisation and the process parameters such as bias voltage and coil current to thoroughly understand the effect of degree of HIPIMS utilisation on the microstructure, residual stress, texture, mechanical, tribological and corrosion properties of such coatings. The degree of HIPIMS utilisation will be altered by increasing the number of HIPIMS targets used for the deposition. Four different source combinations will be used for this purpose, as follows: 4 cathodes in conventional DCMS (henceforth UBM) mode to deposit pure UBM coating, 1HIPIMS + 3UBM and 2HIPIMS + 2UBM cathodes to deposit

combined HIPIMS/UBM coatings and 2HIPIMS cathodes to deposit pure HIPIMS coatings.

- TiN/NbN, TiCN/NbCN and CrN/NbN multilayer coatings will be deposited on CoCr alloy test buttons along with other (HSS, SS and Si) substrates since our intended application is on total knee replacement joints made of CoCr alloy. The knowledge gained by investigating the TiN (Ar + N_2) plasma and the properties of TiN will be used to determine the process parameters for depositing the multilayer coatings. Various analytical techniques will be used to characterise the coatings.

References

1. DRAKE, Richard L., VOGL, Wayne and MITCHELL, Adam W. M. (2005). Joints. In: *Gray's anatomy for students.* First ed., 38.
2. DRAKE, Richard L., VOGL, Wayne and MITCHELL, Adam W. M. (2005). Knee joint. In: *Gray's anatomy for students.* First ed., 532-533.
3. GEETHA, M., et al. (2009). Ti based biomaterials, the ultimate choice for orthopaedic implants – A review. *Progress in materials science,* **54** (3), 397-425.
4. American academy of orthopaedic surgeons (06, 2010). [online]. at: http://orthoinfo.aaos.org/topic.cfm?topic=A00585.
5. LONG, Marc and RACK, H. J. (1998). Titanium alloys in total joint replacement—a materials science perspective. *Biomaterials,* **19** (18), 1621-1639.
6. WANG, Kathy (1996). The use of titanium for medical applications in the USA. *Materials science and engineering: A,* **213** (1–2), 134-137.
7. *Biomet knee joint replacement prostheses.* (06, 2010). [online]. at: http://www.biosol.co.in/pdf/01-50-0975.pdf.
8. OKAZAKI, Yoshimitsu and GOTOH, Emiko (2005). Comparison of metal release from various metallic biomaterials in vitro. *Biomaterials,* **26** (1), 11-21.
9. WAPNER, K. L. (1991). Implications of metallic corrosion in total knee arthroplasty. *Clinical orthopaedics and related research,* (271), 12-20.
10. MCGREGOR, D. B., et al. (2000). Evaluation of the carcinogenic risks to humans associated with surgical implants and other foreign bodies — a report of an IARC monographs programme meeting. *European journal of cancer,* **36** (3), 307-313.
11. RAO, S., et al. (1996). Effect of Ti, Al, and V ions on the relative growth rate of fibroblasts (L929) and osteoblasts (MC3T3-E1) cells. *Bio-medical materials and engineering,* **6** (2), 79-86.

12. WALKER, P. Roy, LEBLANC, Julie and SIKORSKA, Marianna (1989). *Effects of aluminum and other cations on the structure of brain and liver chromatin.* American Chemical Society. Biochemistry, **28** (9), 3911-3915.
13. MILLER, P. D. and HOLLADAY, J. W. (1958). Friction and wear properties of titanium. *Wear,* **2** (2), 133-140.
14. LIANG JR., P. G., FERGUSON JR., E. S. and HODGE, E. S. (1967). Tissue reaction in rabbit muscle exposed to metallic implants. *J biomed mater res,* **1**, 135-149.
15. CLUETT, Jonathan (April 20, 2013). ***How long do knee replacements last?*** [online]. at: http://orthopedics.about.com/od/kneereplacement/f/How-Long-Do-Knee-Replacements-Last.html.
16. KURTZ, Steven, et al. (2007). Projections of primary and revision hip and knee arthroplasty in the united states from 2005 to 2030. *The journal of bone & joint surgery,* **89** (4), 780-785.
17. BUECHEL, Frederick F. Sr, et al. (2001). Twenty-year evaluation of meniscal bearing and rotating platform knee replacements. *Clinical orthopaedics and related research,* **388,** 41-50.
18. WISBEY, A., GREGSON, P. J. and TUKE, M. (1987). Application of PVD TiN coating to Co-Cr-Mo based surgical implants. *Biomaterials,* **8** (6), 477-480.
19. MEARS, D. C. (1979). *Materials and orthopaedic surgery.* Baltimore, USA, Williams & Wilkins.
20. OÑATE, J. I., et al. (2001). Wear reduction effect on ultra-high-molecular-weight polyethylene by application of hard coatings and ion implantation on cobalt chromium alloy, as measured in a knee wear simulation machine. *Surface and coatings technology,* **142-144,** 1056-1062.

21. JEHN, H. A. (2000). Improvement of the corrosion resistance of PVD hard coating–substrate systems. *Surface and coatings technology,* **125** (1–3), 212-217.

22. PETROV, I., et al. (1989). Microstructure modification of TiN by ion bombardment during reactive sputter deposition. Thin solid films, 169 (2), 299-314.

23. MOZGRIN, D. V., FETISOV, I. K. and KHODACHENKO, G. V. (1995). *Plasma Physics reports,* **21** (5), 400.

24. KOUZNETSOV, Vladimir, et al. (1999). A novel pulsed magnetron sputter technique utilizing very high target power densities. *Surface and coatings technology,* **122** (2–3), 290-293.

25. KOUZNETSOV, V., (2001). *Method and apparatus for magnetically enhanced sputtering.* United States of America Patent 6,296,742 (application number US 09/393,294).

26. EHIASARIAN, A. P., et al. (2011). Influence of high power impulse magnetron sputtering plasma ionization on the microstructure of TiN thin films. *Journal of applied physics,* **109,** 104314.

27. EHIASARIAN, A. P., WEN, J. G. and PETROV, I. (2007). Interface microstructure engineering by high power impulse magnetron sputtering for the enhancement of adhesion. *Journal of applied physics,* **101,** 054301.

Chapter 2

2 Literature Review

This chapter starts with a short introduction of plasma and the classical DC glow discharge process. A brief review of selected PVD techniques such as evaporation, sputtering and cathodic arc deposition is presented to highlight the capabilities and the limitations of such techniques. The advantages of using HIPIMS for the surface pre-treatment and the deposition of coatings are discussed in detail. Dependence of process parameters such as substrate temperature, substrate bias, gas pressure, metal ion to neutral ratio and ion energy on microstructure evolution during coating growth is discussed by illustrating various structure zone models. The final section of this chapter investigates the possibility of employing various thin film coatings such as monolithically grown transition metal nitrides, carbides and its superlattices, hydroxyapatite and DLC as biomaterials for the application of protecting orthopaedic implants.

2.1 Plasma & Glow discharge

Plasma is a quasineutral gas consisting of positive ions and negative electrons with numerous neutral atoms which exhibits collective behaviour. The quasineutral behaviour of plasma is attributed to the approximately equal amount of positive ions and negative electrons present in a given volume element. In the plasma, ion-electron pairs are continuously generated and destroyed by ionization and recombination respectively. The motion of these charged particles gives rise to electric fields and current, and thus magnetic fields. These fields influence the other charged particles far-off in the plasma. Thus the motion of charged particles depends on local conditions as

well as the state of plasma in remote regions as well. Irving Langmuir was the first scientist to name the ionised gas mixture as 'plasma' [1, 2].

Generally, in the laboratory, the plasma can be generated by heating and ionising a small amount of gas by driving an electric current through it or by transmitting RF waves into it. This is called as 'glow discharge' since it glows and the ionised gas contains electrons, various types of ions, neutral atoms and molecules. Several collision processes take place in the glow discharge. The main collision processes ionization, excitation, relaxation and recombination due to the electrons are discussed below since they are the essential phenomena in understanding the basic glow discharge process [1,2]. The collision between argon atoms and electrons is considered to illustrate the ionization and excitation processes.

2.1.1 Ionisation

In the ionization process the primary electron ejects an electron from the atom, producing a positive ion and two electrons. The electrons generated by this collision also participate in producing further ionization.

$$e + Ar \longrightarrow 2e + Ar^{+} \tag{2.1}$$

The minimum energy required to eject the most weakly bound electron from the atom is known as the ionization potential [1].

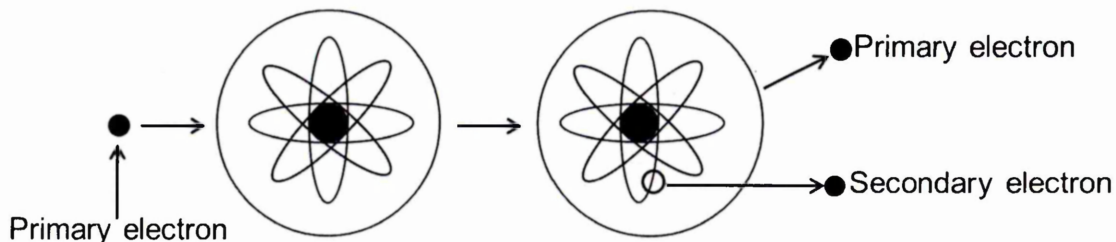

Figure 2.1 Schematic of ionization phenomenon

2.1.2 Excitation

Excitation is a process in which the weakly bound electron is raised to a higher energy level within the atom upon interacting with the primary electron. The excitation potential i.e. the minimum energy required to raise the most weakly bound electron to a higher shell is slightly less than that of the ionization potential since it happens with in the atom [1].

$$e + Ar \longrightarrow e + Ar^{*} \qquad (2.2)$$

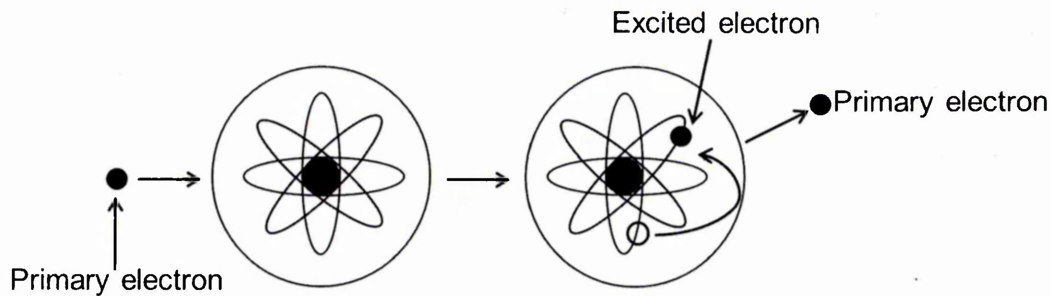

Figure 2.2 Schematic of excitation phenomenon

2.1.3 Relaxation

After the excitation, the excited states of atoms and molecules are usually unstable and the excited electrons tend to return to its original configuration (ground state) in one or many transitions by the emitting photons of very specific energy. The glow in the plasma is attributed to this phenomenon [1].

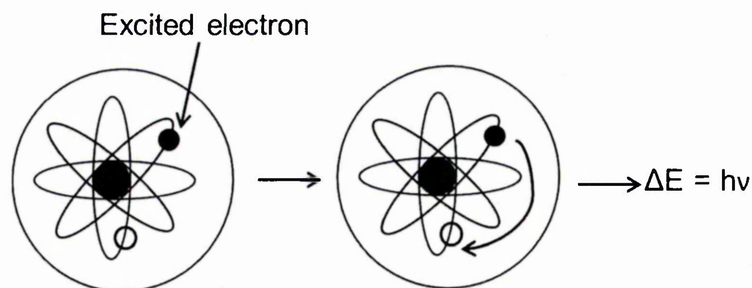

Figure 2.3 Schematic of relaxation phenomenon

2.1.4 Recombination

Recombination is a process where an electron coalesces with a positive ion to form a neutral atom by various recombination processes (3 body recombination, ion-ion recombination and radiative recombination) [1].

2.1.5 Classical DC glow discharge

Fig. 2.4 shows the various zones observed in a classical glow discharge. A glow in front of the cathode is termed as the 'cathode glow' followed by a dark region (sheath) called the 'cathode dark space'. In this region, the electrons and positive ions are accelerated. The adjacent brightest region called the 'negative glow' is due to the excitation and consequent recombination processes discussed above. The region next to the negative glow is known as 'Faraday dark space'. The 'positive column' is between Faraday dark space and 'anode dark space'. It acts as a conducting path between the anode and the negative glow regions [1,3].

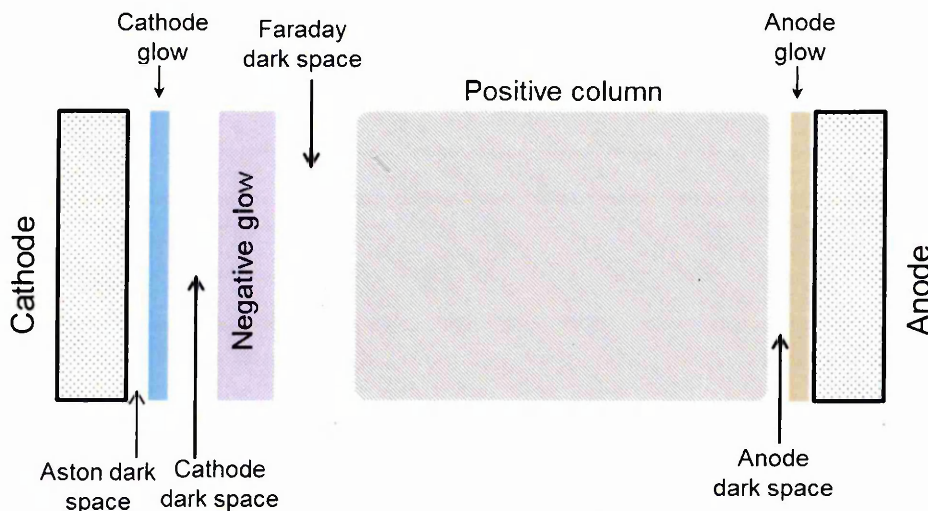

Figure 2.4 Schematic of a glow discharge process

The positive column shrinks when the distance between the electrodes is decreased. This process continues until both the positive column and the Faraday dark space are disappeared. And, the dark spaces adjacent to each electrode and the negative column remain unaffected provided the distance between the electrodes is about two

times the dark space thickness. The discharge is exhausted when the thickness is less than twice the dark space thickness. A glow in front of the anode is called as 'anode glow'. Also, at low pressures a dark space known as 'Aston dark space' is also observed between the cathode and cathode glow [1, 3].

2.2 Thin film deposition techniques

Several thin film deposition techniques are available to deposit various coatings of metals, alloys, ceramics, composites, etc., with different desirable properties from solutions, gases and in a vacuum environment. Generally they are classified as physical and chemical methods. Among these methods, physical vapour deposition has found a wide range of applications.

2.2.1 Physical Vapour Deposition

Schematic of a typical PVD process is shown in Fig. 2.5. PVD is a vacuum assisted process by which a thin film of material is deposited on a substrate in which the material to be deposited is converted into vapour by physical means, then the vapour is transported across a region of low pressure from its source to the substrate; and finally the vapour undergoes condensation on the substrate to form the thin film. These three steps can be easily controlled in PVD processes.

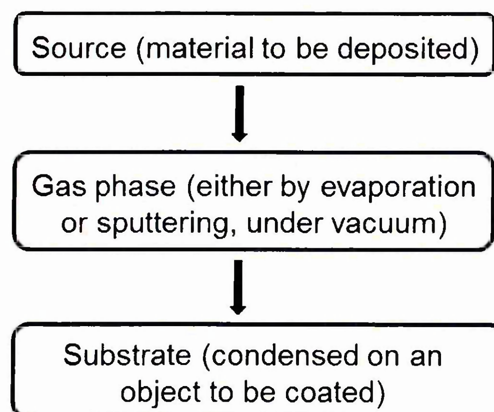

Figure 2.5 Illustration of a typical PVD process

2.2.1.1 Evaporation processes

The metal deposits which Faraday found in 1857 when he exploded metal wires in an inert atmosphere to study the experimental relations of gold (and other metals) to light are thought to be the first evaporated thin films. And this method had no control over the thickness of growing film [3-5]. It is well known that an ideal operating environment for the evaporation of thin films with controlled properties should not be interacting with the process of film formation. In 1887, Nahrlworld discovered the vacuum deposition of thin metals films by Joule heating of platinum wires and a year later Kundit used it to study the optical properties of metal films [3]. However, Holland credited the discovery of vacuum evaporation to Edison citing the latter's deposition of carbon films on the glass envelopes of incandescent carbon lamps. But unfortunately he could not support his claim with proper reference. In 1912, Pohl and Pringsheim succeeded in preparing the thin films of various metals by evaporation from a crucible in a vacuum environment [5].

In a typical thermal evaporation process, the material to be coated, either solid or liquid (evaporant) is kept in a vapour source. The evaporant is heated to increase its vapour pressure by resistance heating or induction heating. Under high vacuum, the vapour molecules escape from the evaporant surface and condense on the substrate. The mechanism of evaporation is mainly governed by the thermodynamics of phase transitions and the kinetic theory of gases. The vapour sources are generally in the form of wires and metal foils. In addition, ceramic crucibles are also used for vapour sources. A variety of vapour sources in different sizes and shapes have been proposed by numerous researchers for various applications [3-5].

In contrast to thermal evaporation, the source material is evaporated by a stream of electrons accelerated through electric fields of generally 5 to 10 kV and focussed onto the evaporant surface in the electron beam (e-beam) evaporation process. The

kinetic particle energy of the impinging electron is then converted into heat energy typically more than 3000 °C. The electron guns used in the e-beam evaporation fall into the following categories: work-accelerated, self-accelerated and Bent-beam electron guns. The e-beam only heats the evaporant and not the entire crucible unlike thermal evaporation since electrons are being charged particles and it can be controlled by applying electric or magnetic field. Thus, the interactions between evaporant and support materials are considerably reduced that leads to lower degree of contamination from the crucible [3].

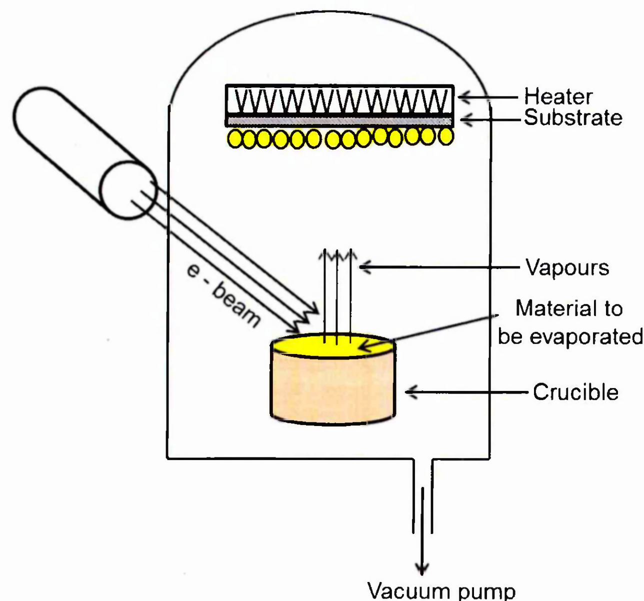

Figure 2.6 Schematic of e-beam evaporation process

While evaporating a compound, each of its constituent will have different vapour pressures. Hence apparently the deposition rate also will be different. This leads to a film with different stoichiometry compared to the original source material. The difficulty in achieving a stoichiometric film has also been addressed with "co-evaporation" technique using two e-beam guns. Moreover, it suffers from poor step coverage, inhomogeneous film thickness. In addition to this the deposited film is prone to damages due to X-rays in the case of e-beam evaporation. This technique is not widely been used in the industries as compared to the sputtering.

2.2.1.2 Sputtering

In 1852, Grove observed a metallic deposit in the region of the negative electrode while investigating electrical discharges in a glow discharge tube [6]. The same phenomenon was also reported by Plucker in 1858 [3]. These observations prompted to use the electrical discharges for thin film deposition purposes. Since then the technology has been developing rapidly to meet the various demands in the field of thin films. In the typical sputtering process, a target (cathode) is bombarded by energetic ions in glow discharge plasma created in front of the target in vacuo. Secondary electrons emitted from the target surface play an important role in sustaining the plasma. The sputtering yield (Y) determines the productivity of the process and it is defined as the number of atoms sputtered from the surface of a target per incident ion.

Sputtering yield (Y) = number of atoms sputtered/incident ion

The sputtering yield depends on a lot of parameters like target properties, energy on target material and angle of incidence, etc. Simple sputtering technique had few limitations like low deposition rates, low ionisation efficiencies in the plasma and high substrate heating effect. These drawbacks motivated the scientists to search for other alternatives.

2.2.1.3 Magnetron sputtering

The basic principle of all magnet based sputtering techniques was first discovered by Frans Penning and it led to the development of conical magnetron (sputter gun) and cylindrical magnetron sources [7, 8]. Since mid-1970s, the planar magnetron sputtering [DC and RF (radio frequency)] has been widely used for thin film deposition. Fig. 2.7 depicts the basic mechanisms involved in the planar magnetron sputtering.

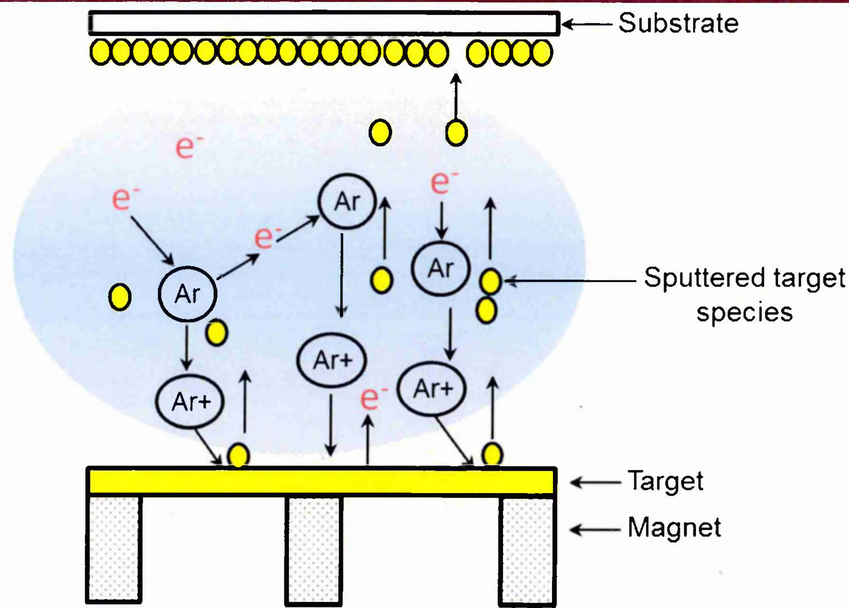

Figure 2.7 Schematic of planar magnetron sputtering process

In a simple magnetron (Fig. 2.8), the cathode surface is subjected to a specially shaped magnetic field by a group of magnets to trap the secondary electrons in a localised region close to the target. This secondary electron trapping leads to dense plasma in the target region which eventually improves the sputtering rate due to increased ion bombardment of the target. Generally, the cathode potential in planar magnetron sputtering is in the range of 300 - 700 V at argon (sputtering gas) pressure of 1.3 Pa which is much lower compared to simple sputtering [8,10].

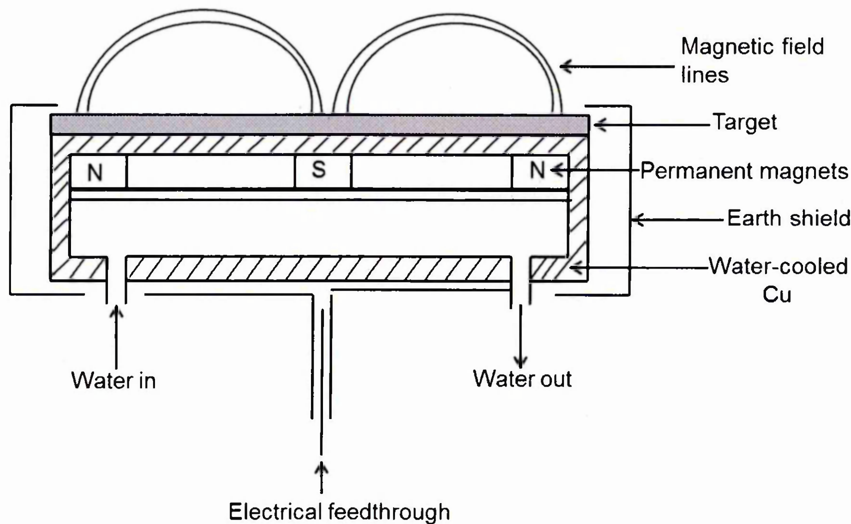

Figure 2.8 Schematic of a simple magnetron sputtering source [9]

In 1977, McLeod et al. successfully demonstrated that planar magnetron sputtering is superior to e-beam evaporation by sputtering aluminium and aluminium-silicon films using planar magnetron sputtering [11]. However, this technique is limited to smaller target-substrate distance since the plasma is confined in the vicinity of the target. In 1986, Window and Savvides introduced the concept of unbalanced magnetron sputtering which involves strengthening either the outer ring of magnets or inner pole with respect to each other. This configuration pushed the plasma further towards the substrate which is confined to the target in the case of balanced magnetron sputtering [12-14]. Munz et al have reported that the substrate bias current density should be 2mAcm^{-2} or more for the reactive deposition of TiN [13] and it is possible with the above said configuration. The difference in the plasma confinements observed for balanced and unbalanced magnetic configurations is shown in Fig. 2.9.

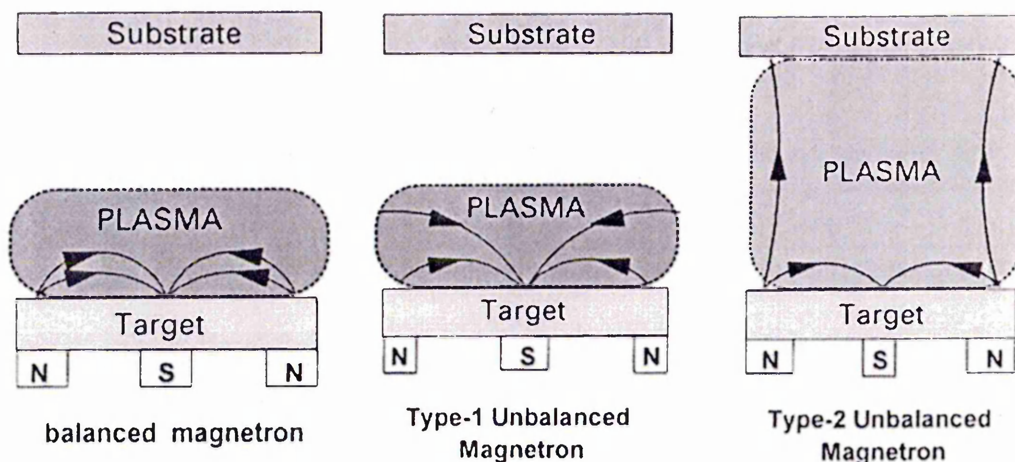

Figure 2.9 Schematic representation of the plasma confinement observed in different magnetron sputtering sources adapted from Ref. [10]

Multiple cathode sputtering systems are quite useful in eliminating the shadowing effect while depositing on complex components [16, 17]. In 1990, Sproul and co-workers deposited TiN coatings in a multiple cathode opposed magnetron sputtering system using two different magnetic configurations such as mirrored and closed filed. In the mirrored setup, magnets are arranged in such a way that the like

poles face each other and opposite poles face each other in the closed filed (Fig. 2.10).

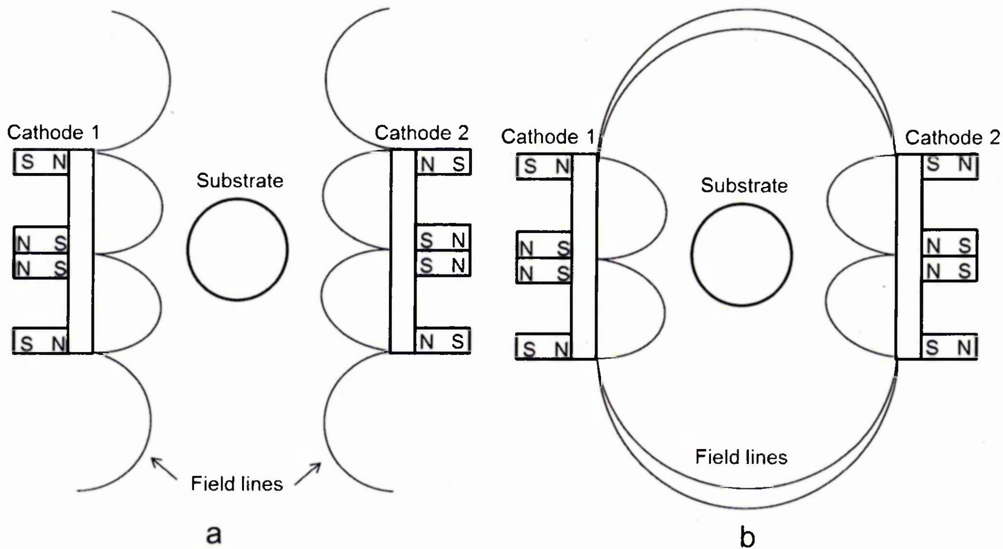

Figure 2.10 Schematic representation of a) mirrored and b) closed field unbalanced magnetic configurations [15]

They have also reported that, for mirrored configuration, the substrate bias current was very low since the plasma density is low at the substrate. A very high substrate current was observed in the case of closed field setup. The sputtering pressure also affects the substrate bias current. At high pressures, secondary electrons loose considerable amount of energy due to the intense collisions near the targets before arriving at the substrate. Hence the degree of ionization is very low which contributes to lower substrate bias current. When the pressure is reduced, the vice-versa occurs and more substrate bias current is generated. However, if the pressure is further dropped, a decrease in substrate bias current is observed due to the fewer gas atoms available for the collision despite having the secondary electrons with significant energy for ionization. TiN coating deposited in the mirrored configuration exhibited poor adhesion with voids due to low ion fluxes whereas the adhesion and hardness was relatively high in the case of coatings made in closed field configuration since high flux ion bombardment plays a vital role in both the nucleation and the growth of the coating [15,18]. In the early 1990s, Teer coatings developed and patented a sputtering system

with multiple magnetrons in closed field configuration [19]. Moreover ionisation efficiency in the plasma is improved by replacing first generation ferrite magnets with stronger rare earth magnets. Rare earth magnets are capable of generating field strengths in excess of 1kG at the target surface whereas ferrite magnets could generate weak magnetic field in the range between 300-500 G. Therefore, more ion current is seen at the substrate with rare earth magnets [10, 20].

2.2.1.4 Pulsed Magnetron sputtering

The plasma density at the substrate for the deposition of good quality coatings can be increased by increasing the target power density, besides exploiting the different unbalanced magnetic configurations. Though the applied power is limited by the thermal load on the targets, increasing the input power to the target is possible, provided it is distributed over a larger target area. The pulsed magnetron sputtering technique (over 20 kHz) can be used for this purpose [21]. AC (alternating current) or DC power supply coupled with a pulsing unit is used for this purpose. However, the pulsed DC sputtering is widely used. In 1991, Gruen have reported in his patent that the pulsed DC sputtering can be utilized to generate the target power densities of less than 50 Wcm^{-2} and the current density of 0.5 $mAcm^{-2}$ at substrate by pulsed DC sputtering [22]. It has been reported that the high bias current densities of up to 10 mA cm^{-2} was observed with TiN unipolar pulsed sputtering [21].

Pulsed DC sputtering can be exploited to overcome the problems due to the 'target poisoning' effect too. The 'target poisoning' is defined as the formation of a thin layer of reacted 'compound film' on the target surface during dc reactive magnetron sputtering. The different sputtering yield of the target material and compound film affect the sputtering rate and stoichiometry of the deposited film which eventually leads to the poor performance of the coatings. Moreover, if the film is an insulator like alumina, it is charged up by the positive ions impinging the target before breaking down

in the form of an 'arc'. Due to this high current density arc discharges; droplets are ejected from the target which can also cause defects in the growing film. And, the damaged area may be prone to more arcs. Frequent arc discharges also lead to fluctuations in the process parameters which results in interrupted sputtering [10, 21, 23]. The difficulties in sputtering of insulators were first reported by Wehner in 1955 [24].

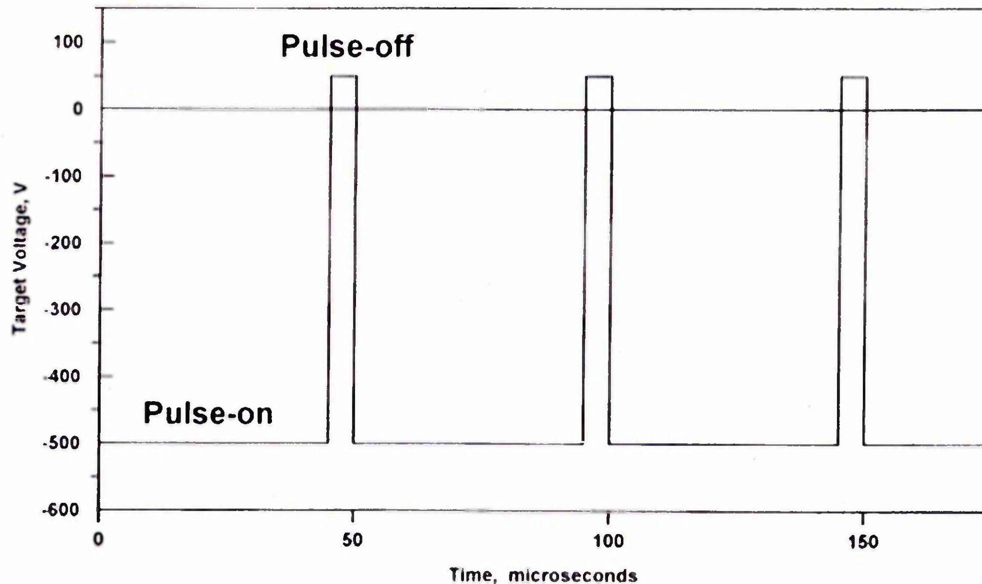

Figure 2.11 Schematic representation of the target voltage waveform for a pulsed DC power supply operating in asymmetric bipolar pulse mode [10]

There are two types of pulsed DC sputtering: unipolar where only a single magnetron is connected to a pulse power supply and bipolar where two magnetrons are connected to the same power supply. In the unipolar sputtering, the voltage applied to a single target is pulsed between the typical operating voltage (- 400 to 500 V) and ground. The target material is sputtered off from the target during the pulse-on time and then the discharging takes place during the pulse-off time. In the bipolar sputtering, the polarity of the voltage applied to the target during 'pulse-on' time is reversed during the 'pulse-off' time so that the target may act once as cathode and once as anode during each cycle. However, usually, the reversed voltage applied to the target during the pulse - off time is between 10 and 20% of the negative operative voltage since it is enough to

neutralise the accumulated positive charge due highly mobile electrons in the plasma than ions. This is called as 'asymmetric bipolar pulsed DC since the voltage applied to the target is not fully reversed. In this case, the target material is sputtered off from the target during the pulse-on time and, subsequently the positively charged target layer is neutralized during the pulse-off time since the voltage becomes positive [10, 21, 23].

The RF sputtering can also be utilized to deposit the insulating films with superior qualities. The plasma is ignited using RF generator (typically operating at 13.56 MHz) along with a matching network to maximise the power transmission from the generator to the electrode. An alternating voltage is applied to the target. During the negative half cycle, the target material is sputtered off from the target and, subsequently the accumulated positive charge is neutralized during the positive half cycle. However, the deposition rates are usually low since the sputtering takes place during only the negative half cycle [10, 23]. RF deposition of insulating oxide films can be found elsewhere in the literature [8, 25, 26].

2.2.1.5 High Power Impulse Magnetron Sputtering (HIPIMS)

HIPIMS is also a pulse power technology that utilizes much higher peak target power density which results in a much higher ion current density at the substrate compared to other magnetron sputtering techniques [13, 22]. The power density applied on the target is increased by decreasing the duty cycle of the pulses. A typical HIPIMS power supply used by Kouznetsov et al. in 1999 for the deposition of copper (Cu) comprises a conventional DC power supply coupled with a pulsing unit as shown in Fig. 2.12. The pulsing unit is a combination of a charging circuit and a trigger circuit. The capacitor is charged and discharged via a thyristor switch by charging and trigger circuit respectively [28].

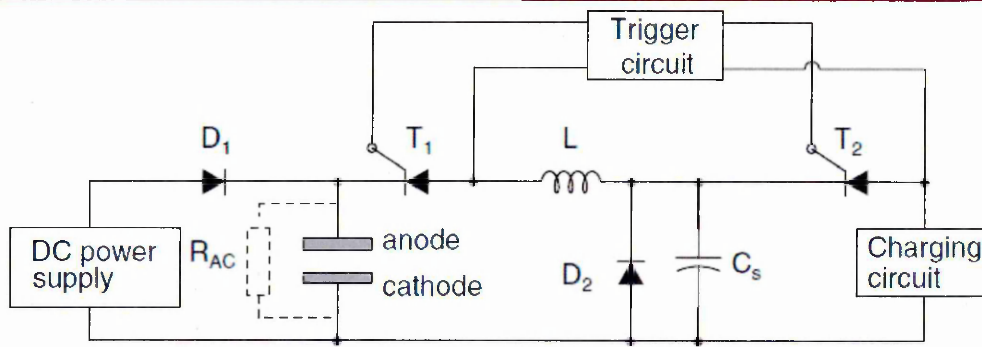

Figure 2.12 An electric circuit diagram representing a HIPIMS pulse generator with a pre-ionizer [28]

Kouznetsov et al. have utilised a peak power density of 2.8 $kWcm^{-2}$ and observed a peak ion current density of 3.4 Acm^{-2} at the substrate during the deposition of Cu. The typical voltage and current behaviour observed during this discharge is shown in Fig. 2.13. The average power was kept to be less than 800 W to avoid overheating the target. The plasma analysis using Langmuir probe showed that the ionized flux arriving at the substrate comprised 70% of ionized copper. Moreover, a dense coating without any voids was observed within the via-holes containing negatively biased silicon substrates. This indicated the strong directionality of the deposited ion flux which could be useful for various applications. Also, increased target utilization was observed with considerably broader race track [27]. It is well known that arc free operation is essential for a stable process and the deposition of high quality coatings. A number of arc controlling devices have been built for dealing with the arcs generated during conventional sputtering such as DC [29, 30]. In 2004, Christie et al. demonstrated the successful operation of their power supply with arc handling for high peak power magnetron sputtering [31].

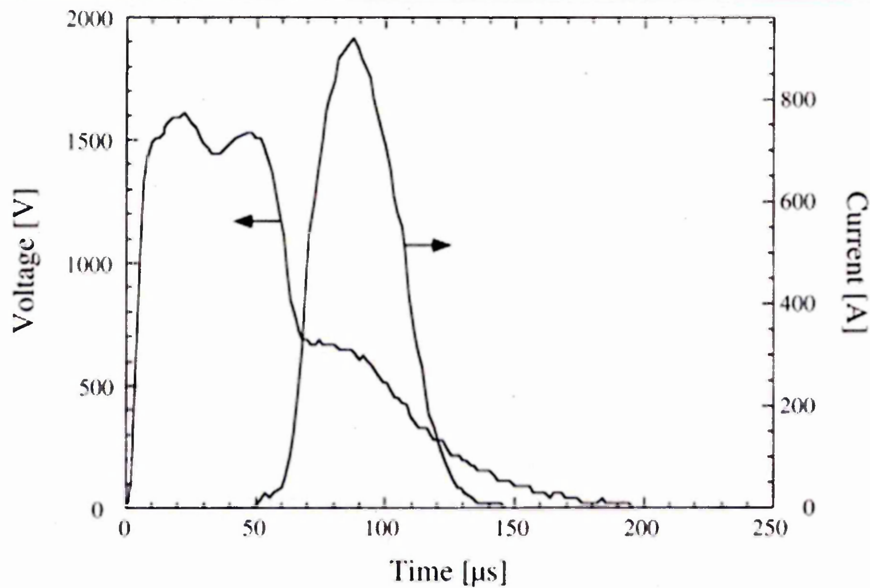

Figure 2.13 A typical voltage and time trace for the HIPIMS discharge [27]

Ehiasarian et al. observed up to two-fold ionised metal ions of Cr and Ti (Cr^{1+},Cr^{2+} and Ti^{1+}) while investigating the plasma composition using optical emission spectroscopy (OES) during high power pulse sputtering of Cr and Ti. The Ti ion to neutral spectral line ratio found to be increased a factor of 5 compared to RF coil enhanced sputtering. The peak power applied to the target was 3 $kWcm^{-2}$. The peak ion current density also considerably increased with increasing peak target current. The peak plasma density was of the order of 10^{13} Cm^{-3}. The degree of ionisation of the sputtered Cr flux was 30% [32]. In 2004, Ehiasarian and Bugyi utilised a power supply capable of delivering peak currents of up to 3000 A and at a voltage of 2000 V for the sputtering of Ti in an industrial size sputtering machine. The power supply enabled with the arc suppression design minimized the arc energy and facilitated arc free sputtering for several hours [33].

The time evolution of the HIPIMS plasma was first reported by Macak et al. in 2000 [34] and later studied in detail by Ehiasarian et al. [32]. The comparison between the discharge current trace and the optical emission spectra observed during the sputtering of Ti in Ar atmosphere showed that the plasma was Ar dominated in the beginning of the pulse and subsequently the metal ions were generated after a certain

period of time [34]. This can be explained by the gas rarefaction effects discussed by Rossnagel and Kaufman where the working gas density in front of the target was found to be decreased due to the transfer of the kinetic energy of the sputtered atoms to the gas when the discharge current to the target was increased [35].

Usually the deposition rate by HIPIMS process is found to be lower compared to a conventional DC magnetron sputtering at the same average power. Several studies have reported on the lower deposition rate. The most important reason for the lower deposition rate is that some of the newly generated metal ions in the sputtered material close to the target are attracted back to the target surface by the cathode potential. The metal ions that return to the target causes sputtering called 'self-sputtering' (sputtering of target material by target material ions) [28, 36, 37]. Christie et al. have demonstrated by their model that it is possible to achieve increased deposition rates in HIPMS discharge compared to conventional DC magnetron sputtering provided the self-sputtering yield exceeds the process gas ion sputtering yield by unity or more [36]. The various other factors affecting the deposition rates in HIPIMS process can be found elsewhere [28, 37].

2.2.1.5.1 Surface pre-treatment using HIPIMS discharge

A surface pre-treatment is performed to remove the contaminants prior to coating deposition during the PVD processes. The substrate is sputter cleaned by bombardment of Ar ions generated in Ar glow discharge plasma. The Ar ions are accelerated to several hundred eV by applying a huge negative bias voltage on the substrates. However, sputter cleaning by gas ions has few disadvantages such as the difficulty in removing carbon-based contaminants and the incorporation of the gas ions into the substrate. The incorporated gas ions induce increased strains in the substrate lattice and create porosity that leads to weakening of the interface when heated during the pre-treatment. It is essential to generate enough Ar ion density for the efficient

substrate cleaning. The plasma density enhancement can be achieved by increasing the pressure and/or by using RF or mid-frequency bipolar pulsing discharge. However, the complex nature of RF discharge systems may lead to reproducibility issues. Cathodic vacuum arc etching can also be used for the surface pre-treatment since it is possible to generate high plasma densities of 10^{10} cm^{-3} and ion current densities of up to 10 mA cm^{-2} at the substrate by this technique. The plasma generated in such discharge is found to have highly ionized metal flux and even the discharge may be operated without any process gas. The metal ions accelerated by suitable substrate bias can be used for the substrate cleaning since the high energy ion bombardment may lead to significant resputtering whereas the low energy ion irradiation cause metal deposition instead of sputter cleaning [38]. Schönjahn et al. have reported that the Cr ion irradiation on steel substrate using steered cathodic arc discharge resulted in a Cr implanted interface zone which promotes localized epitaxial growth of the coating over individual grains of the substrate [39]. However, cathodic arc discharges are characterized to produce droplets which are undesirable for many applications. The mechanism behind the formation of the droplets, their role on the microstructure evolution during thin film deposition and subsequent effect on certain properties is discussed in detail in other sections.

HIPIMS can also be used for the substrate pre-treatment as it also produces highly ionized metal flux comparable to an arc discharge. In addition, the HIPIMS discharge is free of the macro particles. Typically, a high substrate bias voltage of greater than 1000 V is used for HIPIMS etching. Ehiasarian et al. have observed the Cr ion implantation in the stain less steel substrates (substrate bias - 1200 V) when subjected to Cr ion irradiation by HIPIMS discharge. Moreover the CrN coating deposited after the Cr ion pre-treatment exhibited superior adhesion with enhanced mechanical properties. The cross section TEM studies revealed that the coating was

columnar, dense and free of droplets [40]. Further studies on the adhesion strength of CrN coatings showed that the coatings deposited after HIPIMS pre-treatment exhibited superior adhesion in comparison to pre-treatments in Ar glow discharge and cathodic vacuum arc processes. Also, the interface was found to be free of amorphous native oxides; hence a well-defined crystal structure at the coating - substrate interface which promotes the localized epitaxial growth of the coating [38].

2.3 Cathodic arc deposition

Cathodic arc deposition technique is one of the oldest deposition techniques and dates back to the 18th century. Edsion was first to patent the practical applications of cathodic arc coatings [41]. Cathodic vacuum arc can be defined as a high current, low voltage electrical discharge between two electrodes by means of highly ionized plasma of vaporized electrode material generated by the arc itself in a vacuum environment. The plasma is generated locally at one or several tiny mobile locations called 'cathode spots' on the cathode in which most of the basic processes of the arc take place [42, 43]. Cathode spots are originated at micro-protrusions on the surface of the cathode. Arc discharges are characterised with low voltages in the range between 20 and 60 V. Also, the discharge voltage is influenced by the cathode material and the magnetic field strength. The applied potential can be multiplied by up to 5 orders of magnitude due to the whisker-like geometry of the micro-protrusions. In addition, the electric field can attain values of 10^5 Vm^{-1} [44]. This electric field in combination with sufficient current density yielded at micro-protrusions is enough to cause Joule heating in the emission regions which eventually prompts the rapid 'explosion' of the cathode material, ionisation and electrical breakdown. The plasma and current density in the vicinity of the cathode spots is typically about 10^{26} m^{-3} and 10^{12} Acm^{-2} respectively [43, 45]. The highly ionised plasma contains considerable amount of multiply charged ions of the cathode material [42]. The ionized flux travels away from the cathode at supersonic

velocities of about 10^4 ms^{-1} due to the highly energetic metal ions typically with kinetic energies of 50 -150 eV and the very high pressure gradient near the cathode [41, 43].

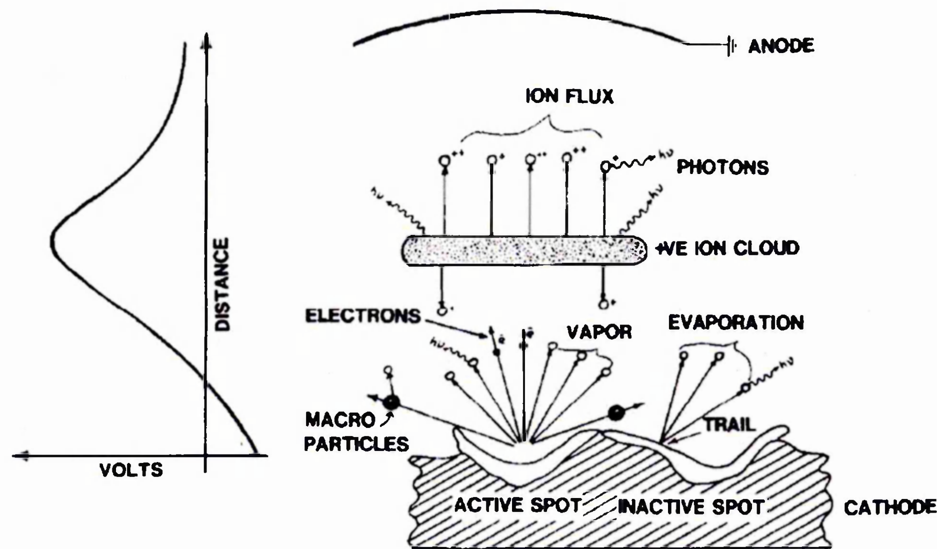

Figure 2.14 Basic arc evaporation processes and potential distribution adapted from Martin et al. [46]

Fig. 2.14 shows schematic of typical arc evaporation processes including the potential distribution between the electrodes. The vaporized flux comprises substantial amount of droplets or macro particles (typically few nm - micron size) of the cathode material. The droplets are ejected during the explosive emission of micro-protrusions in the cathode spot from the molten material which is not sufficiently heated to sublimate. It has been reported that materials have low melting point produce more and larger macro particles and they are likely to move along straight line trajectories [28, 41]. The macro particles are then embedded in the growing coating during the thin film deposition in cathodic vacuum arc discharge. These embedded droplets then create porosity by shadowing the deposition flux and nucleating large scale growth defects throughout the thickness of the coating [47]. These defects contribute in deteriorating the performance of the coatings. Wang et al. proved that the droplets accelerated the substrate corrosion by corroding concurrently with the localised galvanic corrosion of the substrate [48].

The emission of the macro particles can be minimized by introduction of magnetic fields in the region near to the cathode. Furthermore, a drastic reduction of droplets in the coating is possible by guiding the plasma with magnetic filters. The plasma is steered away from the cathode to the substrate which is not in line of sight, by the combination of magnetic and electric fields generated by the magnetic filters [41]. A magnetic filter made of permanent magnet proposed by Ramalingam et al. can be seen in Ref. [49]. Various designs of filter have been proposed several researchers [50]. However, it has been reported that the up-scalability of many filters is not easy due to geometry of such filters [28].

2.4 Microstructure evolution during coating growth

Polycrystalline thin films prepared by various techniques demonstrate a vast variety of microstructures characterized in terms of grain size and crystallographic orientation, lattice defects, phase composition and surface morphology. It is well known that the growth of thin films deposited by PVD techniques includes the following consecutive specific structure evolution stages: nucleation, formation of island, coalescence of islands, growth of polycrystalline islands and channels, development of continuous structure and thickness growth [51]. These processes are illustrated in Fig. 2.15. The three basic mechanisms occurring during the above said film forming processes are as follows [53]:

- The incident atoms become loosely bonded adatoms by transferring the kinetic energy to the lattice
- Then the adatoms are desorbed, by evaporation or sputtering or more commonly become trapped at low-energy lattice sites after exchanging energy with the lattice and other absorbed species while diffusing over the surface.
- Finally, the bulk diffusion process by which the incorporated adatoms relocate their positions within the lattice.

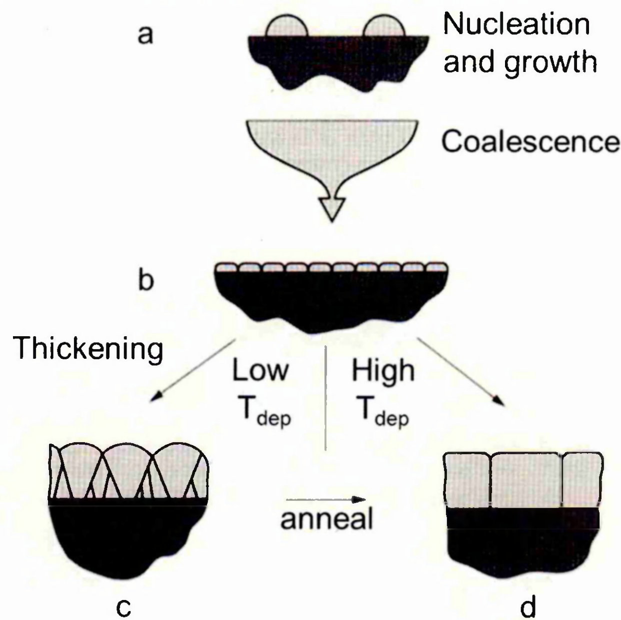

Figure 2.15 Schematic of grain structure evolution during deposition of polycrystalline thin films [52]

The film forming processes such as surface diffusion, bulk diffusion and the sublimation energy can be quantified in terms of the activation energies of surface and bulk diffusion, and the sublimation energy. It has been reported that these energies are proportional to the melting point for many pure metals. Hence several of the basic processes that are responsible for the differences in the resultant coating structures can be expected to dominate over different ranges of T (substrate temperature)/T_m (melting point) [53].

Understanding the correlation between the microstructure evolution and process parameters is essential since the former strongly determines the properties that translate into the performance of a material. Various structure zone models based on the experimental results have been proposed to classify the surface morphology of films prepared by various techniques. The Movchan - Demchishin basic structure zone model (Fig. 2.16) was based on the substrate temperature gradient maintained during the deposition of Ti, Ni, W, ZrO_2, Al_2O_3 and Fe using electron beam evaporation. This model proposed three zones: zone 1 ($T/T_m < 0.3$), zone 2 ($0.3 < T/T_m < 0.5$) and zone 3

($0.5<T/T_m < 1$). The zone 1 consisted of tapered crystals with dome tops (rough) separated by voided column boundaries. The diameter of the crystals found to be increased with T/T_m [53] which indicates very low activation energy and implies very little surface diffusion. The zone 2 contained smooth columnar grains separated by well defined, dense, intercrystalline boundaries. In this case, the width of the grains increased with T/T_m and this could be attributed to the activation energy yielded that was approximately equal to that for surface diffusion. The zone 3 was characterized with equiaxed grains with a bright surface which could be due to an activation energy corresponding to the bulk diffusion [53].

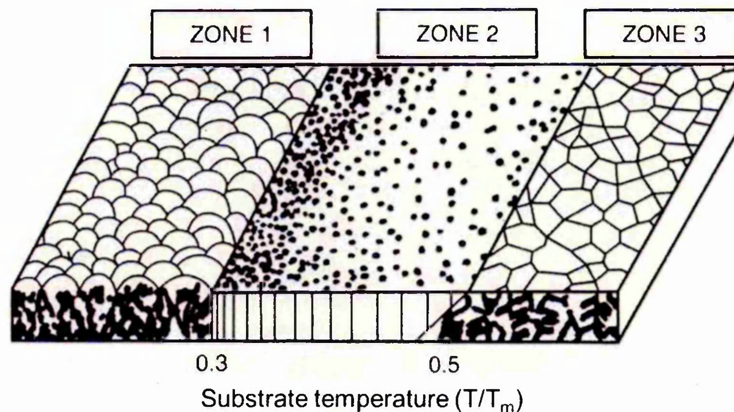

Figure 2.16 Movchan - Demchishin structure zone model [53]

2.4.1 Effect of sputtering parameters on microstructure evolution

In sputtering deposition, the process parameters such as substrate temperature, sputtering gas pressure, substrate bias, etc. affect the microstructure. Thornton extended the basic structure zone model to sputtering by considering the effect of the sputtering gas. The proposed model was based on the experimental results of Ti, Cr, Fe, Cu, Mo and Al alloy coatings deposited on metal and glass substrates using cylindrical-post and hollow-cathode magnetron sputtering systems. The structure zone model for sputtered coatings proposed by Thornton and a schematic representation of physical processes that establishes structural zones is shown in Fig. 2.17 and Fig. 2.18 [53].

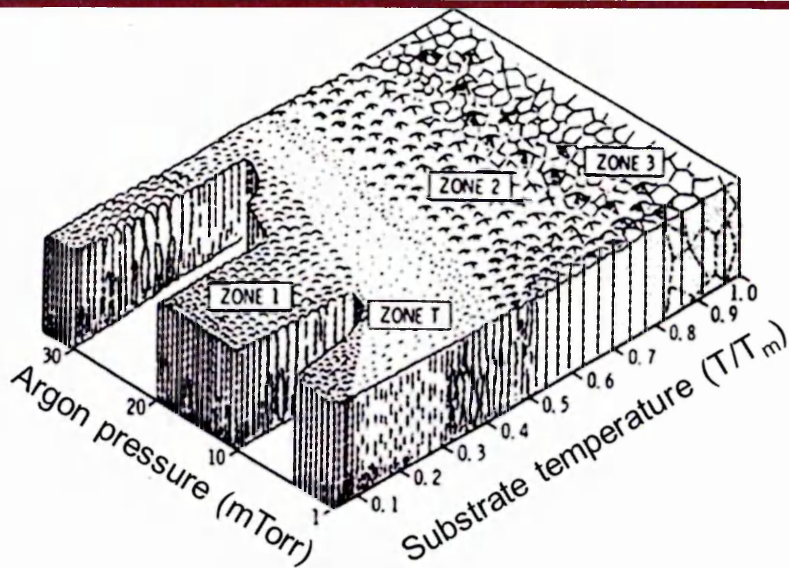

Figure 2.17 Thornton structure zone model [53]

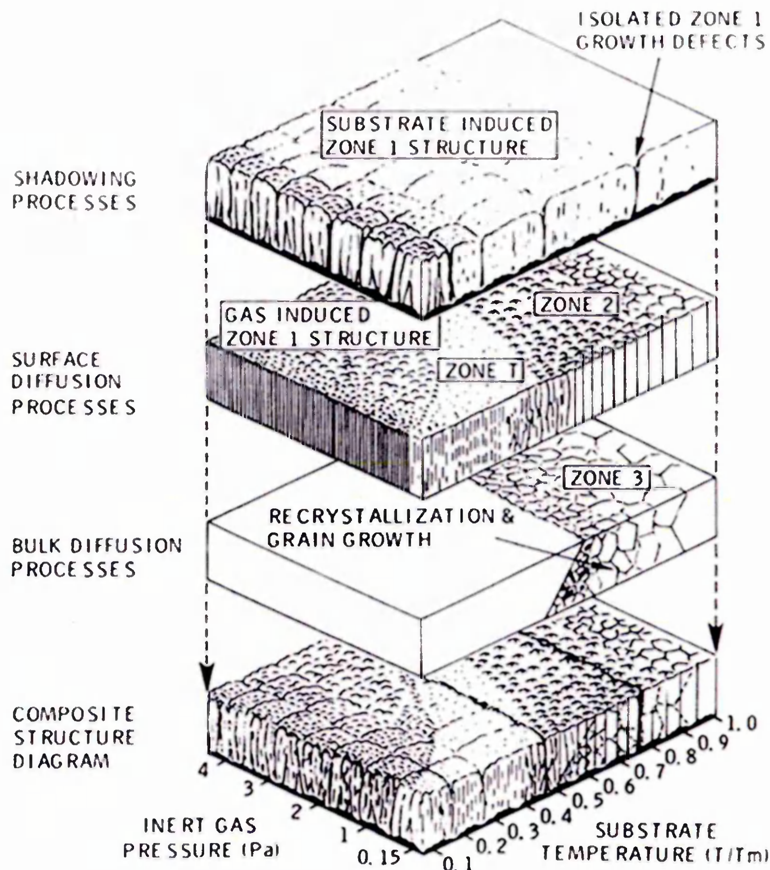

Figure 2.18 Schematic showing the superposition of physical processes that establishes structural zones [53]

The formation of pronounced (dome shaped rough tops) crystal structure with open column boundaries in zone 1 is promoted by the substrate roughness, high argon pressure and an oblique component to the deposition flux. The zone 1 structure is due

to low adatom mobility which is insufficient to diffuse through the open boundaries formed by the atomic shadowing effect. The zone T (internal structure of zone 1) is characterized by poorly defined fibrous crystals separated by dense boundaries at zero T/T_m on infinitely smooth substrates.The zone T terminates at $T/T_m \sim 0.3$ for single phase materials on smooth substrates. Interestingly, the fibrous zone T structure transformed to rough zone 1 structure at high inert gas pressure and low T/T_m even on smooth substrates due to low adatom mobility. However, the influence of inert gas on coating growth at sufficiently elevated temperatures is found to be negligible. The zone 1 structure may be promoted by residual gas adsorption also. The structure in zone 2 is characterized by near-equiaxed shape columnar crystallites with dense intercrystalline boundaries due to adatom surface diffusion. The equaxied or broad columnar shape grains are formed in zone 3 by bulk diffusion processes such as recrystallization and grain growth [53].

According to Thornton's model, zone T evolved with decreasing sputtering gas pressure. Messier et al. demonstrated that the substrate floating potential increased while decreasing the pressure of the sputtering gas.. In addition, the average energy of the sputtered flux that arrives at the growing film surface also increases with decreasing gas pressure. Moreover, it has been reported that the zone 1-T boundary is non-linear and depends on the bias potential as a function of gas pressure. Therefore, Messier proposed a revised structure zone model (Fig. 2.19) by considering the bombardment induced mobility due to the substrate floating potential which was appeared to be the more fundamental process affecting the microstructure along with thermal effects. According to this model, the zone T is small and probably doesn't even exist at zero bombardment. The width of zone 1 is decreased with increasing bombardment energy and a broad zone T was is observed due to high adatom mobility [54].

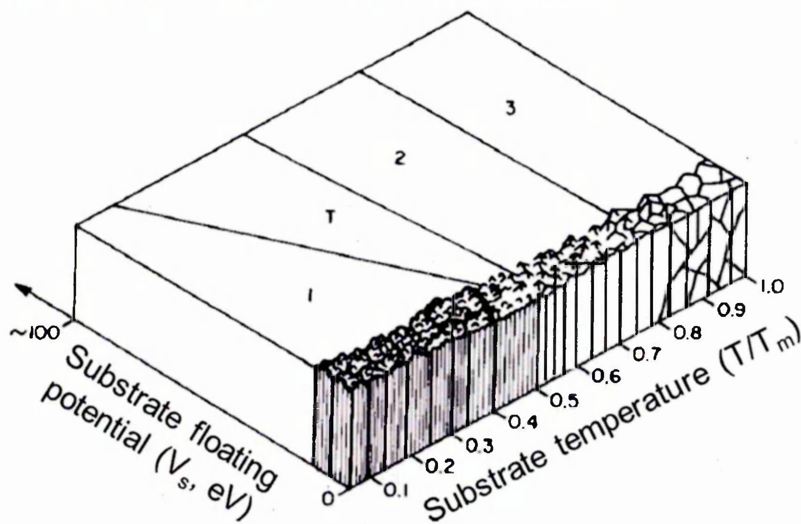

Figure 2.19 Messier structure zone model [54]

It was shown that the microstructure densification of Ta and Cr coatings can be achieved by ion bombardment facilitated by high bias voltage (V_s) during the deposition. The pronounced columnar structure of the coatings grown at zero substrate bias became less columnar while increasing the bias to -500 V. This structure densification was attributed to resputtering of the deposit surface during deposition [55]. It has been reported that the ions to titanium atoms ratio that arrives at the substrate increased from 0.3 to 0.4 when the bias voltage was increased from 40 to 400 V during reactive sputter deposition of TiN. A detailed cross-section TEM analysis showed that the coatings subjected to ion irradiation even at low temperatures found to be with reduced porosity due to enhancement in adatom mobility (recoil implantation and forward sputtering). The microstructure of the coatings deposited at 300° C with $200 \geq V_s \geq 120$ V was fully dense but columnar. The termination of columnar structure, resulting in grain renucleation was observed for coatings grown with $V_s \geq 200$ [18].

Müller has developed a molecular dynamics based model to demonstrate that the structure densification can be achieved by increasing the ion energy (E) and the metal ion to vapour flux ratio (j_I/j_V) which eventually increases the adatom mobility [56]. Various microstructures obtained for different ion to vapour flux ratios and ion energies

are shown in Fig. 2.20 (A-B). Experimental evidences for Müller's modelling results can be seen elsewhere in literature.

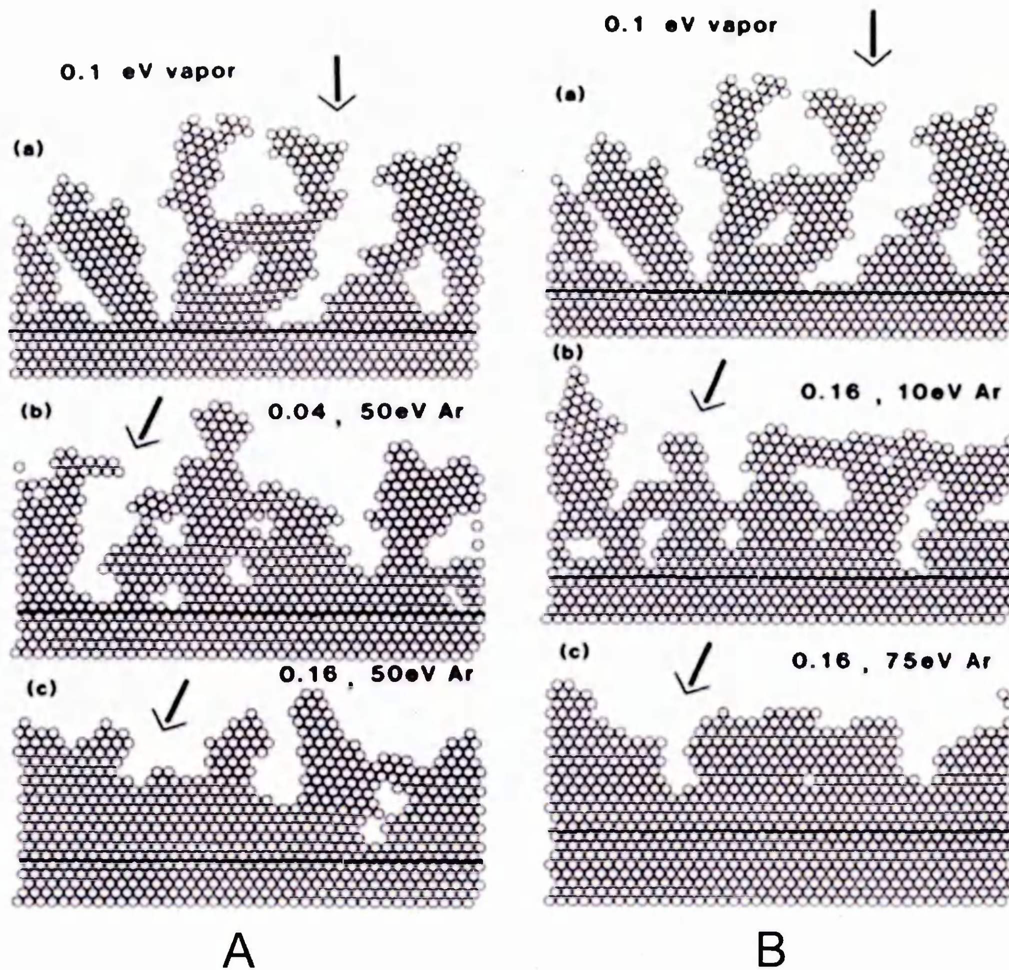

Figure 2.20 Typical microstructures: (A) Microstructure obtained for condensing vapour atoms with kinetic energy of 0.1 eV arriving under normal incidence (a) without ion bombardment, (b) with Ar bombardment of E = 50 eV & (j_I/j_V) = 0.04 (c) with Ar bombardment of E = 50 eV & (j_I/j_V) = 0.16: (B) (a) without ion bombardment, (b) with Ar bombardment of E = 10 eV & (j_I/j_V) = 0.16 (c) with Ar bombardment of E = 75 eV & (j_I/j_V) = 0.16 [56]

Ehiasarian et al. have investigated the effect of ion to neutral ratio and ion energy on the microstructure by varying the peak discharge current during the deposition of TiN films using HIPIMS. The density of the coatings was found to be increased with increasing peak discharge current since ion to neutral ratio and energy of the ions are directly proportional to the peak discharge current [57]. Hence it is well

understood that the microstructure of the coatings can be engineered by tuning the process parameters such as bias voltage, peak discharge current, etc.

2.5 Nanostructured coatings for implants

An ideal coating for knee implants should exhibit superior biocompatibility, mechanical, tribological and corrosion properties in vivo. A thin film of transition metal nitrides (TiN, CrN, NbN & TiCN, etc.) and their multilayers have been widely used for many industrial applications due to its high hardness, corrosion resistance and low wear etc. [58, 59]. The performance of the well-known TiN coating deposited on implants by a variety of techniques has been reported by various authors [60-62]. In 1988, Coll and Jacquot reported that TiN coating can be used to protect implants since TiN coated Ti6Al4V hip prosthetic head exhibited a lower UHMWPE wear rate than the uncoated head. In addition, the coating survived even after a 500 h hip simulator run. This coating was deposited by an arc technique [61]. Pham and co-workers have reported that that the biocompatibility of CoCr alloy was improved with TiN films by demonstrating the enhanced alkaline phosphatase (ALP) activity of MC3T3 cells (widely used model system in bone biology) which is a by-product of osteoblast activity (bone formation) along with cell proliferation behaviour. In this case, the coatings were deposited by reactive DC sputtering [62]. However, the failure of orthopaedic implants coated with TiN due to various factors such as in vivo fretting corrosion and third body abrasion (acrylic cement particle) has also been well documented by many authors [63, 64]. .

Multicomponent nanostructured coating such as TiCN exhibits high hardness, thermal stability and wear resistance compared to coatings such as TiN [65]. The biomedical application of Nb has been reported by Sader and co-workers [66]. Serro et al. suggested that TiN, TiNbN and TiCN may be used for biomedical applications since no cytotoxic effect was observed for them. Also, the wear rate of UHMWPE rubbed against TiNbN coated SS disc in the presence of albumin found to be

very low compared to TiN and TiCN coated discs. It has been reported that the TiNbN coating is used in commercially available hip and knee prosthesis [67]. Hamelynck has accounted that the corrosion and wear resistance of CoCrMo hip prosthetic component was improved with TiNbN coating deposited using physical vapour deposition. Due to this, the release of Cr ions from CoCrMo component was reduced by 90%. And, no symptoms of cytotoxicity were observed for TiNbN coated component [68]. The possibility of using three thick (8-12 μm) coatings, TiN, CrN and CrCN, and one thin (2 μm) diamond like carbon (DLC) coating for metal-on-metal hip prostheses was investigated by Fisher and co-workers [69].

Multilayer coatings can also be used for orthopaedic implants since they exhibit superior mechanical, tribological and corrosion performance compared to single layer coatings. Superlattice coatings are defined as nanometre-scale multilayers made of two different (materials) alternating layers with the bilayer thickness (superlattice period, Λ) of two materials typically ranging from 5 to 10 nm (Fig. 2.21). Literature suggests that the nitride and carbide based superlattice coatings are superhard materials with hardness in the range of 45 to 55 GPa. The hardness for various superhard multilayers is given in Table 2.1. It is well known that the overall hardness (H_o) value of the multilayer coatings exceeds the hardness value derived from the rule of mixture [70-72]:

$$H_o = V_{m1}H_{m1} + V_{m2}H_{m2} \tag{2.3}$$

Where V_{m1} and V_{m2} are the volume fractions material 1 and material 2 in the multilayers, H_{m1} and H_{m2} are the measured hardness values of individual layers of material 1 and material 2 in the multilayers [72].

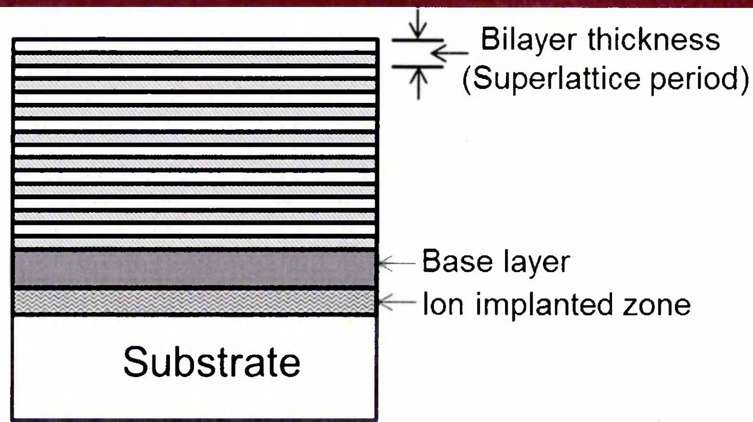

Figure 2.21 Schematic representation showing a multilayer structure

Table 2.1. Hardness of various multilayer coatings [70, 73]

Material	Hardness (GPa)	Young's modulus (GPa)
TiN/NbN	51	TiN: ~ 450 NbN: ~ 350 [74]
TiN/CN_x	45-55	TiN: ~ 450 CN_x: ~ 228 [75]
TiN/Nb	52	TiN: ~ 450 Nb: ~ 110 [76]
TiC/NbC	45-55	TiC: ~ 275 [77] NbC: ~ 375 [78]
TiN/Ti	36.8	TiN: ~ 450 Ti: ~ 110 [79]
TiCN/TiNbCN	42	TiCN: ~ 200 [77]

Hardness of the multilayer coatings varies with super lattice period (Λ). The hardness increases with increasing Λ, before attaining a saturation point. Further increases in Λ cause a slower decrease in the hardness values [80]. Several mechanisms have been proposed to explain the complex hardness enhancement phenomenon in the multilayer superlattice coatings. According to Koehler, the strength of materials can be increased by suppressing dislocation mobility through the formation of alternating layers of different materials. To achieve this, difference in dislocation line energy in the alternating layers should be large (large difference in elastic constant of the materials) and the layer thickness small enough so that dislocation generation (Frank-Read source) cannot occur inside a given layer [81]. Chu et al. proposed a model based on

dislocation glide within and between layers by investigating the difference in shear modulus between the layers to explain the superlattice hardening. The Hall-Petch type relationship (yield stress proportional to bilayer thickness) could also be attributed to the increased hardness since it has been argued that the superlattice layers will have a similar effect.

$$\sigma_y = \sigma_0 + k_l \Lambda^{-1/2} \tag{2.4}$$

Where σ_y is yield stress, σ_0 and k_l are constants and $\Lambda^{-1/2}$ is bilayer thickness. The coherency strain at the interface between the two layers also plays a minor role in the hardness enhancement [82]. It has been demonstrated that the TiAlCrN monolayer coating underwent plastic deformation which leads to delamination and crack formation deep (~ 200 nm) below the surface under high mechanical loads in dry sliding wear conditions. In contrast, the TiAlN/CrN superlattice coating experienced fine scale (~ 8 nm) delamination at the surface without any plastic deformation or perpendicular crack propagation [83].

Hübler and co-workers investigated the wear and corrosion performance of TiN, ZrN, Ti/TiN and Cr/V coatings deposited on 316L SS hip prosthetic femoral component. They have concluded that the Ti/TiN multilayer coating outperformed the other coatings when tested with mechanic wear simulator and cyclic voltammetry technique [84]. Caicedo et al. demonstrated that the corrosion resistance of 4140 steel substrate was improved with TiCN/TiNbCN multilayers deposited using RF magnetron sputtering. The several interfaces that present in the modulated structure act as barriers for corrosive ions to diffuse through the coating and reach the substrate. In addition, the diffusion of ions towards the substrate is inhibited due to the reduced number of pores present in the coating with increasing number of interfaces [85]. The performance of various multilayer coatings deposited using HIPIMS can be seen in Ref. 86-90. The coating-substrate adhesion and corrosion resistance of CrN/NbN multilayer coatings

(unbalanced magnetron sputtering) have been improved by Nb ion pre-treatment utilising HIPIMS compared to the same coating deposited after cathodic arc pre-treatment. Moreover, the corrosion resistance of the coating was further improved with the deposition of Nb interlayer utilising HIPIMS [91].

Plasma sprayed Hydroxyapatite (HA) coatings characterised by a calcium-phosphate-based material is used on total joint replacement components due to their good biocompatibility and bioactivity. However, the fatigue resistance of such coatings is found to be low. But human body joints are subjected to fatigue loading during day to day activities. These coatings exhibit increased surface micro-cracks and bulk porosity as well [92]. Diamond-like carbon coatings have also been proposed as potential candidates for protecting orthopaedic implants due to its chemical inertness, corrosion and wear resistance [93].

In summary, PVD coatings deposited with enhanced biocompatibility, mechanical, tribological and corrosion properties possess huge potential as protective layer on knee implants. And, the performance enhancement can be achieved by utilising HIPIMS for the deposition of such coatings.

References

1. CHAPMAN, Brian (1980). *Glow discharge processes: Sputtering and plasma etching.* First ed., United States of America, John Wiley & Sons.
2. GOLDSTON, Robert J. and RUTHERFORD, Paul H. (1997). *Introduction to plasma physics.* Second ed., United Kingdom, Institute of Physics Publishing.
3. MAISSEL, Leon I. and GLANG, Reinhard (eds.) (1983). *Handbook of thin film technology.* Reissue ed., United States of America, McGraw-Hill, Inc.
4. FARADAY, Michael (1857). Experimental relations of gold (and other metals) to light. *Philosphical transactions of the royal society of London,* **147**, 145-181.
5. HOLLAND, L. (1963). *Vacuum deposition of thin films.* Fifth ed., London, Chapman & Hall Ltd.
6. GROVE, W. R. (1852). On the electro-chemical polarity of gases. *Philosphical transactions of the royal society of London B,* **142**, 87-101.
7. PENNING, F. M., (1939). *Coatings by cathode disintegration.* United States of America Patent 2146025.
8. WAITS, Robert K. (1978). Planar magnetron sputtering. *Journal of vacuum science and technology,* **15,** 179-187.
9. SWANN, S. (1988). Magnetron sputtering. *Physics in tehnology,* **19,** 67-75.
10. KELLY, P. J. and ARNELL, R. D. (2000). Magnetron sputtering: A review of recent developments and applications. *Vacuum,* **56,** 15-172.
11. MCLEOD, P. S. and HARTSOUGH, L. D. (1977). High rate sputtering of aluminium for metallization of integrated circuits. *Journal of vacuum science and technology,* **14,** 263-265.

12. WINDOW, B. and SAVVIDES, N. (1986). Charged particle fluxes from planar magnetron sputtering sources. *Journal of vacuum science and technology A,* **4,** 196-201.

13. WINDOW, B. and SAVVIDES, N. (1986). Unbalanced dc magnetrons as sources of high ion fluxes. *Journal of vacuum science and technology A,* **4,** 453-456.

14. SAVVIDES, N. and WINDOW, B. (1986). Unbalanced magnetron ionassisted deposition and property modification of thin films. *Journal of vacuum science and technology A,* **4,** 504-508.

15. SPROUL, William D., et al. (1990). High rate reactive sputtering in an opposed cathode closed-field unbalanced magnetron sputtering system. *Surface and coatings technology,* **43–44,**270-278.

16. MÜNZ, W. -D., HOFFMANN, D. and HARTIG, K. (1982). A high rate sputtering process for the formation of hard friction-reducing TiN coatings on tools. *Thin solid films,* **96** (1), 79-86.

17. MÜNZ, W. -D (1986). Titanium aluminum nitride films: A new alternative to TiN coatings. *Journal of vacuum science and technology A,* **4** (6), 2717.

18. PETROV, I., et al. (1989). Microstructure modification of TiN by ion bombardment during reactive sputter deposition. Thin solid films, 169 (2), 299-314.

19. TEER, D. G., *Magnetron sputter ion plating.* United Kingdom Patent 2258343.

20. KELLY, P. J. and ARNELL, R. D. (1998). The influence of magnetron configuration on ion current density and deposition rate in a dual unbalanced magnetron sputtering system. *Surface and coatings technology,* **108–109**, 317-322.

21. SCHILLER, S., et al. (1993). Pulsed magnetron sputter technology. *Surface and coatings technology,* **61** (1–3), 331-337.

22. GRUEN, Reinar, (1991). Process and apparatus for coating conducting pieces using a pulsed glow discharge. United States of America Patent 5,015,493.

23. KELLY, P. J., et al. (1996). The deposition of aluminium oxide coatings by reactive unbalanced magnetron sputtering. *Surface and coatings technology,* **86–87**, 28-32.

24. JACKSON, G. N. (1970). R.F. sputtering. *Thin solid films,* **5** (4), 209-246.

25. HARTSOUGH, L. D. and MCLEOD, P. S. (1977). High-rate sputtering of enhanced aluminum mirrors. *Journal of vacuum science and technology,* **14,** 123-126.

26. NOWICKI, R. S. (1977). Properties of rf-sputtered Al_2O_3 films deposited by planar magnetron. *Journal of vacuum science and technology,* **14,** 127-133.

27. KOUZNETSOV, Vladimir, et al. (1999). A novel pulsed magnetron sputter technique utilizing very high target power densities. *Surface and coatings technology,* **122** (2–3), 290-293.

28. HELMERSSON, Ulf, et al. (2006). Ionized physical vapor deposition (IPVD): A review of technology and applications. *Thin solid films,* **513** (1–2), 1-24.

29. ANDERSON, Glen L., HAMMOND, Peter W., and YOTIVE, David S., (1993). Circuit for detecting and diverting an electrical arc in a glow discharge apparatus. United States of America Patent 5241152 A.

30. DRUMMOND, Geoffrey N., (1995). Thin film DC plasma processing system. United States of America Patent 5427669.

31. CHRISTIE, D. J., et al. (2004). Power supply with arc handling for high peak power magnetron sputtering. *Journal of vacuum science and technology A,* **22,** 1415-1418.

32. EHIASARIAN, A. P., et al. (2002). Influence of high power densities on the composition of pulsed magnetron plasmas. *Vacuum,* **65** (2), 147-154.

33. EHIASARIAN, A. P. and BUGYI, R. (2004). Industrial size high power impulse magnetron sputtering. In: *47th Annual Technical Conference Proceedings,* April 29-24. Dallas, United States of America, Society of Vacuum Coaters, 486-490.

34. MACÁK, Karol, et al. (2000). Ionized sputter deposition using an extremely high plasma density pulsed magnetron discharge. *Journal of vacuum science and technology A*, **18**, 1533-1537.

35. ROSSNAGEL, S. M. and KAUFMAN, H. R. (1988). Current-voltage relations in magnetrons. *Journal of vacuum science and technology A,* **6**, 223-229.

36. CHRISTIE, D. J. (2005). Target material pathways model for high power pulsed magnetron sputtering. *Journal of vacuum science and technology A,* **23,** 330-335.

37. ANDERS, André (2010). Deposition rates of high power impulse magnetron sputtering: Physics and economics. *Journal of vacuum science and technology A,* **28,** 783-790.

38. EHIASARIAN, A. P., WEN, J. G. and PETROV, I. (2007). Interface microstructure engineering by high power impulse magnetron sputtering for the enhancement of adhesion. *Journal of applied physics,* **101,** 054301.

39. SCHÖNJAHN, C., et al. (2000). Enhanced adhesion through local epitaxy of transition-metal nitride coatings on ferritic steel promoted by metal ion etching in a combined cathodic arc/unbalanced magnetron deposition system. *Journal of vacuum science and technology A,* **18,** 1718-1723.

40. EHIASARIAN, A. P., et al. (2003). High power pulsed magnetron sputtered CrN_x films. *Surface and coatings technology,* **163–164**, 267-272.

41. ANDERS, André *Cathodic arcs.* [online]. Last accessed 08/07/2013 at: http://escholarship.ucop.edu/uc/item/5km1m68m.

42. DAVIS, W. D. and MILLER, H. C. (1969). Analysis of the electrode products emitted by dc arcs in a vacuum ambient. *Journal of applied physics,* **40** (5), 2212-2221.

43. BOXMAN, Raymond L., MARTIN, Philip J. and SANDERS, David M. (eds.) (1995). *Hand book of vacuum arc science and technology: Fundamentals and applications.* New Jersey, United States of America, Noyes Publications.

44. EHIASARIAN, A. P. (2002). *Development of PVD coating processes informed by plasma diagnostics.* PhD Thesis. Sheffield Hallam University.

45. ANDERS, Andre, et al. (1996). High-resolution imaging of vacuum arc cathode spots. *Plasma science, IEEE transactions on,* **24** (1), 69-70.

46. MARTIN, P. J., et al. (1987). Characteristics of titanium arc evaporation processes. *Thin solid films,* **153** (1–3), 91-102.

47. PETROV, I., et al. (1997). Ion-assisted growth of $Ti_{1-x}Al_xN/Ti_{1-y}Nb_yN$ multilayers by combined cathodic-arc/magnetron-sputter deposition. *Thin solid films,* **302** (1–2), 179-192.

48. WANG, H. W., et al. (2000). The corrosion behaviour of macroparticle defects in arc bond-sputtered CrN/NbN superlattice coatings. *Surface and coatings technology,* **126** (2–3), 279-287.

49. RAMALINGAM, Subbiah, CAI, B. Qi and KYUNGHOON, Kim, (1987). *Controlled vacuum arc material deposition, method and apparatus.* United States of America Patent 4,673,477 .

50. ANDERS, André (1999). Approaches to rid cathodic arc plasmas of macro- and nanoparticles: A review. *Surface and coatings technology,* **120–121** (0), 319-330.

51. BARNA, P. B. and ADAMIK, M. (1998). Fundamental structure forming phenomena of polycrystalline films and the structure zone models. *Thin solid films,* **317** (1–2), 27-33.

52. THOMPSON, C. V. (2000). Structure evolution during processing of polycrystalline films. *Annual review of materials science,* **30** (1), 159.

53. THORNTON, John A. (1977). High rate thick film growth. *Annual review of materials science,* **7,** 239-260.

54. MESSIER, R., GIRI, A. P. and ROY, R. A. (1984). Revised structure zone model for thin film physical structure. *Journal of vacuum science and technology A,* **2,** 500-503.

55. MATTOX, D. M. and KOMINIAK, G. J. (1972). Structure modification by ion bombardment during deposition. *Journal of vacuum science and technology A,* **9,** 528.

56. MÜLLER, K. H. (1987). Ion beam induced epitaxial vapour- phase growth: A molecular-dynamics study. *Physical review B,* **35,** 7906.

57. EHIASARIAN, A. P., et al. (2011). Influence of high power impulse magnetron sputtering plasma ionization on the microstructure of TiN thin films. *Journal of applied physics,* **109,** 104314.

58. SUBRAMANIAN, C. and STRAFFORD, K. N. (1993). Review of multicomponent and multilayer coatings for tribological applications. *Wear,* **165** (1), 85-95.

59. HOVSEPIAN, P. Eh, LEWIS, D. B. and MÜNZ, W. -D (2000). Recent progress in large scale manufacturing of multilayer/superlattice hard coatings. *Surface and coatings technology,* **133-134**, 166-175.

60. WISBEY, A., GREGSON, P. J. and TUKE, M. (1987). Application of PVD TiN coating to Co-Cr-Mo based surgical implants. *Biomaterials,* **8** (6), 477-480.

61. COLL, Bernard F. and JACQUOT, Patrick (1988). Surface modification of medical implants and surgical devices using TiN layers. *Surface and coatings technology,* **36** (3–4), 867-878.

62. PHAM, Vuong-Hung, et al. (2011). Deposition of TiN films on Co-Cr for improving mechanical properties and biocompatibility using reactive DC sputtering. *Journal of materials science: Materials in medicine,* **22** (10), 2231-2237.

63. TERESA RAIMONDI, Manuela and PIETRABISSA, Riccardo (2000). The in-vivo wear performance of prosthetic femoral heads with titanium nitride coating. *Biomaterials,* **21** (9), 907-913.

64. HARMAN, Melinda K., BANKS, Scott A. and HODGE, W. Andrew (1997). Wear analysis of a retrieved hip implant with titanium nitride coating. *The journal of arthroplasty,* **12** (8), 938-945.

65. BULL, S. J., BHAT, D. G. and STAIA, M. H. (2003). Properties and performance of commercial TiCN coatings. Part 2: Tribological performance. *Surface and coatings technology,* **163–164**, 507-514.

66. SADER, M. S., et al. (2002). Niobium for biomedical applications: In Vitroevaluation. *Acta Microscopica,* **11,** 49-52.

67. SERRO, A. P., et al. (2009). A comparative study of titanium nitrides, TiN, TiNbN and TiCN, as coatings for biomedical applications. *Surface and coatings technology,* **203** (24), 3701-3707.

68. HAMELYNCK, Karel J. (2010). *Ceramic surface engineered metal-on-metal hips system for total hip arthroplasty and resurfacing hip arthroplasty.* White paper.

69. FISHER, J., et al. (2004). Wear of surface engineered metal-on-metal hip prostheses. *Journal of materials science: Materials in medicine,* **15,** 225-235.

70. MUSIL, J. (2000). Hard and superhard nanocomposite coatings. *Surface and coatings technology,* **125** (1–3), 322-330.

71. BARSHILIA, Harish C. and RAJAM, K. S. (2004). Structure and properties of reactive DC magnetron sputtered TiN/NbN hard superlattices. *Surface and coatings technology,* **183** (2–3), 174-183.

72. RUDD, J. A., JERVIS, T. R. and SPAEPEN, F. (1994). Nanoindentation of Ag/Ni multilayered thin films. *Journal of applied physics,* **75** (10), 4969-4973.

73. CAICEDO, J. C., et al. (2010). TiCN/TiNbCN multilayer coatings with enhanced mechanical properties. *Applied surface science,* **256** (20), 5898-5904.

74. FULCHER, B. D., et al. (2012). Hardness analysis of cubic metal mononitrides from first principles. *Physical review B,* **85**, 184106.

75. AKIYAMA, M., et al. (2001). Optimizing hardness of CNx thin films by dc magnetron sputtering and a statistical approach. *Journal of materials science,* **36** ,5397

76. MONDAL, Jayanta, ROY, A. and MITTAL, K. C. *Optimization of wall thickness of superconducting 700 MHz bulk niobium and niobium coated OFHC cavities by thermal/structural analysis.* India, Bhabha Atomic Research Centre.

77. FANG, Te-Hua, JIAN, Sheng-Rui and CHUU, Der-San (2004). Nanomechanical properties of TiC, TiN and TiCN thin films using scanning probe microscopy and nanoindentation. *Applied surface science,* **228** (1–4), 365-372.

78. ZOU, Guifu, et al. (2010). A chemical solution approach for superconducting and hard epitaxial NbC film. *The royal society of chemistry,* **46,** 7837.

79. VIJGEN, R. O. E. and DAUTZENBERG, J. H. (1995). Mechanical measurement of the residual stress in thin PVD films. *Thin solid films,* **270** (1–2), 264-269.

80. HELMERSSON, U., et al. (1987). Growth of single-crystal TiN/VN strained-layer superlattices with extremely high mechanical hardness. *Journal of applied physics,* **62** (2), 481-484.

81. KOEHLER, J. S. (1970). Attempt to design a strong solid. *Physical review B,* **2** (2), 547-551.

82. CHU, Xi and BARNETT, Scott A. (1995). Model of superlattice yield stress and hardness enhancements. *Journal of applied physics,* **77,** 4403-4411.

83. LUO, Q., RAINFORTH, W. M. and MÜNZ, W. -D (1999). TEM observations of wear mechanisms of TiAlCrN and TiAlN/CrN coatings grown by combined steered-arc/unbalanced magnetron deposition. *Wear,* **225–229,** 74-82.

84. HÜBLER, R., et al. (2001). Wear and corrosion protection of 316-L femoral implants by deposition of thin films. *Surface and coatings technology,* **142-144,** 1078-1083.

85. CAICEDO, J. C., et al. (2011). Corrosion surface protection by using titanium carbon nitride/titanium–niobium carbon nitride multilayered system. *Thin solid films,* **519** (19), 6362-6368.

86. HOVSEPIAN, P. Eh, EHIASARIAN, A. P. and RATAYSKI, U. (2009). CrAlYCN/CrCN nanoscale multilayer PVD coatings deposited by the combined high power impulse magnetron Sputtering/Unbalanced magnetron sputtering (HIPIMS/UBM) technology. *Surface and coatings technology,* **203** (9), 1237-1243.

87. HOVSEPIAN, Papken Eh, et al. (2009). Effect of high ion irradiation on the structure, properties and high temperature tribology of nanoscale CrAlYN/CrN multilayer coating deposited by HIPIMS-HIPIMS technique. *Plasma processes and polymers,* **6,** S118-S123.

88. PAULITSCH, J., et al. (2008). Structure and mechanical properties of CrN/TiN multilayer coatings prepared by a combined HIPIMS/UBMS deposition technique. *Thin solid films,* **517** (3), 1239-1244.

89. HOVSEPIAN, P. Eh, et al. (2008). Novel TiAlCN/VCN nanoscale multilayer PVD coatings deposited by the combined high-power impulse magnetron sputtering/unbalanced magnetron sputtering (HIPIMS/UBM) technology. *Vacuum,* **82** (11), 1312-1317.

90. PURANDARE, Y. P., et al. (2010). CrN/NbN coatings deposited by HIPIMS: A preliminary study of erosion–corrosion performance. *Surface and coatings technology,* **204** (8), 1158-1162

91. REINHARD, C., EHIASARIAN, A. P. and HOVSEPIAN, P. Eh (2007). CrN/NbN superlattice structured coatings with enhanced corrosion resistance achieved by high power impulse magnetron sputtering interface pre-treatment. *Thin solid films,* **515** (7–8), 3685-3692.

92. LIANG, Hong, et al. (2004). Applications of plasma coatings in artificial joints: An overview. *Vacuum,* **73** (3–4), 317-326.

93. RILL, A. (2003). Diamond-like carbon coatings as biocompatible materials—an overview. *Diamond and related materials,* **12** (2), 166-170.

Chapter 3

3 Materials and Methods

3.1 Materials, Substrate preparation and deposition of various coatings

3.1.1 Substrate materials

TiN and TiN/NbN, TiCN/NbCN and CrN/NbN multilayer coatings were deposited on M2 high speed steel (HSS), 316 stainless steel (SS), CoCr alloy and silicon substrates of different dimensions shown in Fig. 3.1. Table 3.1 lists the various substrate materials, dimensions and its usage.

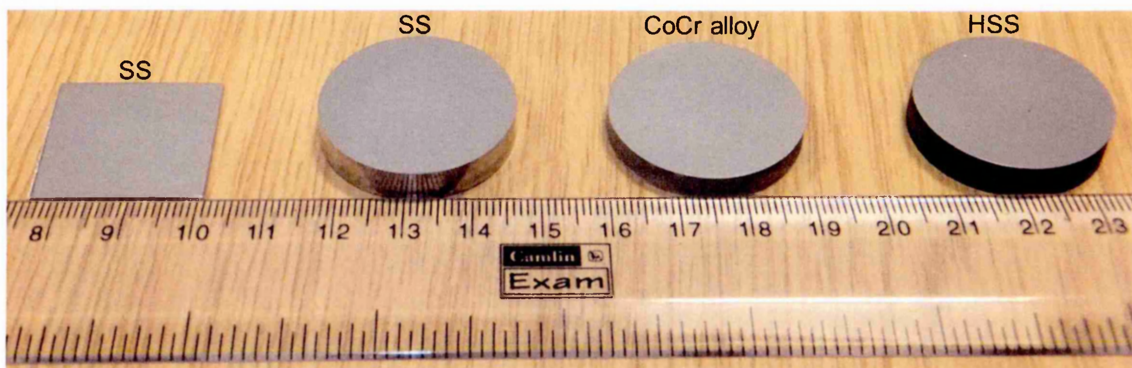

Figure 3.1 Various substrates used for the deposition of TiN and multilayer coatings

Table 3.1 Various substrate materials, dimensions and its usage

Material	Dimension	Tests
M2 HSS	30 mm x 6 mm coupon	Adhesion strength, Nanohardness and Tribology
316 SS	30 mm x 6 mm coupon	Corrosion, XRD
316 SS	25 mm x 25 mm x 0.8 mm sheet	Transmission electron microscopy
CoCr alloy	30 mm x 6 mm coupon	Nanohardness, Corrosion, XRD and Tribology
Silicon	5 mm x 5 mm x 1 mm	Scanning electron microscopy

3.1.2 Substrate preparation prior to coating deposition

The substrate preparation prior to coating deposition involved mechanical grinding, polishing and cleaning using hot alkaline saponifiers which convert organic fats to water soluble soaps. For the mechanical grinding, 180, 320, 600, 1200 and 4000 grit abrasive papers were used. For the mechanical polishing, different kinds of cloth pads were used with 9, 6 and 1 μm diamond fluid and lubricant. The mirror polished substrates were cleaned in an industrial size ultrasonic cleaning line comprising of various commercially available alkaline solutions, tap water and de-ionized (DI) water. Subsequently, the substrates were subjected to drying in the vacuum dryer attached to the cleaning line. Table 3.2 shows the sequence of cleaning procedure performed using ultrasonic cleaning line after polishing the substrates.

Table 3.2. Sequence of the cleaning procedure

Step	Solution	Temperature (°C)	Time (min)
1	DI water + Deconex HT 015 + Deconex HT 1169	~ 60	~ 15
2	Tap water rinsing	room	~ 1
3	DI water + Deconex VP 1233A	~ 60	~ 15
4	Tap water rinsing	room	~ 1
5	DI water	~ 50	~ 5
6	DI water rinsing	~ 50	~ 1
7	Vacuum drying	~ 100	~ 40

3.1.3 Industrial size coating machine enabled with HIPIMS technology

The industrial size, HIPIMS technology enabled coating machine, HTC 1000-4 manufactured by Hauzer Techno Coating (The Netherlands) was used for the deposition

of the coatings. Fig. 3.3 represents schematic of horizontal cross section of such coating machine.

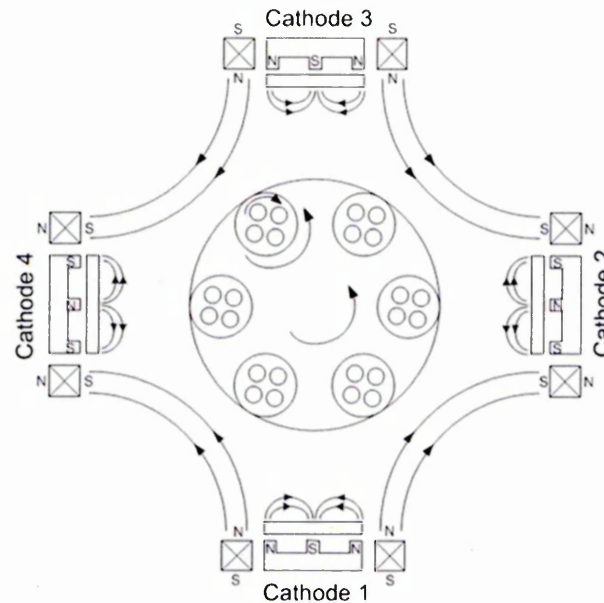

Figure 3.2 Schematic of horizontal cross section of the industrial size sputtering machine

Two roughing pumps such as roots pump and rotary vane pump were used to achieve rough vacuum in the pressure range of about 8 Pa. Two turbo molecular pumps were in operation to evacuate the chamber to a base pressure of better than .0075 Pa. The total pressure was measured using a viscosity pressure gauge (Leybold Viscovac VM212). The machine was equipped with four cathodes (target area of 1200 cm^2 each) which were able to operate in either unbalanced magnetron sputtering or HIPIMS mode by switching the power supply. Four dc power generators and two HIPIMS power generators (HMP2/1) supplied by Hüttinger Electronic Sp. z.o.o. (Poland) were connected to the coating machine. The HIPIMS power supply was capable of delivering peak currents of up to 3000 A and at a voltage of 2000 V. A specialised HIPIMS compatible bias power supply (Model: HBP, Hüttinger Electronic Sp. z.o.o., Poland) was used to maintain a stable bias voltage during the surface pre-treatment as well as the coating deposition processes. Arcing energy was minimized by arc suppression design that stops the power supply in the event of maximum current. Each cathode was

provided with a movable magnetic confinement array, capable of producing a range of magnetic field strengths from 40 mT to 10 mT. Additionally, each cathode was surrounded by electromagnetic coils by which the magnetic field strength on the target surface can be varied. The substrates were mounted on the turntable located in the centre of the chamber which can be rotated one or two or three fold rotation. Fig. 3.4 shows the photographs of HTC 1000-4 coating machine and HIPIMS power supply.

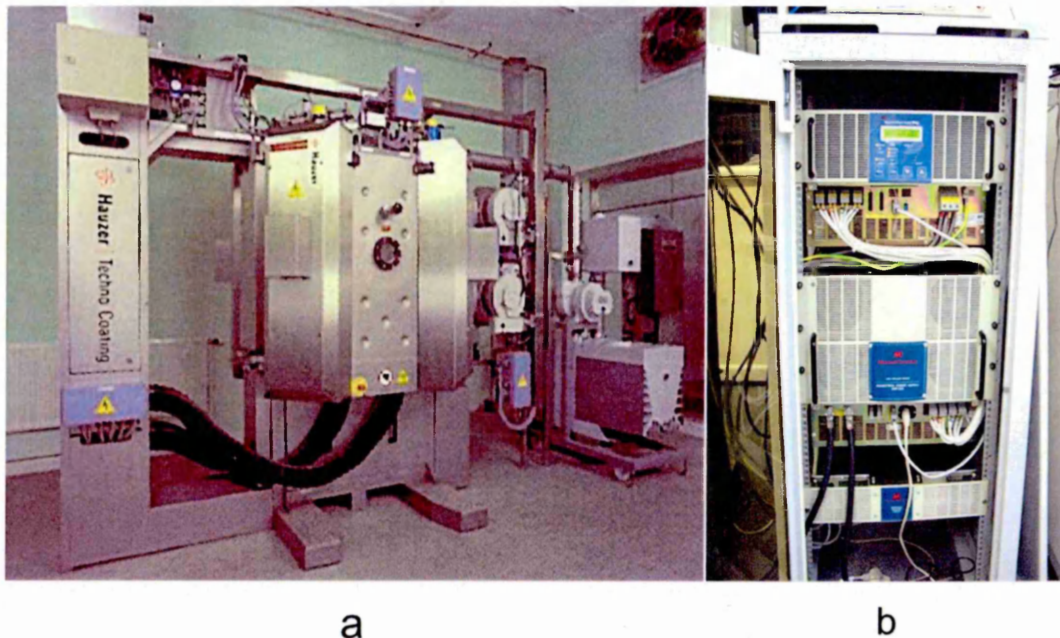

Figure 3.3 a) Photograph of HTC 1000-4 coating machine b) Photograph of HIPIMS power supply

3.1.4 Protocol followed for the experiments

Step 1: Achievement of high vacuum & baking operation

The coating chamber was evacuated using a combination of rotary vane pump, roots pump and two turbo molecular pumps to achieve base pressure of better than 0.0075 Pa. The temperature of the chamber and its contents was raised to accelerate the desorption of gases and vapours (degassing) by baking facilitated by two heaters attached to the chamber walls. The suitable substrate temperature was also achieved by the baking operation. The substrates were subjected to three fold rotations for all the experiments with 35% rotation speed.

Step 2: Target cleaning

The impurities and other contaminants on the target surface were sputtered-off by applying a low potential to the targets in the presence of an inert sputtering gas such as Argon. The shutters are placed in front of the targets during the target cleaning to prevent substrate contamination.

Step 3: Substrate pre-treatment by metal ion etching using HIPIMS

The substrates were bombarded with $M^{+}Ar^{+}$ mixture (M ion and Ar ion) generated in Ar glow discharge plasma by applying a high potential of -1000 V to the target using a HIPIMS generator. The observed peak current was about 1.24 kA during the process. The ion mixture was accelerated towards the substrate by applying a high bias voltage of about -1000 V. Because of this, the substrate was sputter cleaned and a shallow metal ion implanted zone was also produced in the substrate. The metal ion zone enhances the coating-substrate adhesion considerably.

Step 4: Deposition of base layer

A base layer was deposited further to improve the adhesion between the coating and the substrate.

Step 5: Deposition of coatings

The monolayer and multilayer (superlattices) coatings were deposited using various target combinations by varying the process parameters such as substrate bias voltage, coil current and total pressure etc.

Step 6: Cooling down and venting the chamber

The substrates were allowed to cool down before venting the chamber.

3.1.5 Deposition of TiN coatings

TiN coatings were deposited by utilizing pure UBM, combined HIPIMS/UBM and pure HIPIMS source combinations. Four different source combinations were exploited with increasing degree of HIPIMS contribution as follows: 4 cathodes in

conventional dc-UBM mode to deposit pure UBM coating, 1HIPIMS + 3UBM and 2HIPIMS + 2UBM source combinations to deposit combined HIPIMS/UBM coatings and 2HIPIMS cathodes to deposit pure HIPIMS coatings. Fig. 3.4 (a-d) shows the schematic representation of various source combinations used for the deposition of TiN coatings.

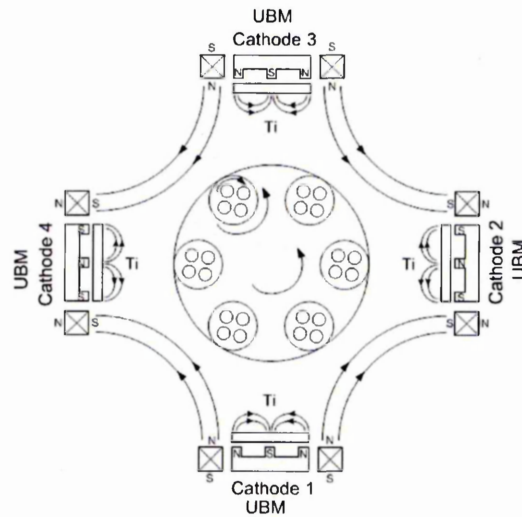

Figure 3.4 (a) Schematic of pure UBM source set-up

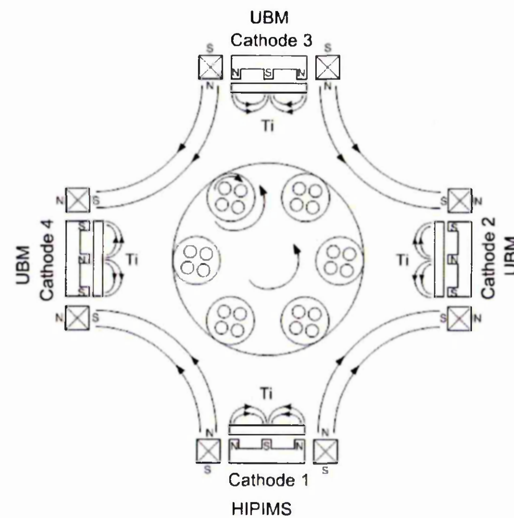

Figure 3.4 (b) Schematic of 1HIPIMS + 3UBM source set-up

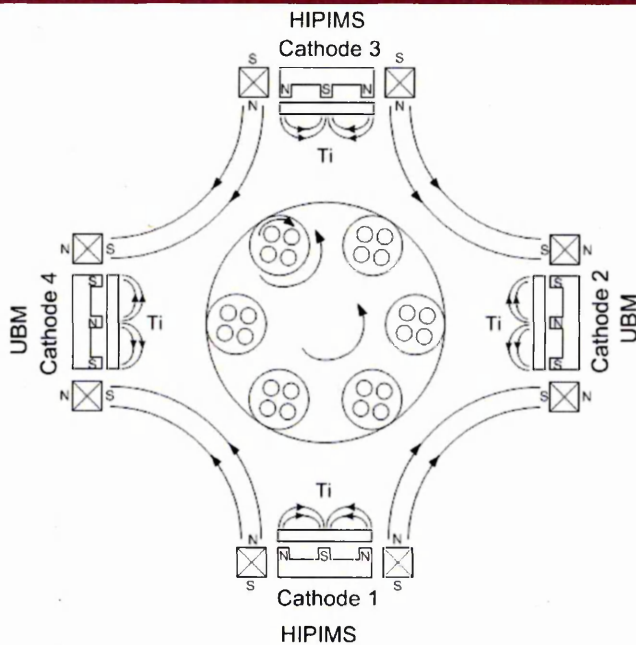

Figure 3.4 (c) Schematic of 2HIPIMS + 2UBM source set-up

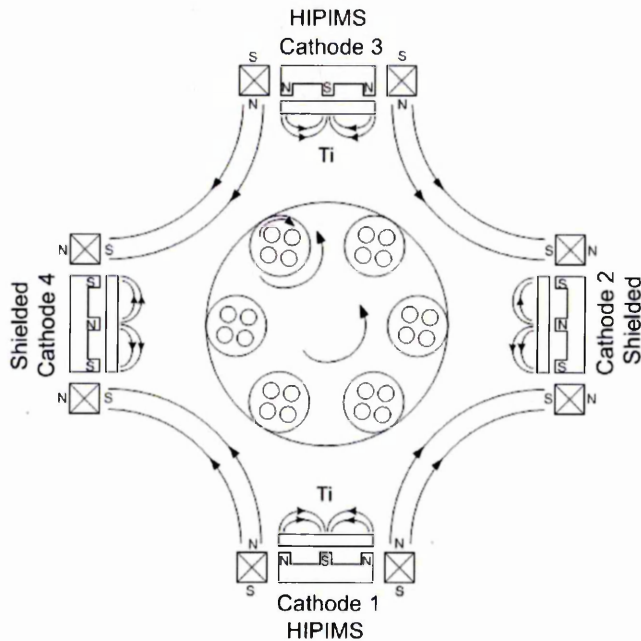

Figure 3.4 (d) Schematic of 2HIPIMS source set-up

All the four cathodes were furnished with 99.99 % pure Ti targets (1200 cm^2) manufactured by GfE, Germany. The deposition of TiN coatings were carried out in Ar + N_2 atmosphere at 400 °C by varying the substrate bias, coil current and total pressure. Table 3.3 lists the various process parameters used for the deposition.

Table 3.3 Various process parameters used for the deposition of TiN coatings

Process parameters	Base layer (Ti)	TiN coating
Target power (kW)	8	8
Target Voltage (V)	~ 400 & ~ 650	~ 400 & ~ 650
Target Current (A)	~ 17 & ~ 14	~ 17 & ~ 14
Substrate bias (V)	0, -50 & -75	0, -50 & -75
Substrate temperature (°C)	400	400
Total pressure (Pa)	0.32	0.22, 0.25,0.30, 0.33 & 0.35
Coil current (A)	0, 3 & 6	0, 3 & 6
Peak target current (A) (HIPIMS)	~ 300	~ 300

3.1.6 Deposition of TiN/NbN multilayer coatings

TiN/NbN multilayer coatings were deposited using combined HIPIMS/UBM sources. Cathode 1 & cathode 2 were furnished with 99.99 % pure Nb targets (1200 cm^2) and cathode 3 & cathode 4 were furnished with 99.99 % pure Ti targets (1200 cm^2). Two source combinations such as 1HIPIMS + 3UBM and 2HIPIMS + 2UBM were used for this purpose. The deposition of these were carried out in Ar + N_2 atmosphere Fig. 3.5 shows the schematic representation of the two source combinations used for the deposition. Table 3.4 shows the various process parameters used for the deposition.

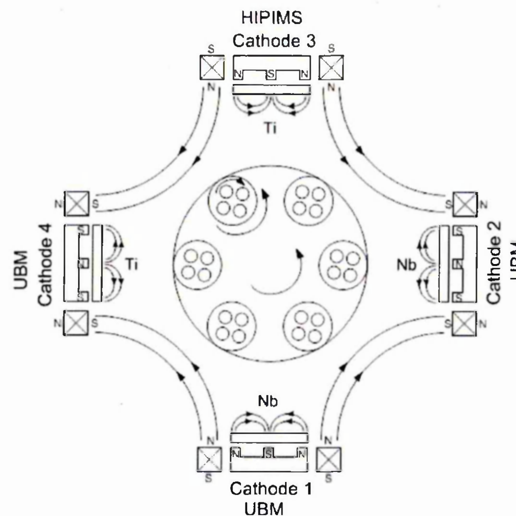

Figure 3.5 (a) Schematic of 1HIPIMS + 3UBM source set-up

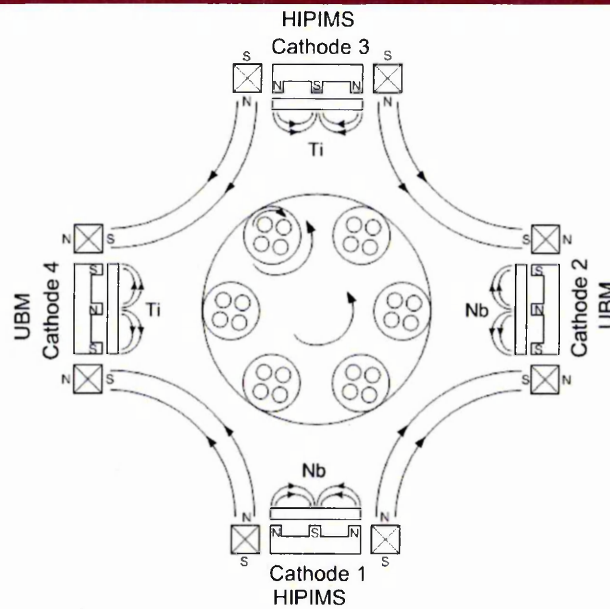

Figure 3.5 (b) Schematic of 2HIPIMS + 2UBM source set-up

Table 3.4 Various process parameters used for the deposition of TiN/NbN multilayer coatings

Process parameters	Base layer (TiN)	TiN/NbN coating
Target power (kW)	8	8
Target voltage (V)	~ 500 & ~ 650	~ 500 & ~ 650
Target current (A)	~ 17 & ~ 14	~ 17 & ~ 14
Substrate bias (V)	-50	-50
Substrate temperature (°C)	400	400
Total pressure (Pa)	0.3	0.3
Coil current (A)	3	3
Peak target current (A) (HIPIMS)	~ 300	~ 300

3.1.7 Deposition of TiCN/NbCN multilayer coating

TiCN/NbCN multilayer coating was deposited using combined HIPIMS/UBM sources. The 1HIPIMS + 3UBM source combination with two Ti and two Nb targets [Fig. 3.6(a)] was used for this purpose. The deposition of these coatings was carried out in Ar + N_2 + CH_4 atmosphere. Table 3.5 shows the various parameters used for the deposition.

Table 3.5 Various process parameters used for the deposition of TiCN/NbCN multilayer coating

Process parameters	Base layer (TiN)	TiCN/NbCN coating
Target power (kW)	8	8
Target voltage (V)	~ 500	~ 550 & ~ 650
Target current (A)	~ 17	~ 14
Substrate bias (V)	-75	-75
Substrate temperature (°C)	400	400
Total pressure (Pa)	0.35	0.397
Coil current (A)	6	6
Peak target current (A) (HIPIMS)	0	~ 300

3.1.8 Deposition of CrN/NbN multilayer coating

CrN/NbN multilayer coating was deposited using combined HIPIMS/UBM sources. The 2HIPIMS + 2UBM source combination with two Nb and two Cr targets (Fig. 3.6) was used for this purpose. The deposition of this coating was carried out in Ar + N_2 atmosphere. Table 3.6 shows the various process parameters used for the deposition.

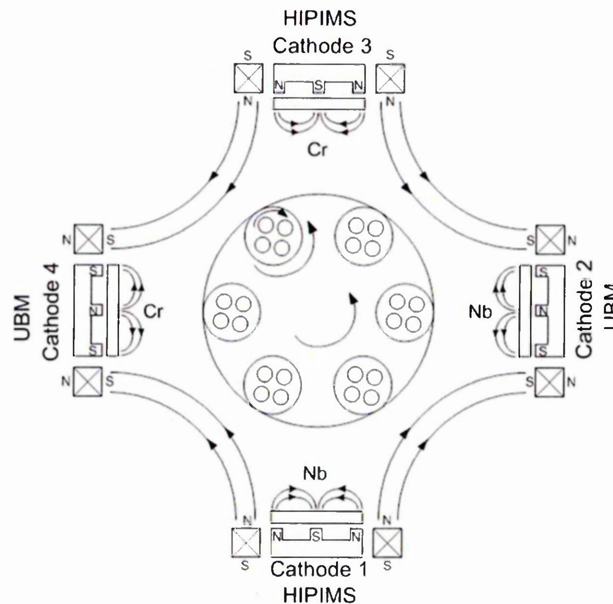

Figure 3.6 Schematic of 2HIPIMS + 2UBM source set-up

Table 3.6 Various process parameters used for the deposition of TiCN/NbCN multilayer coating

Process parameters	Base layer (CrN)	CrN/NbN coating
Target power (kW)	0.4 & 8	8
Target voltage (V)	~ 250 & ~ 650	~ 500 & ~ 650
Target current (A)	~ 11 & ~ 14	~ 11 & ~ 14
Substrate bias (V)	-65	-65
Substrate temperature (°C)	400	400
Total pressure (Pa)	0.36	0.35
Coil current (A)	4	4
Peak target current (A) (HIPIMS)	~ 300	~ 300

3.2 Plasma diagnostics

Optical Emission Spectroscopy (OES) was used to analyse the plasma since it is proven to be successful in determining the type and charge state of metal and gas species in the plasma. OES spectra of TiN plasma generated by the various combinations of HIPIMS and UBM sources were recorded using a Czerny-Turner type monochromator (Triax 320 - Jobin Yvon) with quartz optical fibre and collimator in time-averaged mode *in vacuo*. The Czerny-Turner type monochromator consists of a plane grating and two concave mirrors as shown in Fig. 3.7. The plane grating facilitates dispersion and the concave mirrors facilitate focusing. The light entering the monochromator through an entrance slit is collimated onto a plane grating by the concave mirror 1. The incident light on the surface of the grating is then diffracted toward the concave mirror 2. A schematic representation of diffraction by a plane reflection grating is shown in Fig. 3.8. The grating is rotated in order to move it normal relative to the incident and diffracted beams, which changes (by the grating equation, Eq. 3.1) the wavelength diffracted toward the concave mirror 2. Subsequently, the diffracted light is collimated and focussed toward an exit slit by the concave mirror 2.

The intensity of the light at the exit slit is measured by a photomultiplier tube (PMT) or a charge-coupled device (CCD) detector against wavelength.

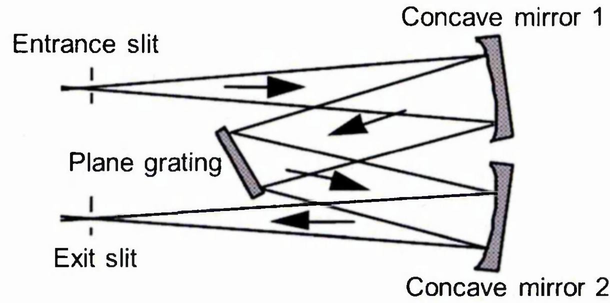

Figure 3.7 Schematic of Czerny-Turner monochromator [Ref.1]

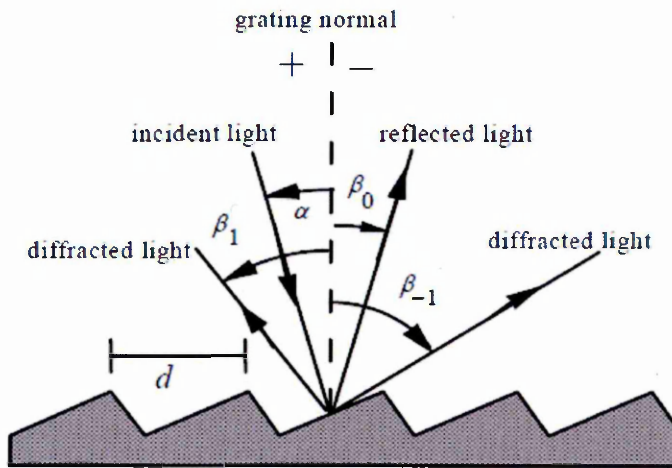

Figure 3.8 Schematic of diffraction by a plane reflection grating [Ref.1]

The grating equation is written as

$$m\lambda = d(\sin\alpha + \sin\beta) \tag{3.1}$$

where m is the diffraction order, λ is the wavelength of light diffracted from a grating, d is the groove spacing, α is the angle of light incident on a grating and β is the angle of diffracted light from a grating.

The quartz fibre capable of transmitting in the ultraviolet spectral region was kept in the substrate region in order to analyse the plasma confined near the substrates. Fig. 3.9 depicts the placement of the optical fibre kept inside the chamber during OES measurements. The orifice of the quartz fibre was facing downwards to be able to see the mixed plasma and not only certain target areas as targets were on opposing sides.

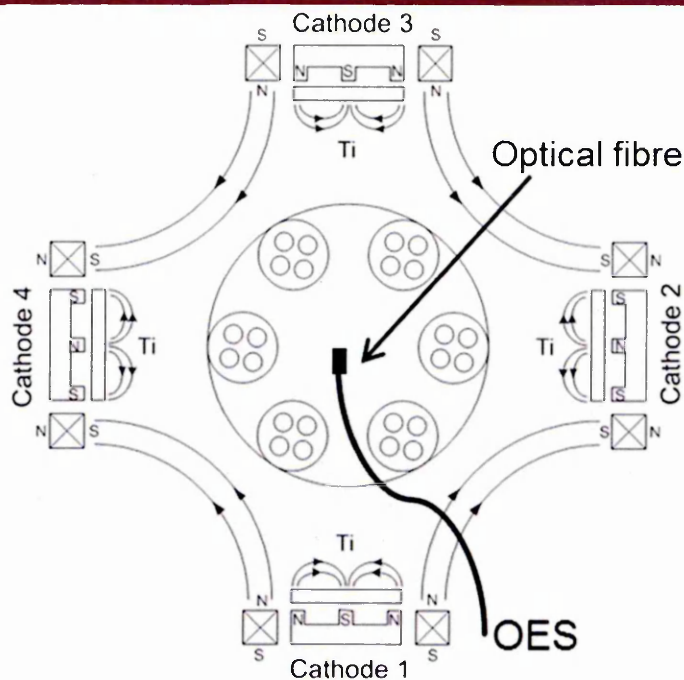

Figure 3.9 Schematic of OES set-up

Emission lines from the spectrum have been identified using NIST atomic spectra database [2] and Ref. 3. Table 3.7 lists the emission lines used in this study.

Table 3.7. List of emission lines used

Species	Oscillator strength (f_{ik})	Wavelength (nm)	Upper excitation energy (eV)	Lower excitation energy (eV)
Ti^{1+}	0.0035	367.968	4.05	1.58
Ti^{0}	0.0053	364.6196	3.4	0
N_2^{0} $C^3\Pi_u$ - $B^3\Pi_g$; (0-2)*	-	380.49	11.18	7.92

* Spectroscopic notation of the excited and ground state energy bands of N_2^{0} species

The chosen Ti species lines have similar wavelengths, similar upper excitation energies and similar oscillator strengths. Considering the intensity ratio of these lines is ideal for a qualitative statement on the effect of HIPIMS utilisation on the ionisation of metal. The intensity ratios of Ti^{1+}, Ti^{0} and N_2^0 to intensity ratios of all Ti species (Ti^{1+}+ Ti^{0}) in the plasma are considered to extract information about the 'weighted emission intensity' of Ti^{1+}, Ti^{0} and N_2^0. To improve the accuracy of the estimates, the oscillator

strengths for Ti^0 and Ti^{1+} were used in the calculation, assuming that the line intensity I ~ f_{ik}*n, where f_{ik} is the oscillator strength and n is the density of species. The following relations were used to estimate the 'weighted emission intensity' of Ti^{1+}, Ti^0 and N_2^0.

$$\{Ti^{1+}\} = \frac{\frac{Ti^{1+}}{f_{ik}^{Ti^{1+}}}}{\left(\frac{Ti^{1+}}{f_{ik}^{Ti^{1+}}}+\frac{Ti^{0}}{f_{ik}^{Ti^{0}}}\right)} \quad (3.2)$$

$$\{Ti^{0}\} = \frac{\frac{Ti^{0}}{f_{ik}^{Ti^{0}}}}{\left(\frac{Ti^{1+}}{f_{ik}^{Ti^{1+}}}+\frac{Ti^{0}}{f_{ik}^{Ti^{0}}}\right)} \quad (3.3)$$

$$\{N_2^0\} = \frac{N_2^0}{\left(\frac{Ti^{1+}}{f_{ik}^{Ti^{1+}}}+\frac{Ti^{0}}{f_{ik}^{Ti^{0}}}\right)} \quad (3.4)$$

where Ti^{1+}, Ti^0 and N_2^0 are the emission line intensities of Ti^{1+} ions, Ti^0 neutrals, and N_2^0 neutrals, respectively. $f_{ik}^{Ti^0}$ and $f_{ik}^{Ti^{1+}}$ are the oscillator strengths of Ti^0 and Ti^{1+}, respectively. Due to the use of oscillator strength, the 'weighted emission intensity' is proportional to the density of species in the plasma. However, the coefficient of proportionality could not be measured. Therefore the 'weighted emission intensity' is only a qualitative measure of the density of species. The excitation energies for N_2 are significantly higher than Ti^0 and Ti^{1+} and as such the ratios are dependent on the electron temperature.

3.3 Thin film characterisation techniques

3.3.1 X-ray Diffraction analysis

The structural characteristics of the coatings were investigated by X-ray diffraction (Philips Xpert PW 3050/60 diffractometer) using Bragg-Brentano (BB) geometry and glancing angle parallel beam geometry. The diffraction was carried on all of the coatings using Cu K_α (λ = 0.154060 nm) radiation. XRD is governed by the well-known Bragg's law (Eq. 3.5) which relates the wavelength of electromagnetic radiation to the diffraction angle and the lattice spacing in a crystalline structure. Fig. 3.10 shows

the diffraction of X-rays by planes of atoms. Constructive interference of the scattered (1' and 2') beams occurs when

$$n\lambda = 2\, d \sin\theta \qquad (3.5)$$

where n is the order of reflection, λ is wavelength of incident ray, d is spacing between the planes in the atomic lattice and θ is Bragg angle (x-ray incident angle).

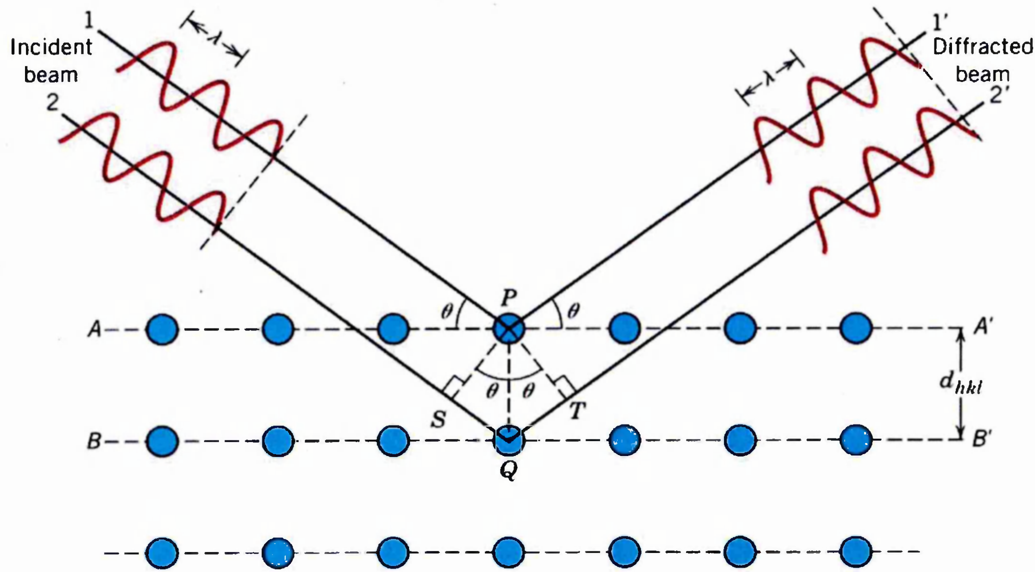

Figure 3.10 Schematic of diffraction of X-rays by planes of atoms [Ref.4]

3.3.1.1 Determination of coefficient of texture

The BB (θ-θ) geometry was used with an angular step size of 0.03° between 2θ values of 20° and 130° for the purpose of determining the texture. A system with BB θ-θ geometry is shown in Fig. 3.11. In this geometry, the sample remains stationary and the detector and x-ray source rotate [5].

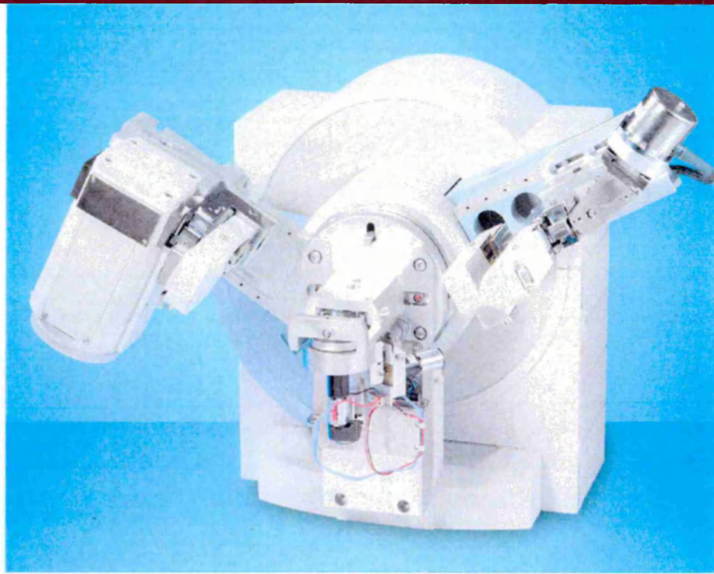

Figure 3.11 Bragg-Brentano θ-θ Geometry [Ref.6]

Texture coefficient for the reflection (T*) was calculated from the Eq. 3.6 [7-8]:

$$T^* = \frac{I_{hkl}/R_{hkl}}{(1/n)\sum_0^n (I_{hkl}/R_{hkl})} \quad (3.6)$$

where $I_{(hkl)}$ is the measured peak intensity from the (hkl) reflections, $R_{(hkl)}$ is the reference standard (random) peak intensity from the (hkl) reflections and n is the number of reflections considered. The JCPDS values of peak intensity were used as the standard reference (R_{hkl}) intensity values since it was not possible to determine R_{hkl} intensity values for a randomly oriented coating material [7-8].

3.3.1.2 Determination of residual stress

Glancing angle geometry was used for determining the residual stress in the coatings. The angle of incidence to the substrate was fixed at a low angle of 1°. The sample to be analysed was stationary and the detector was rotated. The low angle of incidence reduces the penetration of x-rays into the sample which in turn limits the depth from which information is collected.

Stress (σ) was calculated from the slope of the least-squares fit of the plot of a_Ψ versus $\sin^2\Psi$ and using the following expression (Eq. 3.7) [8]:

$$\sigma = \frac{\text{Slope E}}{a_\Psi (1+\nu)} \quad (3.7)$$

where E is the elastic modulus, a_Ψ is the lattice parameter and ν (0.3) is the Poisson's ratio. The elastic modulus E was determined by nanoindentation test. A nano hardness tester (CSM) with a Berkovich indenter was used to evaluate the elastic modulus using Oliver and Pharr method. The applied load for all of the elastic modulus measurements was 10 mN. The lattice parameter a_Ψ can be calculated for each diffraction peak where Ψ is the angle between the diffraction vector of planes (hkl) and the normal to the surface, such that $\Psi = \theta - \gamma$ where θ is the Bragg angle and γ is the angle of incidence of the X-ray beam relative to the specimen surface [8].

3.3.1.3 Determination of superlattice period

The BB (θ-θ) geometry was used with an angular step size of 0.03° between 2θ values of 2° and 10° for determining the superlattice period. The superlattice period (Λ) in the low angle region was calculated directly from the standard Bragg equation (Eq. 3.8) [8]:

$$\Lambda = \frac{n\lambda}{2\sin\theta} \tag{3.8}$$

Where θ is the Bragg angle, λ is wavelength of incident ray and n is the order of reflection.

3.3.2 Determination of adhesion strength of thin films

3.3.2.1 Scratch test

Scratch test was carried out to examine the adhesion strength of the coatings. An automatic scratch tester developed by CSM instruments, which enables the measurement of the mechanical strength - adhesion and intrinsic cohesion of hard and brittle coatings on softer and tougher substrates was used to test the coatings. This instrument is equipped with an optical microscope to choose the desired area and analyse the scratch track after the test. A Rockwell C diamond indenter (120° cone shaped indenter of 200 μm radius) was allowed to slide on the sample with a static load of 5 N and the force was increased gradually up to a value of 100 N while moving the

sample forward. Subsequently the optical microscope was used to determine the critical load Lc, the minimum load at which a well-defined failure occurs.

3.3.2.2 Rockwell - C indentation method

A Rockwell hardness tester with a C type diamond indenter (120° cone shaped indenter) was indented into the deposited coating with an applied force of 1471 N. The force was achieved with a mass of 150 kg. The indentation made through the coating by the indenter was observed through an optical microscope. The adhesive strength is categorised according to the six grades (Fig. 3.12) of indentations, such as. HF 1 - HF 4 (acceptable) and HF 5 - HF 6 (unacceptable) outlined by the Association of German Engineers Guideline - 3198 [9]. The grades are dependent on the degree of cracking and/or spallation of the coating around the indentation.

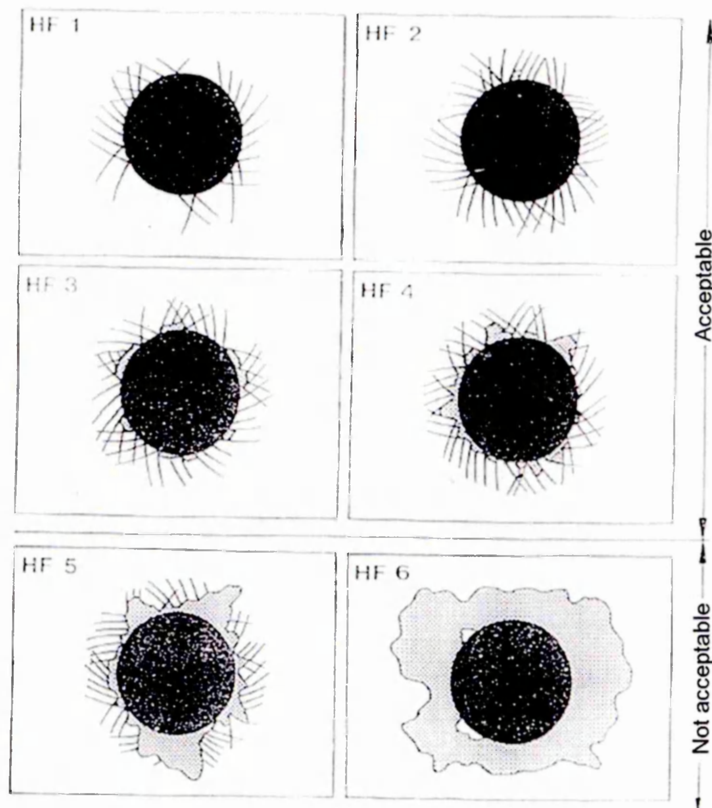

Figure 3.12 Six grades of indentations outlined by the Association of German Engineers Guideline - 3198 [Ref.9]

3.3.3 Nanohardness measurement

The hardness and Young's modulus of the deposited coatings were measured in a CSM nano indentation tester using Oliver-Pharr method [10-11]. The measurements were carried out using a Berkovich indenter which made indentations into the sample (normal to the sample surface) at a load of 10 mN. The indentation depth was less than $1/10^{th}$ of the coating thickness in order to avoid the influence of substrate on the hardness measurements. Then the load was gradually removed until partial or complete relaxation of the material occurs.

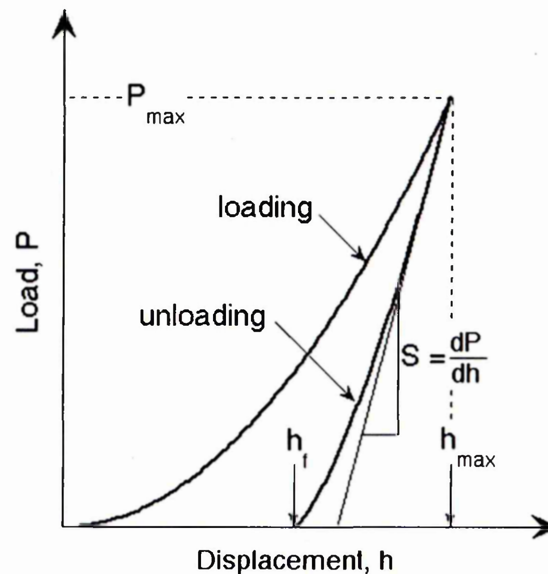

Figure 3.13 Schematic representation of indentation load - displacement data showing important measured parameters [Ref. 10]

According to Oliver-Pharr method, hardness and Young's modulus are determined from the resultant load - displacement data (Fig. 3.13) obtained during one cycle of loading and unloading. Fig. 3.14 illustrates the unloading process showing parameters characterizing the contact geometry.

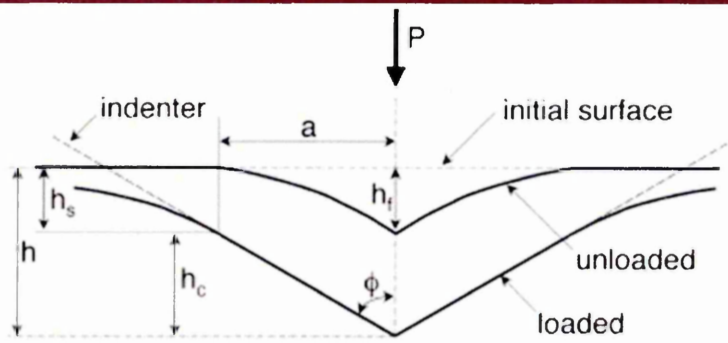

Figure 3.14 Schematic illustration of the unloading process showing parameters characterizing the contact geometry [Ref. 10]

The hardness (H) is estimated from:

$$H = \frac{P_{max}}{A} \quad (3.9)$$

where P_{max} is the maximum load obtained from the P-h curves and A is the contact area.

The contact area A is

$$A = F(h_c) \quad (3.10)$$

Where F is an "area function" that describes the projected (or cross sectional) area of the indenter at a distance d back from its tip and h_c is the depth along which contact is made between the indenter and the specimen.

The h_c is written as

$$h_c = h_{max} - h_s \quad (3.11)$$

Where h_{max} is the maximum displacement and h_s is the amount of sink-in. The amount of sink-in is given by

$$h_s = \varepsilon \frac{P_{max}}{S} \quad (3.12)$$

Where ε is a constant that depends on the geometry of the indenter, P_{max} is the maximum load and S is the elastic unloading stiffness (contact stiffness). The S is defined as the slope of the upper portion of the unloading curves during the initial stages of unloading [10-11].

The elastic modulus is calculated from the relationship

$$S = \beta \frac{2}{\sqrt{\pi}} E_{eff} \sqrt{A} \tag{3.13}$$

Where S is the contact stiffness, A is the contact area, β is the correction factor that depends on the geometry of the indenter and E_{eff} is the effective elastic modulus defined by

$$\frac{1}{E_{eff}} = \frac{1-v^2}{E} + \frac{1-v_i^2}{E_i} \tag{3.14}$$

Where E and v is the Young's modulus and Poisson's ratio of the specimen and E_i and v_i is the Young's modulus and Poisson's ratio of the indenter [11].

3.3.4 Tribological characterisation

The pin on disc method was used to determine the coefficient of friction (μ) and wear coefficient (K_c) of the coatings. A computer controlled CSM room temperature pin on disc tribometer was used for the measurements. In this tribometer, the sample holder rotates and the counterpart remains stationary. The sample was fixed onto a rotating sample holder. The counterpart, 6mm diameter of alumina (Al_2O_3) ball was supported by an arm. The system calibration includes the calibration of friction force and the motor calibration. The calibration of friction force was carried out by measuring the same using a load cell with 0 and 5 N loads. The load was applied by placing a weight on the arm that supports the counterpart. The applied load was 5 N, the radius of the wear track was 10 mm and the linear speed of the sample relative to the counterpart was 10 cm/s for the measurements. The coefficient of friction is plotted against time, number of revolutions and the distance travelled using a software programme by which the tribometer is controlled.

3.3.4.1 Coefficient of friction measurement

Friction is defined as the resistance to relative motion of contacting bodies. The degree of friction is expressed as a coefficient of friction (μ). Coefficient of friction (μ) is given as

$$\mu = \frac{F_T}{F_N} \quad (3.15)$$

where F_T is the tangential force required to initiate or sustain relative motion and F_N is the normal force that presses the two surfaces together. The coefficient of friction depends on various factors, such as intrinsic properties of the materials involved, operating conditions, sliding speed, load and lubricant [12].

3.3.4.2 Wear coefficient measurement

Wear is defined as a process of unwanted material removal from one or both of two solid surfaces which are in sliding or rolling motion relative to each other [12]. Generally, a wear coefficient expresses the resistance to contact wear [13]. According to the well-known Archard equation, the adhesive wear (W) is

$$W = \frac{V}{L} = K\frac{F_N}{H} \quad (3.16)$$

where V is the wear volume, L is the sliding distance, K is the dimensionless wear coefficient, F_N is the normal load and H is the hardness of the softer material. This equation shows hardness is the only material property that affects the wear coefficient. But it was shown that the K depends on various properties of the materials in motion [12].

In this study, the wear coefficient (K_c) was determined using Eq. 3.15 based on the assumption that the wear volume varies directly with the contact load and the sliding distance (Eq. 3.17).

$$V = K\,L\,F_N \quad (3.17)$$

$$K_c = \frac{V}{LF_N} \quad (3.18)$$

where V is the wear volume, L is the sliding distance, K_c is the dimensional wear coefficient (usually expressed in mm^3/Nm) and F_N is the normal load [13].

The wear volume can be expressed as:

$$V = 2\pi RA \tag{3.19}$$

where V is the wear volume, R is the radius of wear track and A is the cross sectional area of the wear track. The cross sectional area A was measured using a Vecco Dektak surface profiler [14].

3.3.5 Determination of surface roughness

Surface texture is referred to the unique characteristics of a surface. The surface roughness is one of the measurable quantities from which the quality of a surface can be identified. It is defined as closely spaced, irregular deviations of the actual topography of a surface from its ideal form and expressed in terms of its height, width and distance along the surface. Generally, surface roughness can be expressed by two methods such as arithmetic mean value (R_a) and root-mean-square roughness (R_q) according to the equations [15]:

$$R_a = \frac{a+b+C+d+\cdots}{n} \tag{3.20}$$

$$R_q = \sqrt{\frac{a^2+b^2+c^2+d^2+\cdots}{n}} \tag{3.21}$$

where all ordinates, a, b, c..., are absolute values and n is the number of readings.

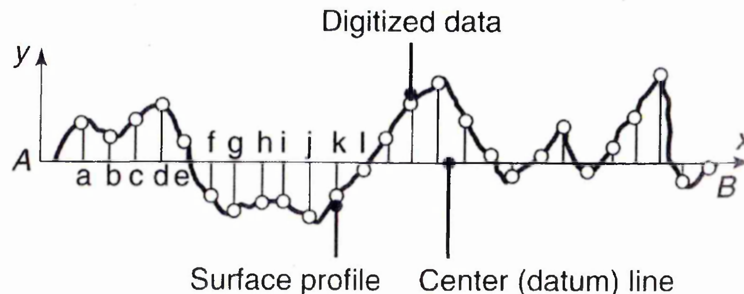

Figure 3.15 Coordinates used for surface roughness measurement [Ref.15].

The surface roughness measurements were carried out by a Veeco Dektak surface profilometer. A diamond stylus was driven along a straight line over the surface

to record the profilometer traces on an amplified vertical scale (larger than the horizontal scale) [15].

3.3.6 Energy Dispersive X- ray spectroscopy

The stoichiometry of the coatings was studied using Energy Dispersive X - ray (EDX) spectroscopy. An EDX module attached to a scanning electronic microscope (FEI NOVA - NanoSEM 200) was used for the analysis. The applied energy was 20 kV. A schematic of energy dispersive X-ray spectrometer is shown in Fig. 3.16. It is well known that the X-rays are produced whenever atoms of the target materials interact with high-speed electrons. The energy of the X-rays is characteristic of the atoms which emitted them. In EDX spectra, energy against X-ray intensity is plotted by observing the X-rays using a solid-state detector and an analyser. The elements present in the sample can be identified by this spectrum. Typically, the quantitative analysis of the elements present in the thin film sample is done by converting the measured characteristic X-ray intensities into the weight fractions using the equation

$$\frac{C_A}{C_B} = k_{AB}\frac{I_A}{I_B} \quad (3.22)$$

where C_A and I_A is the weight fraction and the characteristic X-ray intensity of element A, C_B and I_B is the weight fraction and the characteristic X-ray intensity of element B and k is a constant at a given operating voltage [16].

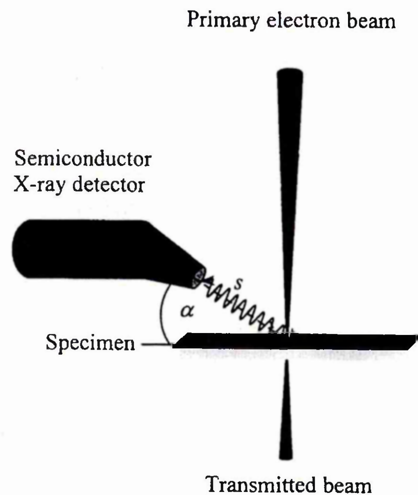

Figure 3.16 Schematic of the Energy Dispersive X-ray spectrometer [Ref.17]

3.3.7 Microstructural analysis

Microstructural analysis was done using a scanning electron microscope (FEI NOVA - NanoSEM 200) and a transmission electron microscope (TEM, Philips CM430).

3.3.7.1 Scanning electron microscopy

A typical Scanning Electron Microscope (SEM) is composed of the microscope column, the various signal detector systems, the computer hardware and software used to process the collected data, and a display and recording systems. Schematic of a SEM is shown in Fig. 3.17. The microscope is attached to a separate vacuum pumping and degassing system. Because a vacuum is mandatory to avoid scattering of high energy electrons by residual gas in the microscope column, to maintain the electron gun thermally and chemically stable during the microscope operation and to minimize or eliminate contamination of the sample due to electron beam interaction during observation. The components of the microscope column include an electron gun, condenser lens, scanning coils and probe lens. A variety of electron sources such as tungsten hair-pin filament, lanthanum hexaboride (LaB_6) tip, cerium hexaboride (CeB_6) and tungsten field emission tip are used. The high energy electrons from the electron gun are focused onto the specimen surface through a probe lens which determines the ultimate resolution achievable in the microscope. The electromagnetic scanning coils placed above the probe lens facilitate the electron beam to be scanned across the specimen surface in an x-y raster. A variety of signal detectors for measuring such as high energy (backscattered) electrons, low energy (secondary) electrons, excited (characteristic) X-rays, etc. are equipped with the microscope. The intensities of various signals generated by interactions between the beam of electrons and the solid specimen (Fig. 3.18) are measured using the detectors and stored in the computer. The stored values are then mapped as variations in brightness on the image display [18].

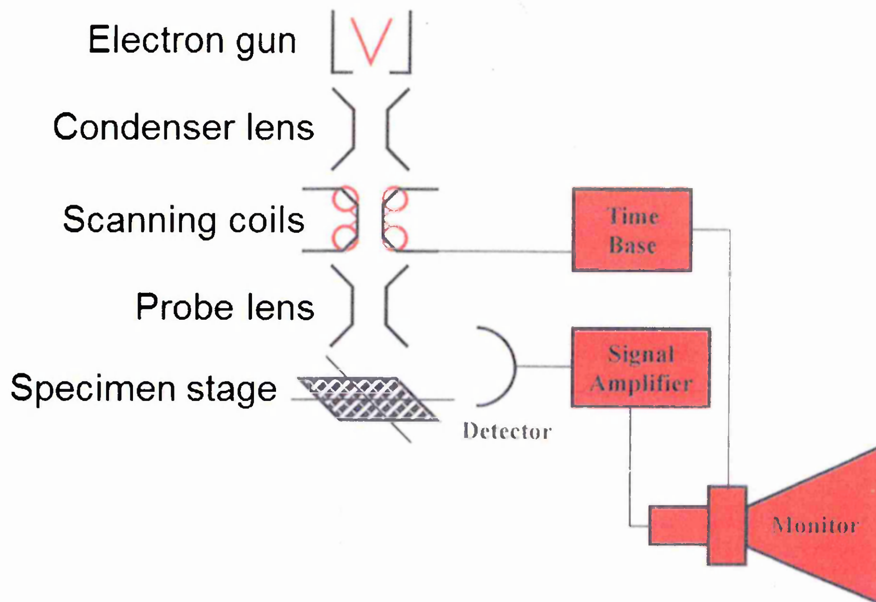

Figure 3.17 Schematic of a SEM [after Ref.18]

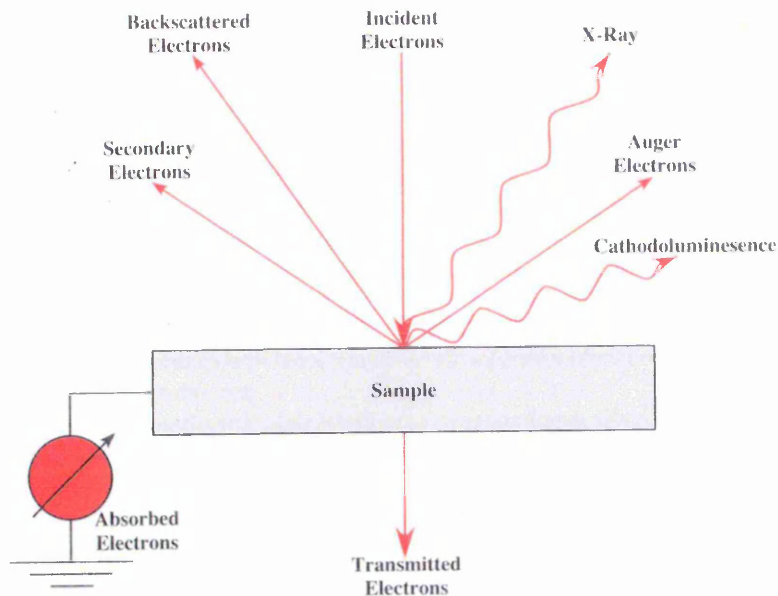

Figure 3.18 Schematic of various signals generated due to the interactions between the beam of electrons and the solid specimen, which can be useful in characterising the microstructure [Ref.18]

3.3.7.2 Transmission electron microscopy

Fig. 3.19 illustrates a Transmission Electron Microscope (TEM). In TEM, the high energy electrons from an electron source (Sec. 3.3.7.1) are focused onto the specimen surface through electromagnetic condenser lens by controlling the lens

currents. The specimen can be moved in x, y and z direction and can be tilted about x and y axes at right angles in the plane of the specimen. The standard TEM specimen diameter is about 3 mm and the thickness is less than 0.1 μm in order to transmit most of the high energy electrons through the specimen without suffering significant energy loss. Focusing of the first image from the elastically scattered electrons that have been transmitted through the thin film specimen is achieved by changing the lens current of the electromagnetic lens in order to adjust the focal length of the electromagnetic lens. Then the final imaging was done by the final imaging system that also consists of electromagnetic lenses. Finally, a fluorescent screen is used to convert the high energy electron image into an image that is visible to the naked eye. The final image has been recorded using photographic emulsions and digitally by charge coupled devices combined with computerized image processing [18].

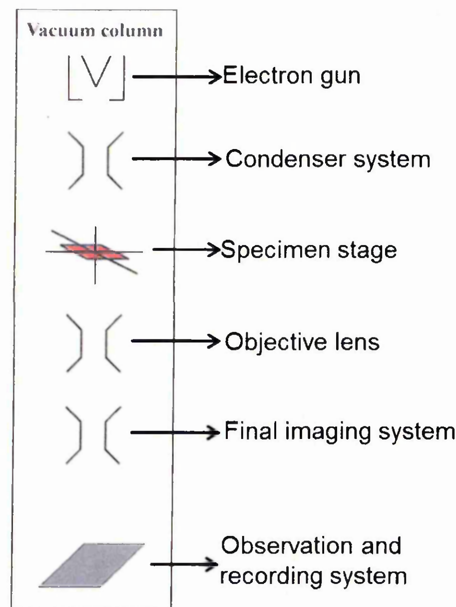

Figure 3.19 Schematic of a TEM [Ref.18]

3.3.7.2.1 TEM specimen preparation

The cross-section TEM specimen preparation for examination in the microscope involves slicing, mechanical grinding, polishing and ion beam milling. The specimens were sliced into small rectangular pieces (length ~ 3 mm and breadth ~ 1 mm) using a

SiC abrasive wheel in a cut-off machine. Two rectangular pieces were glued together with the coating sides facing each other (Fig. 3.20) onto a glass plate using the crystalline wax. The slices were ground on both sides by hand using 600, 1200 and 4000 grit abrasive papers to about 50 - 60 μm of thickness followed by hand polishing on both sides using 3, 1 and 0.5 μm diamond lapping. After polishing, the specimen was removed from the glass plate by melting the wax and subsequently cleaned using acetone. The specimen is fixed onto a copper gird holder using a fast-curing epoxy (resin + hardener). Finally, it was subjected to ion milling in a precision ion polishing system (Model 691, Gatan) for obtaining electron transparent regions. Typical conditions used for the ion milling were: gun angles: ±7°, rotation speed: 3 rpm and voltage: 5 kV initially and final polishing at 4° and 3 kV for 10 minutes. The polishing was single sided from substrate side until a small hole formed on the coating side of the specimen [19].

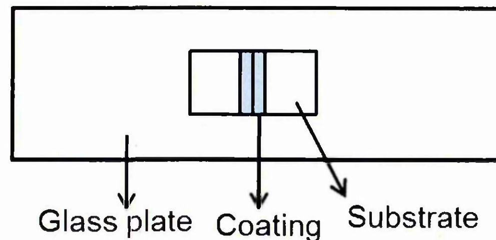

Figure 3.20 Schematic showing the cross-section TEM sample mounted on a glass plate

3.3.8 Electrochemical corrosion testing

Corrosion refers to the material loss by the dissolution of metal by its reaction with the environment. Corrosion destroys the metals by converting them into oxides or other corrosion products. Typically, corrosion is a combination of two electrochemical half-cell reactions such as oxidation and reduction. For example, a hypothetical metal M that has n valence electrons in corrosive medium oxidizes (Eq. 3.23) at anode and any metal ions present in the solution are reduced (Eq. 3.24) at cathode by transferring of electrons from each metal atom that is oxidized according to the reactions [4, 20]:

$$M \rightarrow M^{n+} + ne^- \quad (3.23)$$

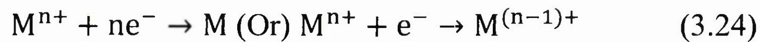

$$M^{n+} + ne^- \rightarrow M \text{ (Or) } M^{n+} + e^- \rightarrow M^{(n-1)+} \quad (3.24)$$

The oxidation reaction in the corrosion process is mainly due to anodic currents. When a specimen is immersed in a corrosive solution and the specimen is not connected to any instrumentation, a potential relative to a reference electrode is generated due to the electro chemical reactions (corrosion) at the specimen-solution interface. This potential is termed as the corrosion potential (E_{Corr}) or the open circuit potential at which the rate of oxidation is exactly equal to the rate of reduction. Hence, at E_{CORR} (the specimen is at equilibrium with the environment), both the anodic and cathodic currents present on the specimen surface are exactly equal in magnitude and the net current is equal to zero. The corrosion potential is a characteristic of the specific specimen-solution system since it is determined by the specific chemistry of the system. And this potential can't be directly measured as any potential measuring device measures a potential energy difference. Therefore, it can be compared to the potential of a known reference system and can be measured indirectly. The corrosion current (i_{Corr}) is directly related to the corrosion rate. The i_{Corr} can be measured by polarizing the specimen in a systematic manner using the proper instrumentation. Polarization accelerates the oxidation or reduction reactions at the specimen [21-22].

In this study, the potentiodynamic polarization technique was used to study the corrosion performance of the coatings. It involves the measurement of polarization characteristics by plotting current response (i) against applied potential (E). The coatings deposited on SS substrates were immersed under 3.5 % NaCl solution in a corrosion test cell (Fig. 3.21) and aerated for 20 minutes. They were also cathodically cleaned for 100s prior to polarisation. A computer controlled potentiostat (Model: EG&G 263A, Princeton Applied Research) was used for the measurements. The potentials were recorded with respect to a saturated Ag/AgCl electrode. The test

specimens were masked with bees wax to expose a surface area of 1 cm^2. The sweeping potential was varied from - 1000 mV to +1000 mV with the scan rate of 1 mV/s. The potentiostat operation is illustrated in Fig. 3.22.

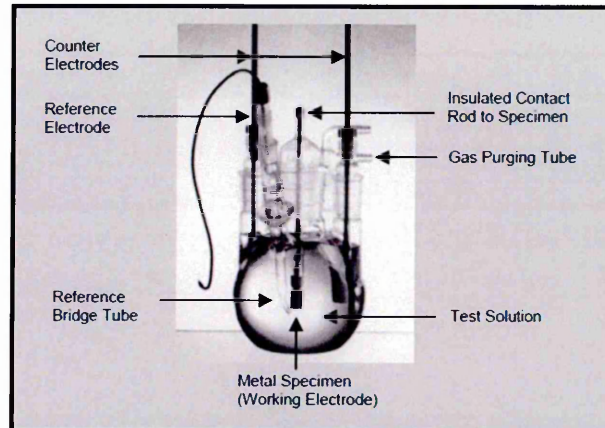

Figure 3.21 Typical electrochemical corrosion test cell [Ref.21]

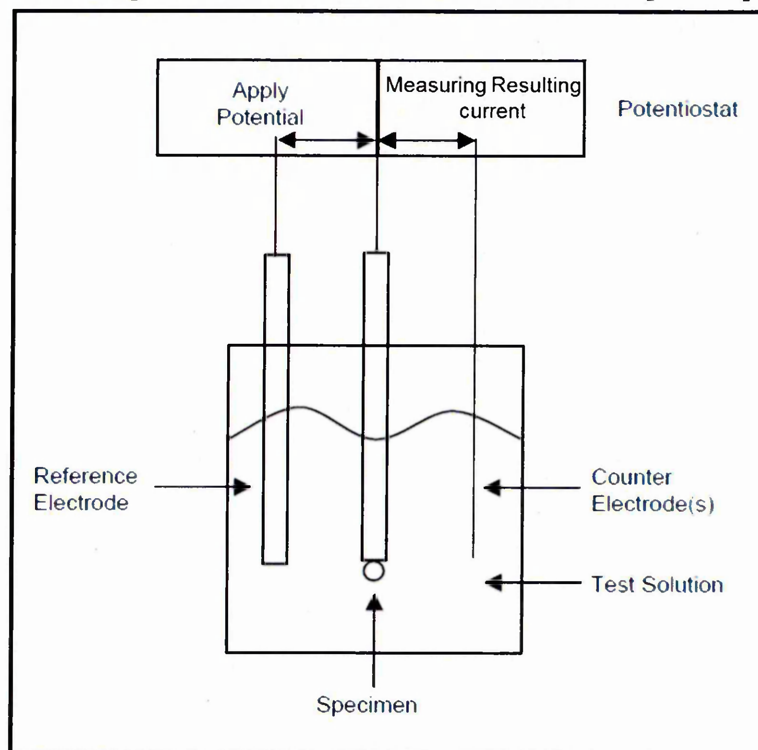

Figure 3.22 Schematic representation of potentiostat operation [Ref.22]

3.3.9 Raman spectroscopy

Raman spectroscopy was used to study the effect of corrosion on the coating surface since it is very sensitive in detecting the surface oxide formation. This technique is based on the 'Raman Scattering' which is defined as the inelastic scattering of a beam

of light (photons) passed through a transparent substance. As a result of the inelastic collision between the incident photon and the molecule the vibrational or rotational energy of the molecule is changed by an amount ΔE_m. Hence the energy of the scattered photon ($h\nu_s$) is different from the energy of the incident photon ($h\nu_i$) by an amount equal to ΔE_m [23]:

$$h\nu_i - h\nu_s = \Delta E_m \quad (3.25)$$

In Raman scattering, a molecule in the ground vibrational state (v = 0) absorbs the energy while interacting with the incident photon and it is raised momentarily to an unstable high energy level (dashed line). Then, ΔEm is positive and the molecule immediately returns to the v = 1 energy level by losing the energy and emitting a scattered photon with the energy lower than that of the incident photon energy ($h\nu_s < h\nu_i$). This scattered photon is attributed to a Stokes line in the Raman spectrum. The second possibility is that the molecule which is initially in the excited state (v = 1) absorbs the energy while interacting with the incident photon and it is also raised momentarily to an unstable high energy level (dashed line). In this case, ΔEm is negative and the molecule immediately returns to the ground vibrational level (v = 0) by losing the energy and emitting a scattered photon with the energy higher than that of the incident photon energy ($h\nu_s > h\nu_i$). This scattered photon is attributed to an anti-Stokes line in the Raman spectrum [23]. Fig. 3.23 shows schematic of the inelastic Raman Scattering.

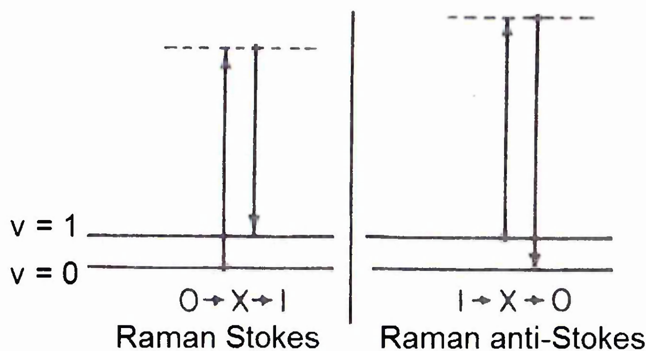

Figure 3.23 Schematic illustration of Raman scattering [Ref.23]

In a Raman microscopic system (Fig. 3.24), a beam of laser is allowed through a filter to obtain a monochromatic wave length beam. The monochromatic laser beam is then focused onto the sample surface by a microscope. The scattered Raman signals reflected from a microscopic area of the sample is again collected by the microscope and sent through a diffraction grating system before recorded by a detector [24].

In this study, Raman spectra of as-deposited and corroded samples were recorded using a Horiba Jobin Yvon (HR 800) Raman micro-spectroscope. The sample was irradiated with a green laser of 520 nm wavelength in order to excite the molecules in the region of interest. A 10 % transmission filter was utilized to limit the intensity of the laser. The exposure time of the sample to the laser was approximately 5 S. The spectra were acquired in the range between 100 cm^{-1} and 1500 cm^{-1}.

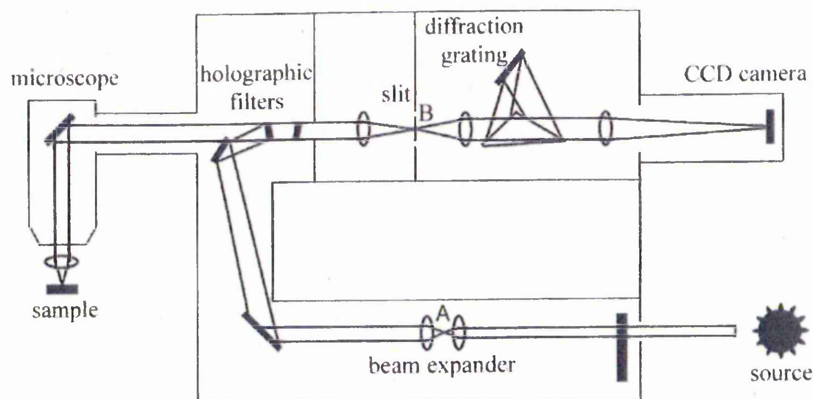

Figure 3.24 Schematic optical diagram of a Raman microscope [Ref.24]

References

1. PALMER, Christopher (2005). *Diffraction grating - handbook.* Sixth ed., New York, United States of America, Newport Corporation.
2. NIST atomic spectra database. (2013). [online]. at: http://www.nist.gov/pml/data/asd.cfm.
3. LOFTHUS, Alf and KRUPENIE, Paul H. (1977). The spectrum of molecular nitrogen. *Journal of physical and chemical reference data,* **6** (1), 113-307.
4. CALLISTER, William D. and RETHWISCH, David G. (2011). *Materials science and engineering.* Eighth ed., Asia, Wiley.
5. Cullity, B.D. and Stock, S.R. (2001). *Elements of X-ray diffraction.* First ed., New Jersey, Prentice-Hall, Inc.
6. Philips Xpert Pro XRD machine - User guide.
7. RICKERBY, D. S., JONES, A. M. and BELLAMY, B. A. (1989). X-ray diffraction studies of physically vapour-deposited coatings. *Surface and coatings technology,* **37** (1), 111-137.
8. LEWIS, D. B., et al. (1999). The influence of the yttrium content on the structure and properties of $Ti_{1-x-y-z}Al_xCr_yY_zN$ PVD hard coatings. *Surface and coatings technology,* **114** (2–3), 187-199.
9. VDI - Association of German Engineers Guideline. (3198).
10. OLIVER, W. C. and PHARR, G. M. (1992). An improved technique for determining hardness and elastic modulus using load and displacement sensing indentation experiments. *Journal of materials research,* **7** (6), 1564-1583.
11. OLIVER, W. C. and PHARR, G. M. (2004). Measurement of hardness and elastic modulus by instrumented indentation. *Journal of materials research,* **19** (1), 3-20.

12. BHUSHAN, Bharat and GUPTA, B. K. (1991). *Handbook of tribology: materials, coatings and surface treatments.* United States of America, McGraw-Hill, Inc.

13. KENNEDY, D. M. and HASHMI, M. S. J. (1998). Methods of wear testing for advanced surface coatings and bulk materials. *Journal of materials processing technology,* **77** (1–3), 246-253.

14. EHIASARIAN, A. P. (2002). *Development of PVD coating processes informed by plasma diagnostics.* PhD Thesis. Sheffield Hallam University.

15. KALPAKJIAN, Serope and SCHMID, Steven (2006). *Manufacturing engineering and technology.* Fifth ed., Singapore, Prentice Hall.

16. HORITA, Zenji, SANO, Takeshi and NEMOTO, Minoru (1987). Simplification of X-ray absorption correction in thin-sample quantitative microanalysis. *Ultramicroscopy,* **21** (3), 271-276.

17. FRIEDBACHER, Gernot and BUBERT, Henning (eds.) (2011). *Surface and thin film analysis: A compendium of principles, instrumentation and applications.* Second ed., Germany, Wiley-VCH Verlag & Co.

18. RANDON, David and KAPLAN, Wayne D. (2008). *Microstructural characterisation of materials.* Second ed., United Kingdom, John Wiley & Sons, Ltd.

19. SRIDHARA RAO, D. V., MURALEEDHARAN, K. and HUMPHREYS, C. J. (2010). TEM specimen preparation techniques. *Microscopy: Science, technology, applications and education,* **2,** 1232-1244.

20. MCCAFFERTY, E. (2010). *Introduction to corrosion science.* United States of America, Springer.

21. *Basics of corrosion measurements.* United States of America, Princeton Applied Research. Application note CORR-1.

22. *Electrochemistry and corrosion: Overview and techniques.* United States of America, Princeton Applied Research. Application note CORR-4.

23. COLTHUP, Norman B., DALY, Lawrence H. and WIBERLEY, Stephen E. (1990). *Introduction to infrared and Raman spectroscopy.* Third ed., United States of America, Academic Press Inc.

24. LENG, Yang (2008). *Materials characterisation: Introduction to microscopic and spectroscopic methods.* Singapore, John Wiley & Sons (Asia) Pte Ltd.

Chapter 4

4 Results and Discussion

This chapter begins with the discussion of plasma diagnostics carried out using optical emission spectrometer while sputtering Ti target in Ar + N_2 atmosphere by utilizing various HIPIMS/UBM sources by varying the process parameters such as coil current and N_2 flow. The characteristics of TiN coatings deposited by pure UBM (conventional DCMS), combined HIPIMS/UBM and pure HIPIMS techniques are discussed in detail. The characterisation results include the effect of degree of HIPIMS utilisation on the microstructure, residual stress, texture, mechanical, tribological and corrosion properties of TiN coatings deposited at different bias voltages and coil currents. The coatings deposited utilizing various source combinations are named depending on the number of HIPIMS and UBM targets used, as follows: pure UBM (4 DC sources), 1HIPIMS + 3UBM, 2HIPIMS + 2UBM and pure HIPIMS (2 HIPIMS sources) coatings. TiN/NbN, TiCN/NbCN and CrN/NbN multilayer coatings were deposited on CoCr test buttons along with HSS, SS and Si substrates since our intended application is on total knee replacement joints made of CoCr alloy. The knowledge gained by investigating the TiN (Ar + N_2) plasma and the properties of TiN coatings was used to determine the process parameters for depositing the multilayers. The characteristics of various multilayer coatings such as TiN/NbN, TiCN/NbCN and CrN/NbN are also discussed.

4.1 Plasma analysis using Optical emission spectroscopy

Optical emission spectroscopy was used to study the effect of process parameters such as coil current, nitrogen flow and the degree of HIPIMS on the plasma chemistry prior to the deposition of the coatings. Table 3.7 (Sec.3.2) lists the optical

emission lines considered for the compositional analysis of the plasma generated by different HIPIMS/UBM source combinations with various coil currents and nitrogen flows.

4.1.1 Effect of different HIPIMS/UBM source combinations on $\{Ti^{1+}\}$ and $\{Ti^{0}\}$

To explain in detail about the effect of various HIPIMS/UBM source combinations on $\{Ti^{1+}\}$ and $\{Ti^{0}\}$, processes carried out with four different source combinations at constant coil current, bias voltage and working pressure is considered. The coil current, bias voltage and working pressure were 3 A, 0 V and 0.3 Pa, respectively. Fig. 4.1 shows the weighted emission intensities $\{Ti^{0}\}$ and $\{Ti^{1+}\}$ as a function of source combination.

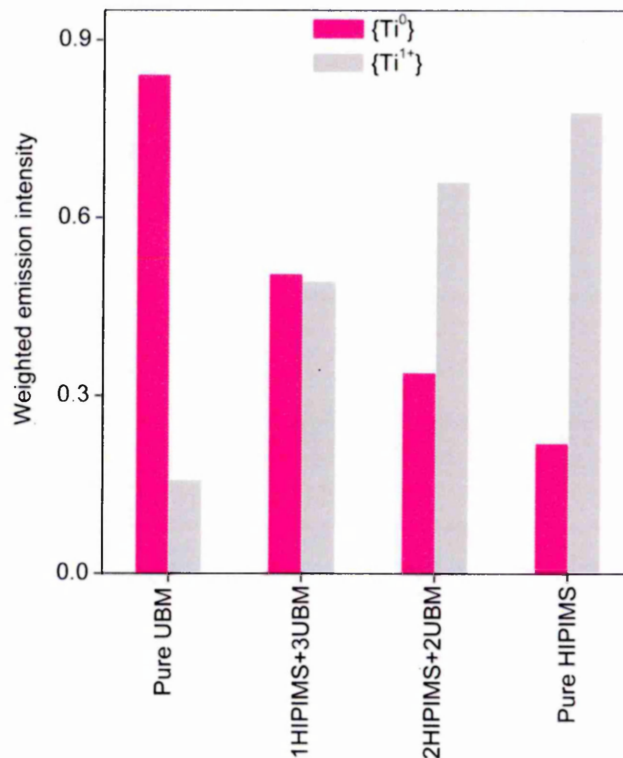

Figure 4.1 Weighted emission intensities as a function of source combination: (a) $\{Ti^{0}\}$; (b) $\{Ti^{1+}\}$

The $\{Ti^{0}\}$ was found to be decreased while $\{Ti^{1+}\}$ increased as more HIPIMS cathodes are energised. The ratio $\{Ti^{1+}\}$:$\{Ti^{0}\}$ started at a low value of 0.19 for the

pure UBM process and increased to 3.54 for the pure HIPIMS process. For 1HIPIMS + 3UBM and 2HIPIMS +2 UBM it was found to be 0.98 and 1.95, respectively. The increase of $\{Ti^{1+}\}:\{Ti^{0}\}$ with increasing HIPIMS utilisation is related to the increased production of Ti^{1+} ions in the high peak power HIPIMS process. The pure HIPIMS process generated a factor of ~ 19 higher metal ionisation ratio than that of the pure UBM process.

4.1.2 Effect of coil current on the degree of metal flux in the plasma generated by utilising different source combinations

Each of the four cathodes is surrounded by an 'unbalancing coil' in the industrial size magnetron sputtering which was used for the deposition. The degree of closed field plasma confinement in the sputtering system was altered by varying the strength of the electromagnetic field of the unbalancing coils by varying the coil current which in turn controlled the degree of ionisation during coating growth. The coil current was varied from 0 to 6 A in 0.5 A increments. The degree of magnetic unbalancing of the magnetron and the closed field confinement increased whilst reducing the width of the race track with increasing coil current. The bias voltage (U_b) and working pressure were kept constant at 0 V and 0.3 Pa, respectively during these measurements.

Fig. 4.2 shows the emission intensities and weighted emission intensities of neutrals Ti^{0} and ions Ti^{1+} generated with different source combinations as a function of coil current. Note that the weighted emission intensity is proportional to the density of species in the plasma and is only a qualitative measure of the density of species as mentioned in Sec. 3.2.

The emission intensity of Ti^{0} for all the source combinations was found to be increased with increasing coil current. The emission intensity of Ti^{1+} considerably increased with increasing coil current for all the source combinations except pure UBM (4 DCMS targets). This increment in emission intensities of Ti^{0} and Ti^{1+} was due to the

enhanced degree of magnetic unbalancing of the magnetron and the closed field confinement.

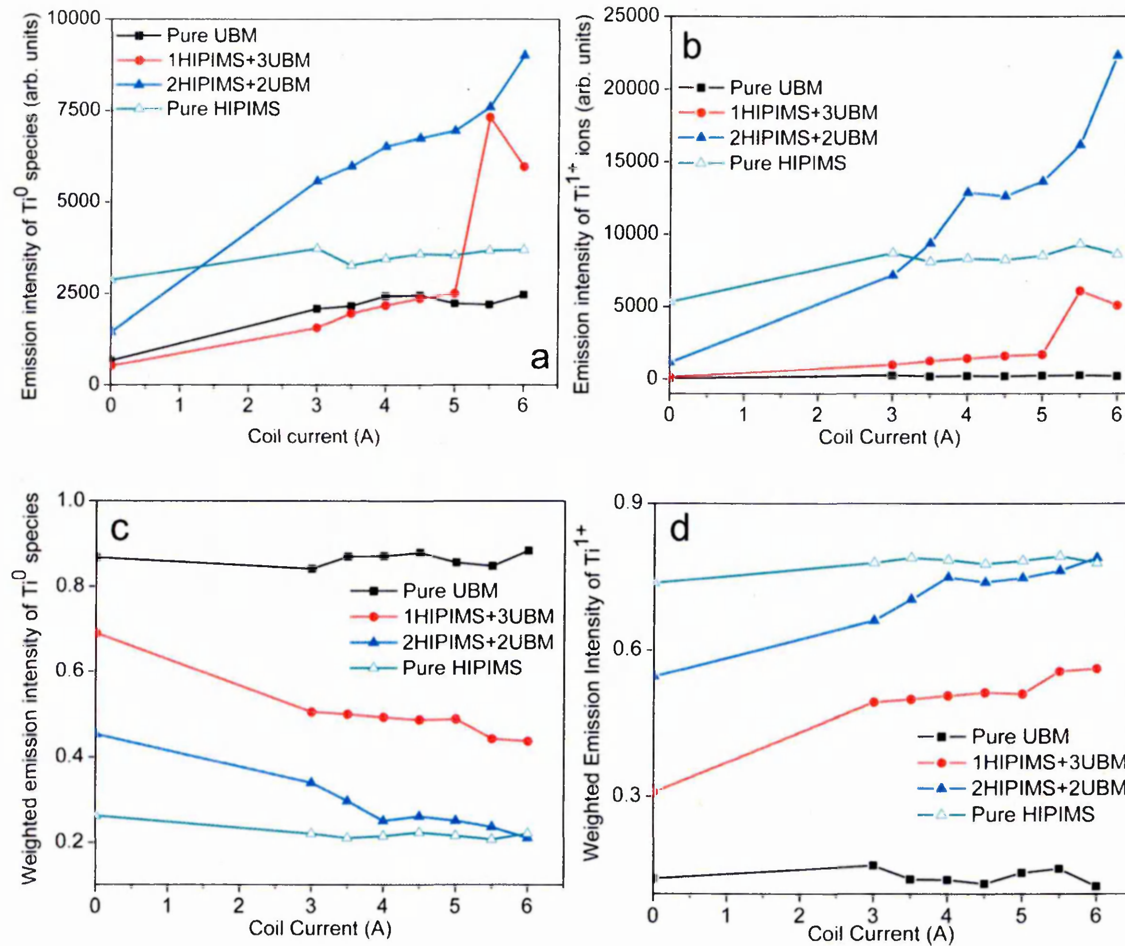

Figure 4.2 Emission intensities as a function of coil current: (a) Ti^0; (b) Ti^{1+} and Weighted emission intensities as a function of coil current (c) Ti^0; (d) Ti^{1+}

In addition, the pure UBM and 1HIPIMS + 3UBM processes exhibited almost an equal amount of emission intensity of Ti^0 followed by pure HIPIMS (2 HIPIMS targets) and 2HIPIMS + 2UBM, respectively. The emission intensity of Ti^0 in the pure HIPIMS process was low as compared to the 2HIPIMS + 2UBM process. This could be attributed to the reduced number of sources (2 HIPIMS) used for the pure HIPIMS process. Similar trend was observed for Ti^{1+} ions.

The weighted emission intensity, $\{Ti^0\}$ was found to be decreased with increasing coil current for all the source combinations except pure UBM. However, the $\{Ti^{1+}\}$ increased with increasing coil current for 1HIPIMS + 3UBM and

2HIPIMS + 2UBM processes. The {Ti^{1+}} was found to be almost constant in the case of pure HIPIMS which is again attributed to due to the reduced number of targets. It was found to be decreased with increasing coil current for the pure UBM sputtering. The decreasing {Ti^0} and increasing {Ti^{1+}} emphasized that the degree of ionisation of metal flux in the chamber increased with increasing coil current. In other words, relatively more metal ions (Ti^{1+}) were generated rather than the metal neutrals (Ti^0) as the coil current increased.

The amount of {Ti^0} in the pure UBM process was found to be the highest followed by 1HIPIMS + 3UBM, 2HIPIMS + 2UBM and pure UBM processes. In contrast the amount of {Ti^{1+}} in the pure UBM was the lowest and it increased with increasing degree of HIPIMS contribution. Despite of using only two HIPIMS targets, the pure HIPIMS process exhibited the highest {Ti^{1+}}.

In summary, for pure UBM, the coil current showed negligible effect on {Ti^{1+}} as fewer Ti^{1+} ions were produced as compared to Ti^0 neutrals. For 1HIPIMS + 3UBM source combination, the ratio {Ti^{1+}}:{Ti^0} increased from 0.45 at 0 A to 1.29 at 6 A. For 2HIPIMS + 2UBM source combination, the {Ti^{1+}}:{Ti^0} ratio was ~ 1.2 at 0 A of coil current and increased to ~ 3.75 at 6 A which is ~ 3 fold increase compared to the ratio at 0 A. For pure HIPIMS source combination, the ratio {Ti^{1+}}:{Ti^0} increased from 2.81 at 0 A to 3.75 at 3.5 A. The change in the ratio for coil currents above 3.5 A was negligible which could be due to reduced number of sources used for this process (2 HIPIMS).

4.1.3 Effect of N_2 flow on the degree of metal flux and N_2^0 in the plasma generated by utilising different source combinations

OES measurements with increasing N_2 flow from 0 to 180 sccm (total pressure from 0.24 Pa to 0.36 Pa) were done to understand the effect of target poisoning. The bias voltage and coil current were kept constant at 0 and 3 A, respectively during these

measurements. Fig. 4.3 shows the emission intensities and weighted emission intensities of Ti^0 neutrals, Ti^{1+} ions and N_2^0 neutrals generated in the plasma with different source combinations as a function of N_2 flow.

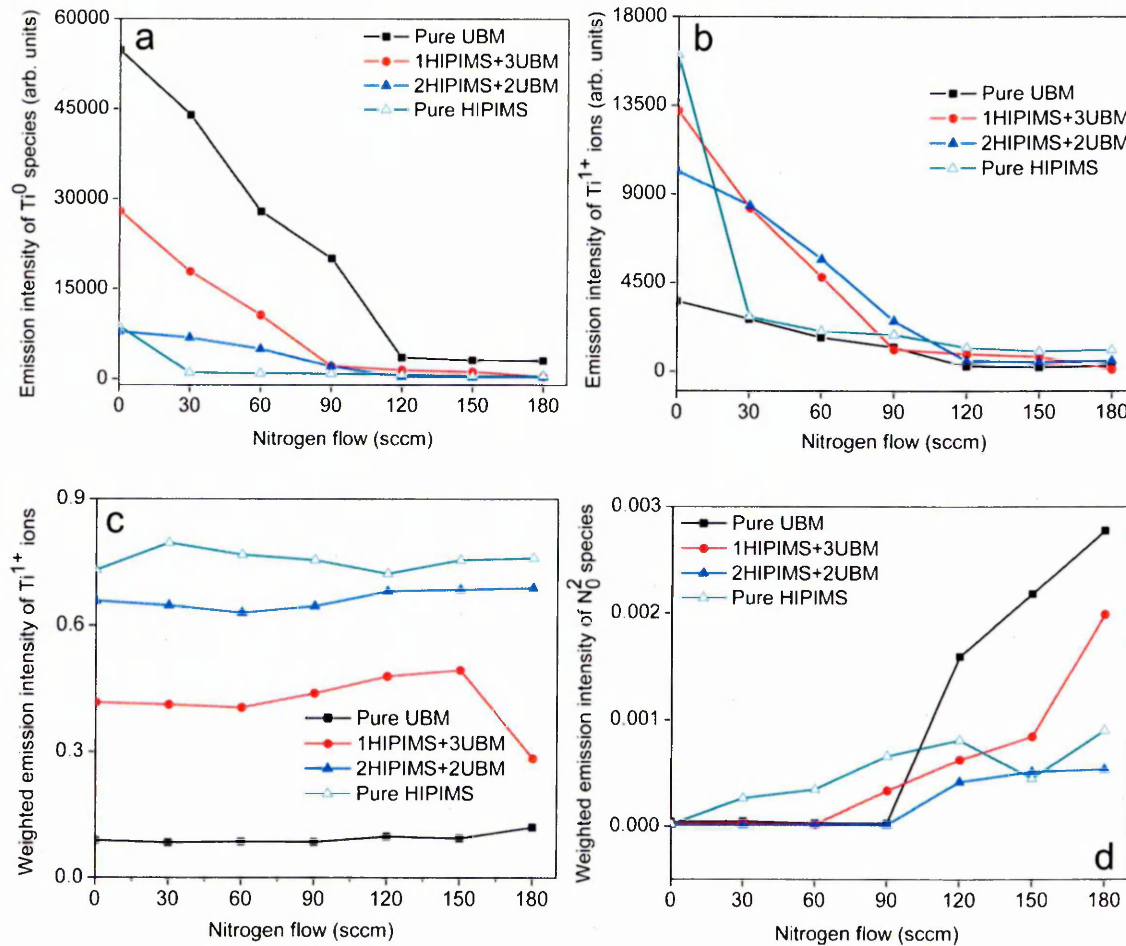

Figure 4.3 Emission and weighted emission intensities as a function of N_2 flow: (a) Ti^0; (b) Ti^{1+}; (c) $\{Ti^{1+}\}$; (d)N_2^0

The trend in Fig. 4.3 (a - b) is very similar to the classical poisoning case observed for magnetron sputtering (reduction of the amount of metallic species with increasing reactive gas flow rate). The emission intensities of Ti^0 and Ti^{1+} for all the source combinations were found to be decreased rapidly with increasing N_2 flow from 0 sccm to 120 sccm which can be attributed to the development of the target poisoning effect. It is well understood that during reactive sputtering a thin layer of TiN is formed due to the chemisorption or physisorption of neutral N_2 molecules on the target and the target bombardment by molecular or atomic nitrogen ions. As a consequence, the

deposition rate of TiN will reduce with increasing the nitrogen flow rate. Ti^0 and Ti^{1+} emission intensities were diminished due to lower sputtering yield of TiN and the involvement of more nitrogen ions in the sputtering process as compared to the non-reactive sputtering case where Ar ions are used [1]. Above 120 sccm of N_2 flow, the target poisoning was complete and the intensities of Ti^0 and Ti^{1+} were constant. The $\{Ti^{1+}\}$ remains almost stable with increasing N_2 flow for all the source combinations except 1HIPIMS + 3UBM coating in both poisoned and sub-stoichiometric regimes due to the constant peak power. The $\{N_2^0\}$ is below the detection limit for N_2 flows up to 90 sccm in pure UBM and 2HIPIMS + 2UBM processes as the nitrogen is completely absorbed while reacting with titanium. For flows between 90 - 120 sccm, the $\{N_2^0\}$ rises sharply, as excess nitrogen is introduced. On the other hand, the $\{N_2^0\}$ was below the detection limit for N_2 flows up to 60 sccm in the case of 1HIPIMS + 3UBM process and it increased monotonically up to 120 sccm in pure HIPIMS process which could be due to the reduced number of targets.

In summary, OES measurements revealed that the implementation of HIPIMS has led to highly activated conditions of deposition, in particular ionisation of Ti. In principle these results show that all the combinations where HIPIMS is involved such as 1HIPIMS + 3UBM, 2HIPIMS + 2UBM and 2HIPIMS provide favourable conditions for depositing films with enhanced ion bombardment. Therefore the optimum combination of sources should be selected accounting also for the effect of HIPIMS utilisation on coating microstructure, compressive stress, mechanical, tribological and corrosion properties.

4.2 Energy dispersive X-ray spectroscopy analysis

EDX analysis was done to study the elemental composition of the TiN coatings though it is generally better suited for detecting elements of high atomic number. EDX spectrum of the coatings grown by combined HIPIMS/UBM and pure HIPIMS

techniques with same process parameters [bias voltage: -50 V, coil current: 3 A and working pressure: 0.3 Pa] along with the coating grown by pure UBM technique [bias voltage: -75 V, coil current: 6 A and working pressure: 0.33 Pa] is shown in Fig. 4.4. The EDX spectrum clearly presents well defined peaks of Ti and N_2. The elemental composition of TiN coatings deposited with different source combinations at different bias voltages and coil currents is shown in Table 4.1. The composition of the coatings was almost similar (near-stoichiometric) within the error of the measurement. However, TiN coatings grown by pure HIPIMS technique were over-stoichiometric with N: Ti ~ 1.5. This could be due to the reduced degree of metal species produced by reduced number of HIPIMS sources (2 sources) used for the pure HIPIMS process and the lower sputtering rate due to HIPIMS.

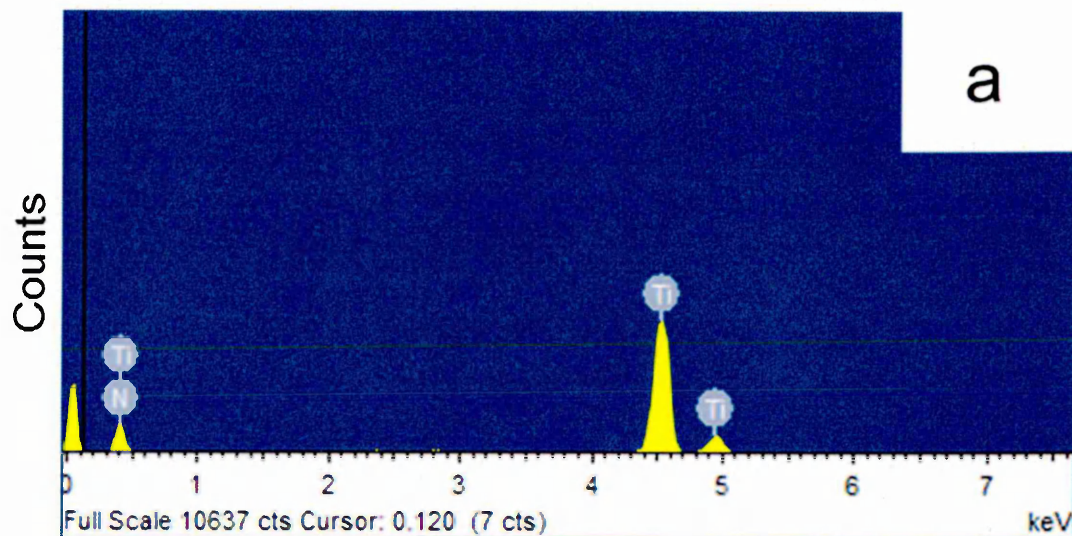

Figure 4.4 EDX spectra of TiN coating (a) pure UBM

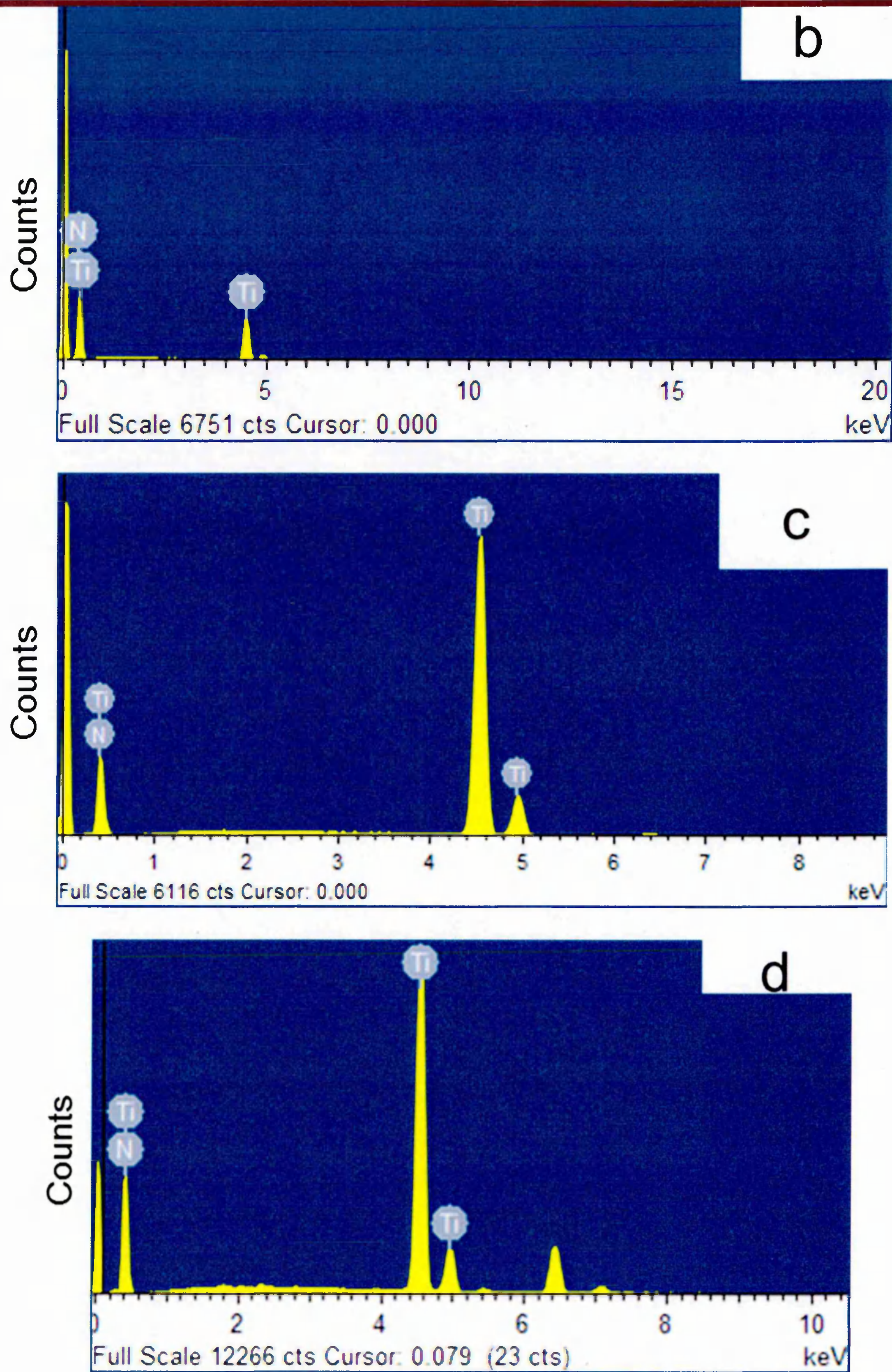

Figure 4.4 EDX spectra of TiN coatings: b) 1HIPIMS + 3UBM; c) 2HIPIMS + 2UBM; d) pure HIPIMS

Table 4.1. Elemental composition of TiN coatings by EDX analysis

Source combination	Bias voltage (V)	Coil current (A)	Working pressure (Pa)	Ti (at. %)	N (at. %)	N/Ti
Pure UBM	-75	6	0.33	~ 49.36	~ 50.64	~1.03
1HIPIMS+3UBM	-50	0	0.22	~ 46.38	~ 53.62	~1.12
	-50	0	0.3	~ 50.49	~ 49.51	~0.98
	-50	3	0.3	~ 49.61	~ 50.39	~1.02
2HIPIMS+2UBM	-50	0	0.3	~ 49.48	~ 50.52	~ 1.02
	-50	0	0.22	~ 49.81	~ 50.19	~ 1.00
	-50	0	0.25	~ 46.69	~ 53.31	~ 1.14
	-50	3	0.3	~ 44.12	~ 55.88	~ 1.27
	-75	6	0.3	~ 47.89	~ 52.11	~ 1.08
Pure HIPIMS	floating potential	0	0.3	~ 40.00	~ 60.00	~ 1.50
	- 50	0	0.3	~ 40.10	~ 59.90	~ 1.49
	-50	0	0.22	~ 40.70	~ 59.30	~ 1.46
	-50	3	0.3	~ 39.42	~ 60.58	~ 1.54
	-75	0	0.3	~ 41.35	~ 58.65	~ 1.41
	-75	6	0.3	~ 42.57	~ 57.43	~ 1.35
	-75	6	0.35	~ 43.08	~ 56.92	~ 1.32

4.3 Effect of HIPIMS utilisation on the deposition rate of TiN coatings

The deposition rate was calculated by measuring the thickness of TiN coatings deposited on silicon substrates. The coated silicon samples were fractured and investigated under a scanning electron microscope. Fig. 4.5 shows the deposition rate of TiN coatings deposited using four different source combinations with increasing degree of HIPIMS utilisation. For completeness, a 4 HIPIMS case derived by extrapolating the results from the 2HIPIMS experiment is also added.

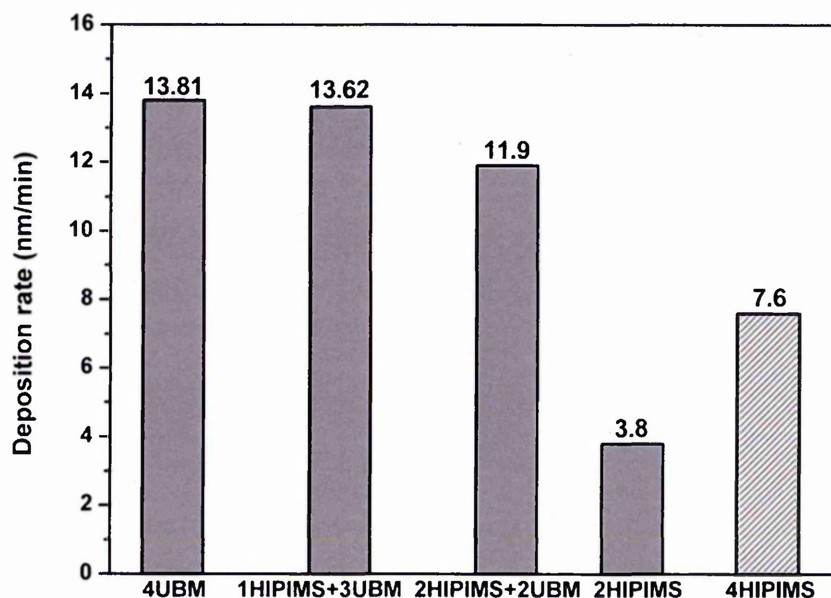

Figure 4.5 Deposition rate as a function of source combinations

As anticipated, the deposition rate was found to be decreased with increasing degree of HIPIMS utilisation. It was relatively high, 13.81 nm/min in the case of pure UBM sputtering with four UBM sources. It decreased to 13.62 nm/min for 1HIPIMS + 3UBM combination. For 2HIPIMS + 2UBM and pure HIPIMS (2 HIPIMS sources) combinations, it was found to be 11.9 and 3.8 nm/min, respectively. The most important reason for the lower deposition rate in HIPIMS is that some of the newly generated metal ions in the sputtered material close to the target are attracted back to the target surface by the cathode potential. The deposition rate for pure HIPIMS process is

expected to increase to 7.6 nm/min when four HIPIMS sources are used for the deposition. The deposition rate loss due to increased HIPIMS utilisation was found to be 1.4% for 1HIPIMS + 3UBM and 13.8% for 2HIPIMS + 2UBM as compared to UBM. For 2HIPIMS, the deposition rate loss was 72.5% and it was 45% for 4HIPIMS (extrapolated value). These experiments clearly demonstrate that combined HIPIMS/UBM processes bear a high potential for improved productivity. Furthermore, if followed, this approach might lead to a reasonable reduction of hardware costs as high quality coatings could be produced with smaller number of HIPIMS sources provided that they deliver the necessary high plasma ionisation.

4.4 Adhesion strength of TiN coatings

The coating-substrate adhesion was evaluated with two different kinds of adhesion measurement techniques such as Rockwell adhesion test and scratch test. An indentation and a scratch were made in each sample. Fig. 4.6 shows the optical images of indentations and scratch tracks (black arrow shows the direction of the moving indentor) of TiN coatings deposited with various source combinations. The adhesive strength of the coatings is categorised using the six grades (Fig. 3.13) of indentations such as HF1 - HF4 (acceptable) and HF5 - HF6 (unacceptable) outlined by the Association of German Engineers Guideline - 3198 [2]. For all the source combinations, no cracks, delamination and spallation of the coatings were observed around the indents (Rockwell) which show the superior adhesion between the coating and the substrate. This superior adhesion strength of all the four coatings can be rated as grade HF1 according to the guidelines outlined by Ref. [2]. Similar behaviour was observed while scratching the coatings by gradually increasing the load up to 100 N. The excellent adhesion behaviour is mainly attributed to the well-defined crystal structure at the coating-substrate interface provided by HIPIMS metal ion etching which promotes the localized epitaxial growth of the coating. However, in all the cases, the substrate was

exposed above 50 N of load. The load at which the substrate was exposed due to scratching is shown in Fig. 4.6. For pure UBM coating, the substrate was exposed around 60 N of load. For 1HIPIMS + 3UBM, 2HIPIMS + 2UBM and pure HIPIMS coatings, the substrate was visible around 70, 80, 70 N of load, respectively. The variations in applied load at which the substrate was exposed can be related to hardness and thickness of the coatings. The scratch test is usually considered as semi-quantitative since it is influenced by many factors including coating thickness, residual stress in the coating, etc.

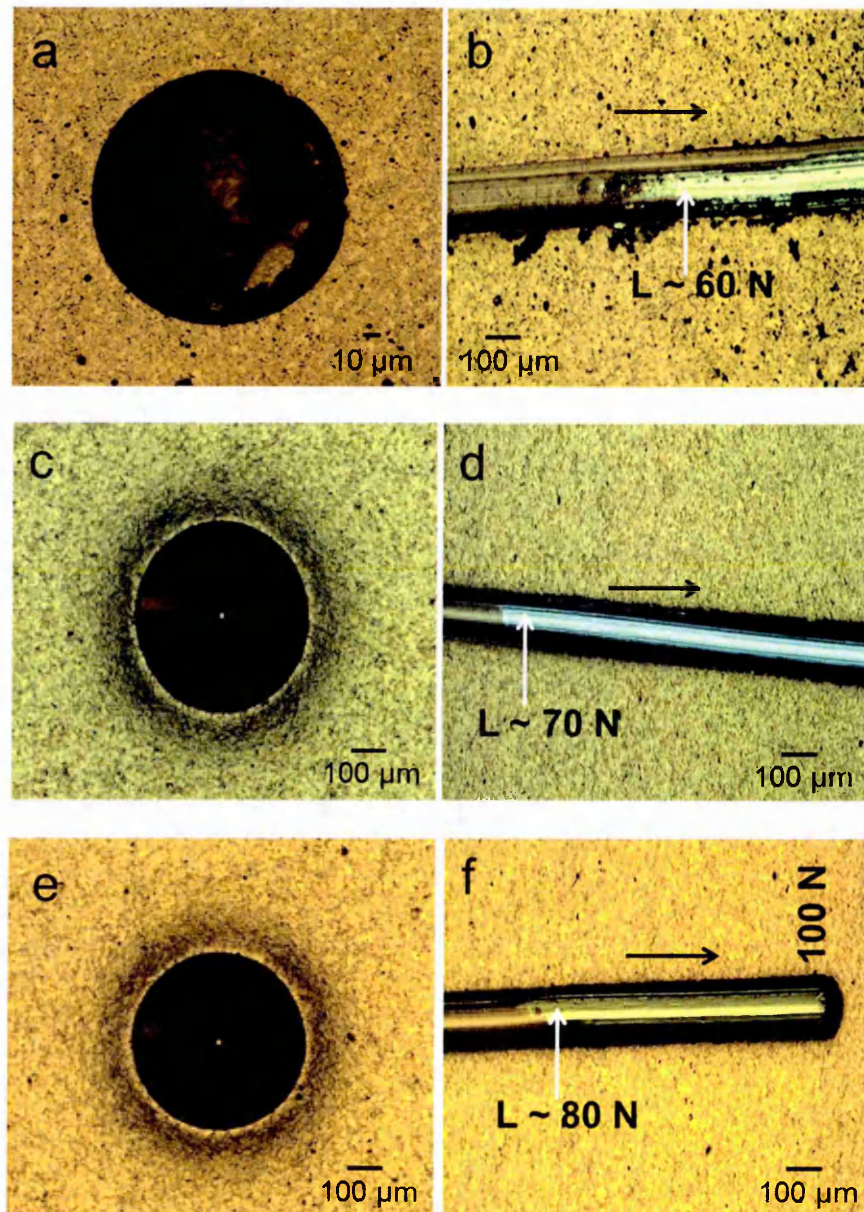

Figure 4.6 Optical images of Rockwell indentations and scratch tracks: (a, b) Pure UBM; (c, d) 1HIPIMS + 3UBM; (e, f) 2HIPIMS + 2UBM

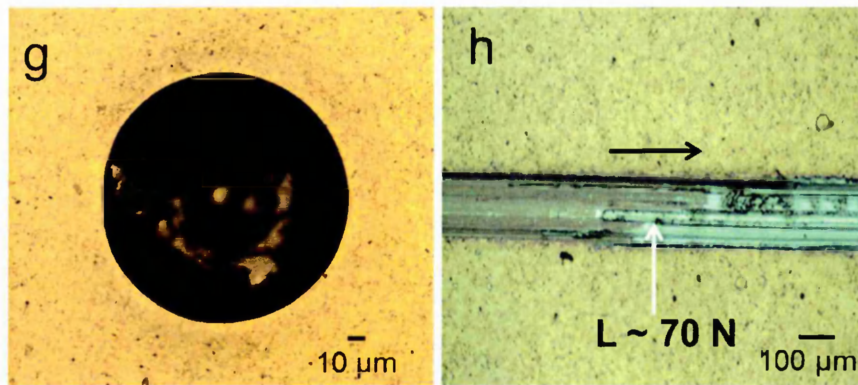

Figure 4.6 Optical images of Rockwell indentation and scratch track: (g, h) 2HIPIMS (Pure HIPIMS)

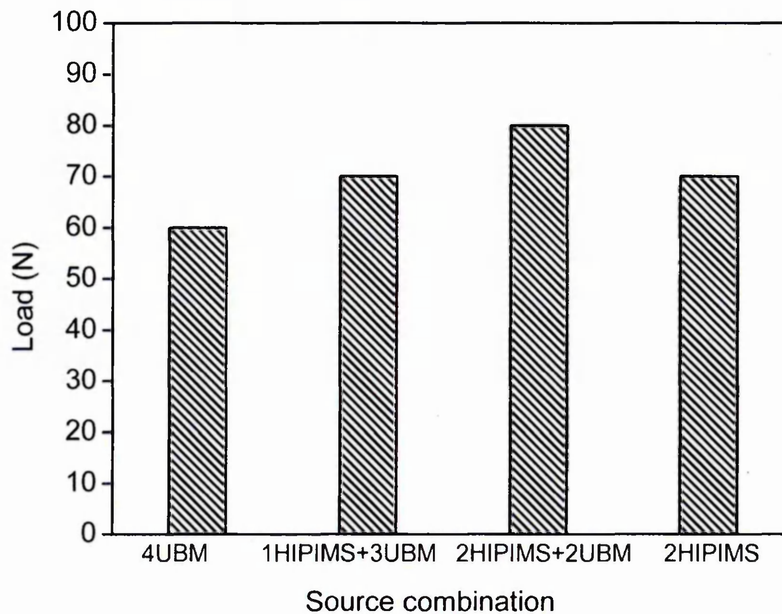

Figure 4.7 The load at which the substrate was visible

4.5 Mechanical and tribological properties of TiN coatings

4.5.1 Nano-hardness test

The nano-hardness and Young's modulus of TiN coatings deposited with various source combinations [bias voltage: -50 V, coil current: 3 A and working pressure: 0.3 Pa] are shown in Fig. 4.8. The applied load for the nanoindentation test was 10 mN. The hardness value of the coating was increased with increasing degree of HIPIMS utilisation. TiN coating grown by 1HIPIMS + 3UBM process is slightly harder than that of the pure UBM grown TiN. The hardness value for

pure UBM and 1HIPIMS + 3UBM grown coatings was 36 GPa and 38 GPa respectively. However, it slightly decreased to 36 GPa for 2HIPIMS + 2UBM grown coating. The pure HIPIMS grown coating showed the highest hardness of 44 GPa.

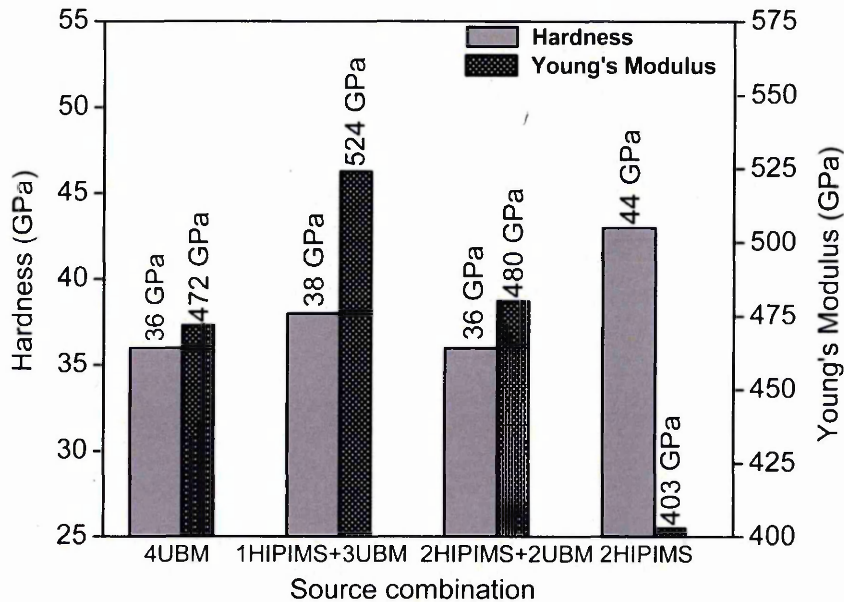

Figure 4.8 Hardness and Young's modulus of TiN coatings as a function of source combination

The increase in the hardness is attributed to the densification of coating microstructure (elimination of voids) due to the increased ion bombardment by HIPIMS sources. The elimination of voids can limit propagation of dislocations, improve resistance to deformation and hence can increase the coating hardness. The increased residual stress due to HIPIMS is also a possible cause for the enhanced hardness [3].

4.5.2 Coefficient of friction and wear coefficient

The wear behaviour of TiN coatings was evaluated by pin on disc tests in dry sliding wear conditions. The COF (μ) of TiN coatings against number of laps is plotted in Fig. 4.9. The average COF and COW (K_c) of TiN coatings deposited with increasing degree of HIPIMS utilisation [bias voltage: -50 V, coil current: 3 A and working pressure: 0.3 Pa] are listed in Table 4.2. For all the coatings, the COF started with the maximum value and the friction coefficient curve was smooth for few thousand laps for pure UBM, 1HIPIMS + 3UBM and 2HIPIMS + 2UBM coatings. Over a few thousand

laps of sliding, the COF deviated from the maximum or average values and reached to the minimum values before increasing again to high values (less compared to the maximum value). And, also the friction curves exhibited high noise, which is typical of sliding wear processes with a large amount of debris involved in a three-body rolling contact mechanism [4]. Similar behaviour was observed for the pure HIPIMS grown coating after a few hundred laps of sliding. This coating exhibited the lowest COF of 0.86. The COF of 1HIPIMS + 3UBM and 2HIPIMS + 2UBM grown coatings was almost equal in the range of 1.04. The pure UBM grown coating showed the highest COF of 1.18. The decreased COF with increasing degree of HIPIMS utilisation is attributed to the smooth surface morphology (reduced asperity contacts) produced by the HIPIMS. Generally, the friction behaviour of thin films has been discussed with the development of a tribofilm which is usually an oxide based on components from the coating and the counterpart [5].

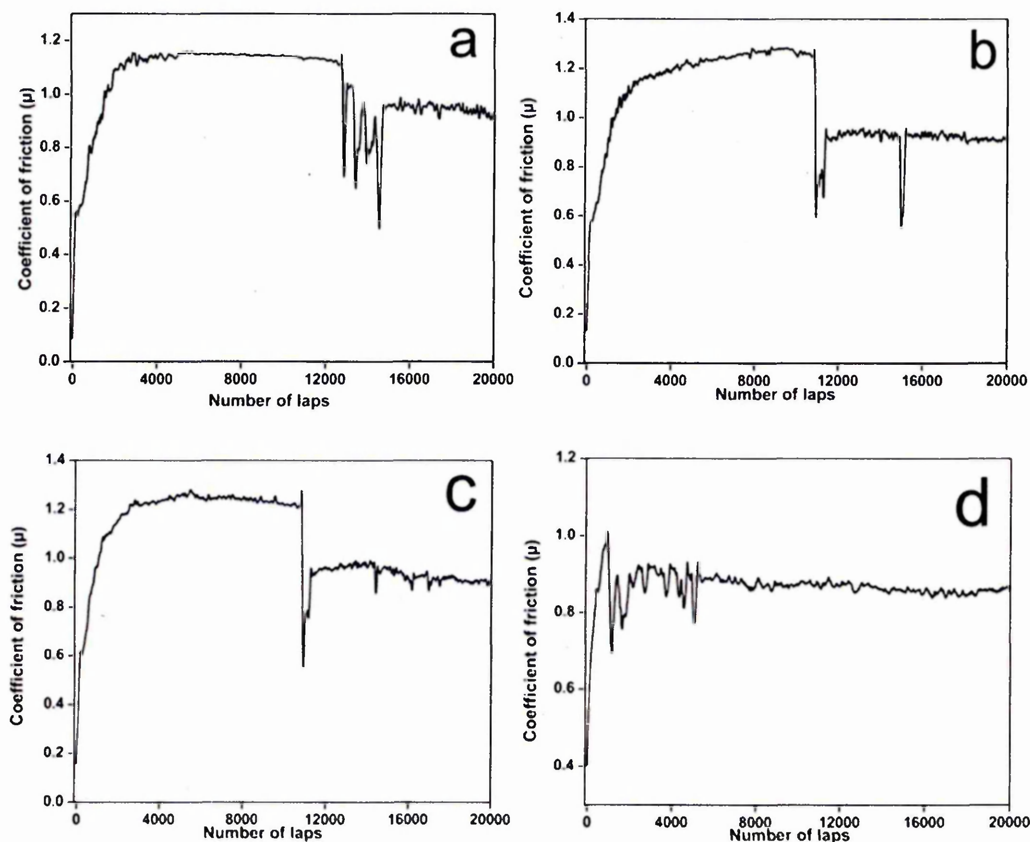

Figure 4.9 Coefficient of friction curves of TiN coatings deposited using various HIPIMS/UBM source combinations

Table 4.2 Summary of tribological properties of TiN coatings

Source combination	Average COF (μ)	COW(K_c) ($m^3N^{-1}m^{-1}$)
Pure UBM	1.18	1.145×10^{-14}
1HIPIMS + 3UBM	1.04	1.056×10^{-14}
2HIPIMS + 2UBM	1.06	9.325×10^{-15}
Pure HIPIMS	0.86	6.705×10^{-15}

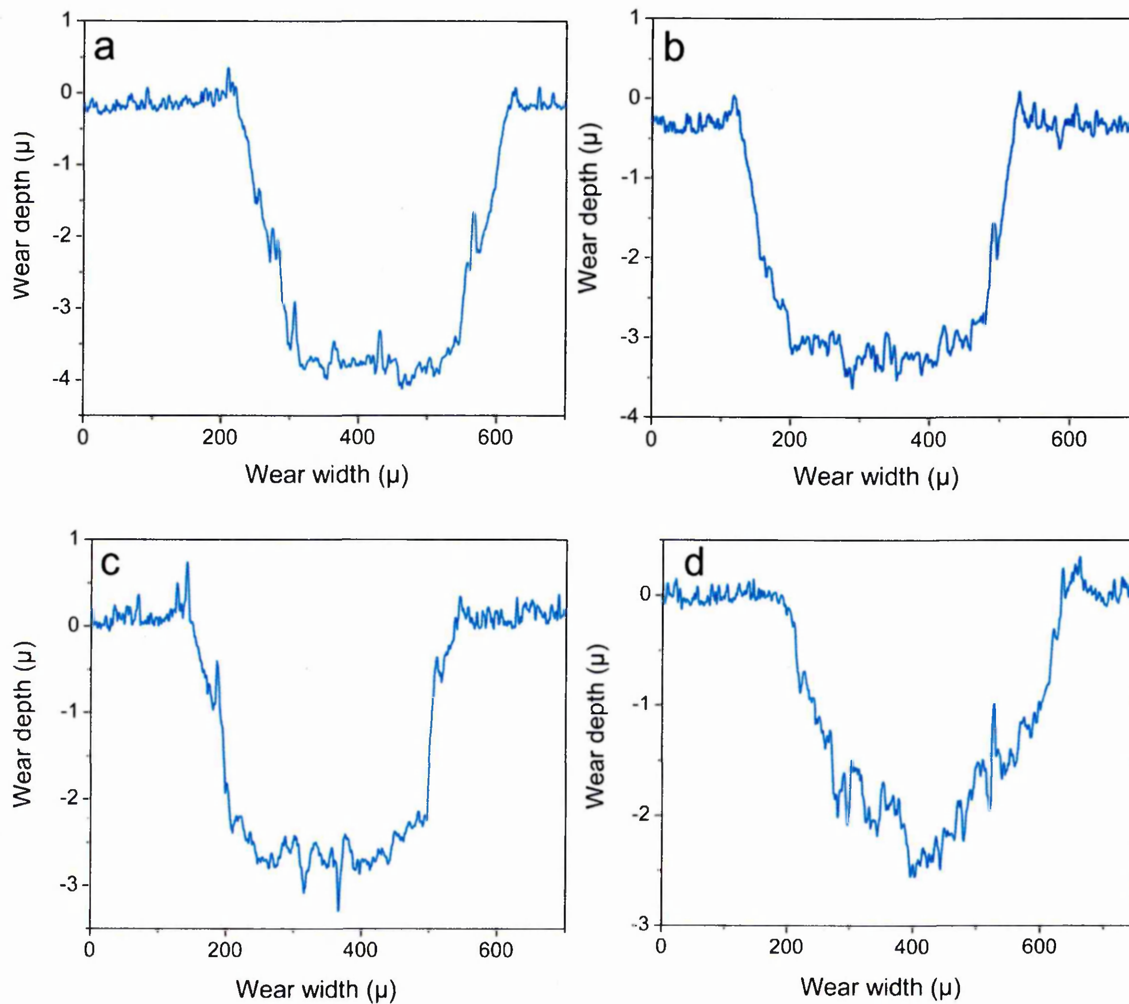

Figure 4.10 Wear depth and width profile of TiN coatings slid against Al_2O_3 ball (diameter of 6 mm): a) pure UBM; b) 1HIPIMS + 3UBM; c) 2HIPIMS + 2UBM; d) pure HIPIMS

Wear profile is measured by the Dektak surface profiler after the tribology test and the results are shown in Fig. 4.10. The wear depth values confirm that the Al_2O_3

ball reached the substrate during the tribology test of all four coatings. It was found to be decreased with increasing degree of HIPIMS utilisation. For pure UBM grown TiN coating, it was ~ 4 μm. It decreased to ~ 3 μm for 1HIPIMS + 3UBM and 2HIPIMS + 2UBM grown TiN coatings. In case of pure HIPIMS grown coating it was only ~ 2.5 μm even though the pure HIPIMS coating was the thinnest of all coatings. The sliding COW (K_c) estimated using the above discussed wear profiles found to be decreased with increasing degree of HIPIMS utilisation. The K_c for pure UBM and 1HIPIMS + 3UBM grown TiN coating was 1.145×10^{-14} and 1.056×10^{-14} $m^3N^{-1}m^{-1}$ respectively which are one order of magnitude higher as compared to 2HIPIMS + 2UBM ($K_c = 9.325 \times 10^{-15}$ $m^3N^{-1}m^{-1}$) and pure HIPIMS ($K_c = 6.705 \times 10^{-15}$ $m^3N^{-1}m^{-1}$) coatings. The K_c and the wear depth values demonstrate that the wear resistance of TiN coatings enhanced with increasing degree of HIPIMS utilisation. The enhancement of wear resistance was attributed to high hardness and a high dense microstructure due to HIPIMS with strong bonding between the columns which is resistant to intercolumnar tensile crack formation while the intercolumnar slip will be hindered to a large extent. The coating then will act as a more homogenous monolithic system in which the removal of material during wear will occur mainly by a layer-by-layer mechanism which will result in generating small-scale debris as explained by Ehiasarian et al. [4]. In contrast, the voided, well-defined columnar structure is known to bend, deform plastically to significant depths and finally chip during wear, thus generating large scale debris and exhibiting inferior wear resistance [4].

4.6 Microstructure evolution

4.6.1 Effect of the degree of HIPIMS utilisation on the microstructure of TiN coatings

Fig. 4.11 depicts the SEM cross-section images of TiN coatings deposited by four different source combinations [bias voltage: -50 V, coil current: 3 A and working pressure: 0.3 Pa]. The microstructure was columnar for all the coatings but with distinct differences as the HIPIMS contribution in the process was increased. The column tops were rough with voided region along the column boundaries for both the pure UBM and 1HIPIMS + 3UBM coatings. This type of microstructure evolution is attributed to low adatom mobility (low ion irradiation due to UBM dominated deposition techniques) which is insufficient for adatoms to diffuse through the open boundaries formed by the atomic shadowing effect.

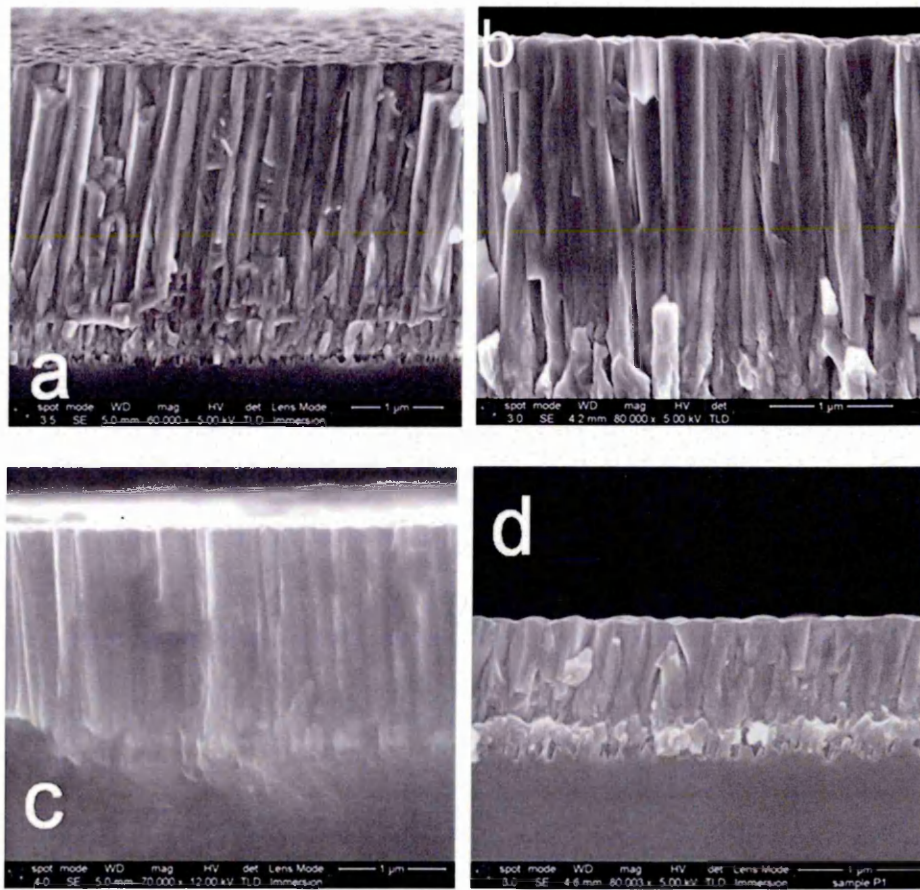

Figure 4.11 Cross-section SEM images of TiN coatings: a) pure UBM; b) 1HIPIMS + 3UBM; c) 2HIPIMS + 2UBM; d) pure HIPIMS

In contrast, the column tops were relatively smoother and wider without any voided region along the column boundaries for 2HIIPIMS+2UBM and pure HIPIMS coatings. This type of microstructure can be explained by the enhancement in the adatom mobility due to the relatively high ion to neutral ratio with sufficient energy by two HIPIMS sources involved in the process. These results can be correlated with OES measurements discussed in Sec. 4.1.1. Similar dense microstructure with smooth column tops has been reported for CrN coating deposited by HIPIMS technique [5].

4.6.2 Effect of bias voltage on the microstructure of TiN coatings

Fig. 4.12 shows the SEM cross-section images of 1HIPIMS + 3UBM grown TiN coatings at different bias voltages [coil current: 3 A and working pressure: 0.3 Pa] to discuss the effect of bias voltage on the microstructure.

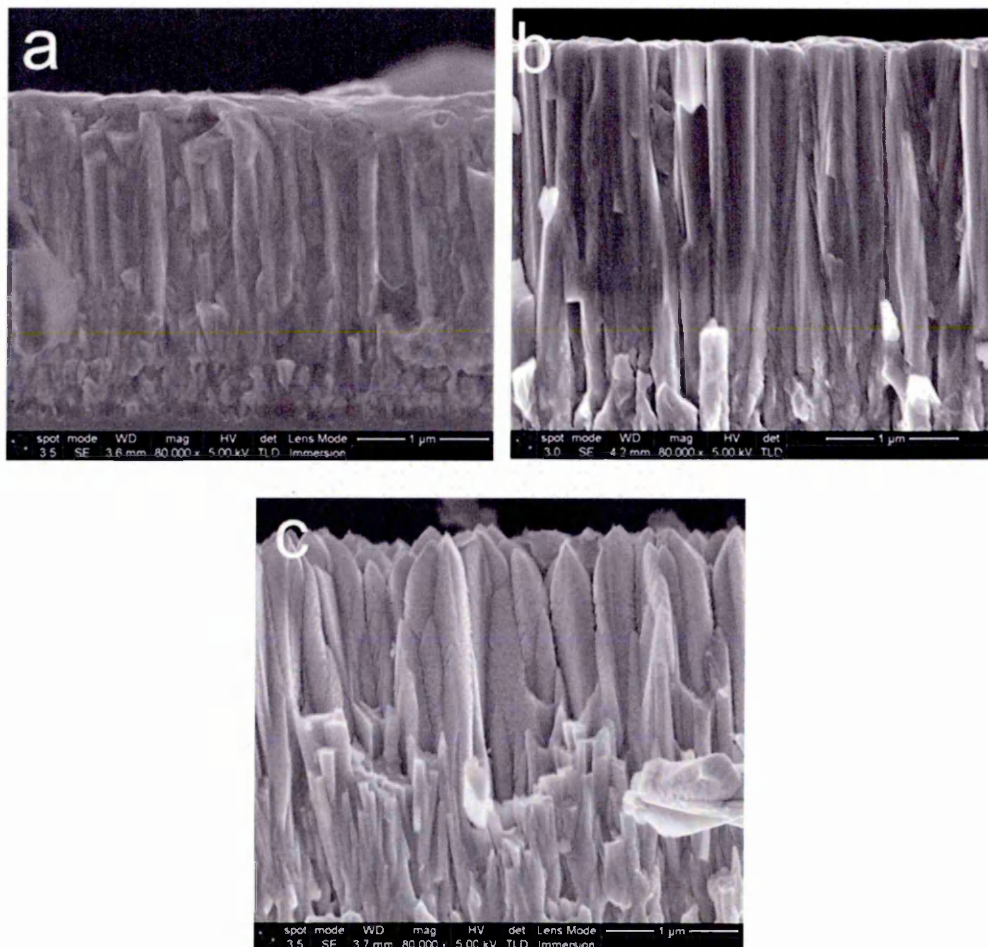

Figure 4.12 Cross-section SEM images of 1HIPIMS + 3UBM TiN coatings deposited at various bias voltages: a) -75 V; b) -50 V; c) floating potential

In magnetron sputtering, the ion irradiation in the substrate region is controlled by applying negative substrate bias voltage to the substrate. As anticipated, the columnar structure was relatively dense and smooth without any voids along the columnar boundaries for the coating deposited at - 75 V of substrate bias. A pronounced, rough columnar structure with voids along the column boundaries was observed for the coating deposited at - 50 V of substrate bias. It was interesting to note that the 1HIPIMS + 3UBM grown coating at floating potential showed dome shaped, extremely rough column tops with inter columnar voids which resembles the pure UBM coating deposited at floating potential. Similar microstructure was observed for TiAlN coating deposited by dc magnetron sputtering [7].

4.6.3 Effect of coil current on the microstructure of TiN coatings

Fig. 4.13 shows the SEM cross-section images of 1HIPIMS + 3UBM grown TiN coatings at different coil currents [bias voltage: -50 V and working pressure: 0.3 Pa] to discuss the effect of coil current on the microstructure. The coil current alters the degree of metal flux in the plasma (Sec. 4.1.2) which in turn plays a vital role in determining the microstructure of the coatings.

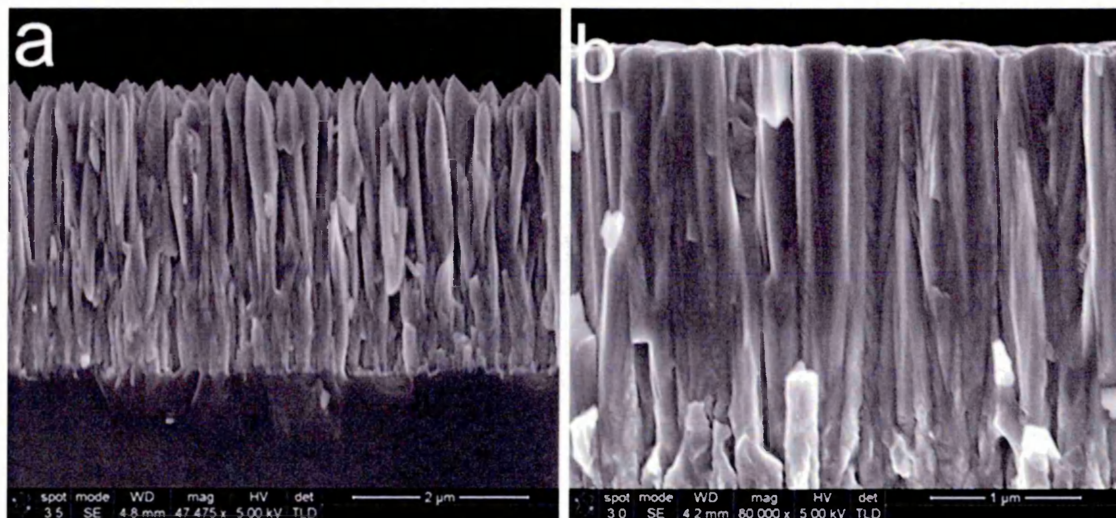

Figure 4.13 Cross-section SEM images of 1HIPIMS + 3UBM TiN coatings deposited at various coil currents and bias voltage of - 50 V: a) 0 A; b) 3 A

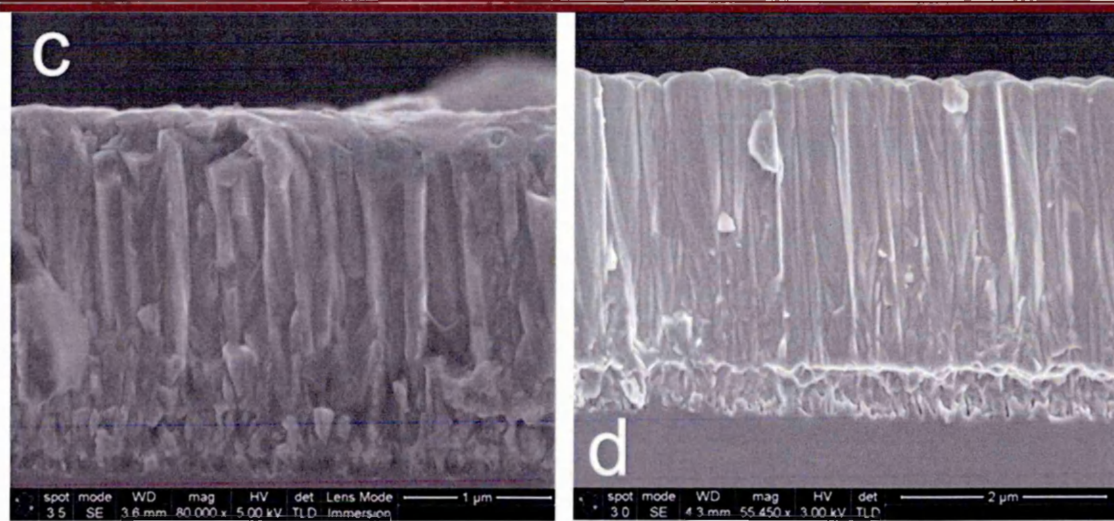

Figure 4.13 Cross-section SEM images of 1HIPIMS + 3UBM TiN coatings deposited at various coil currents and bias voltage of - 75 V: c) 3 A; d) 6 A

The dome shaped, under dense microstructure transformed to a relatively dense microstructure with fewer inter-columnar voids when the coil current was increased from 0 A to 3 A. The substrate bias was kept constant at - 50 V for these experiments [Fig. 4.13 (a, b)]. Further densification of an already dense coating deposited at - 75 V of substrate bias and coil current of 3 A was observed when the coil current was increased to 6 A [Fig. 4.13 (c, d)].

In summary, the quality of the microstructure deteriorates (which in turn deteriorates the performance of the coatings) when HIPIMS is strongly "diluted" in UBM and operated in "weak" ionisation conditions.

The microstructure investigation using SEM revealed that the structure densification can be achieved by high ion irradiation. It was evident that the high ion irradiation can be facilitated by many different ways such as using HIPIMS for the deposition of coatings, increasing bias voltage and increasing coil current, etc. However, it has been well documented that increasing the substrate bias voltage or using HIPIMS for the deposition of coating generates high residual compressive stress in the coatings. Therefore, the effect of HIPIMS utilisation and bias voltage on residual stress in TiN coatings was investigated.

4.7 Determination of residual stress in TiN coatings

Generally, thin film coatings develop compressive stress due to the bombardment of atoms or ions with energies of tens or hundreds of electronvolts during the growth of the coating. Notably, thin film coatings deposited by HIPIMS exhibit excessive compressive stress due to the bombardment of high energetic metal ion rich deposition flux compared to the coatings grown by other magnetron sputtering techniques such as dc-magnetron sputtering. Even though this high energetic ion bombardment favours the formation of dense coatings with properties close to those of bulk material, unfortunately the excessive residual stress might not be suitable for many applications as it causes coating delamination and stress induced corrosion [8]. Hence it is essential to address the effect of substrate bias voltage (accelerates ionised species towards the substrate), degree of HIPIMS utilisation and coil current (alters the degree of ionisation) on the residual compressive stress in TiN coatings deposited by various HIPIMS/UBM source combinations to determine the optimum deposition conditions. The residual stress was determined using X-ray diffraction method and nanoindentation test (Sec. 3.3.1 and Sec. 3.3.3). Glancing angle X-ray geometry was used for this purpose.

4.7.1 Effect of the degree of HIPIMS utilisation on residual stress in TiN coatings

The residual stress (σ) was calculated from the slope of the least-squares fit of the plot of a_Ψ versus $\sin^2 \Psi$. Fig. 4.14 (a-c*) shows GA-XRD patterns and the least-squares fit of the plot of a_Ψ vs. $\sin^2 \Psi$ for TiN coatings deposited with three different source combinations with increasing degree of HIPIMS utilisation. Table 4.3 lists the calculated residual stress in the coatings. For these experiments, the substrate bias voltage and the coil current were kept at - 50 V and 3 A respectively.

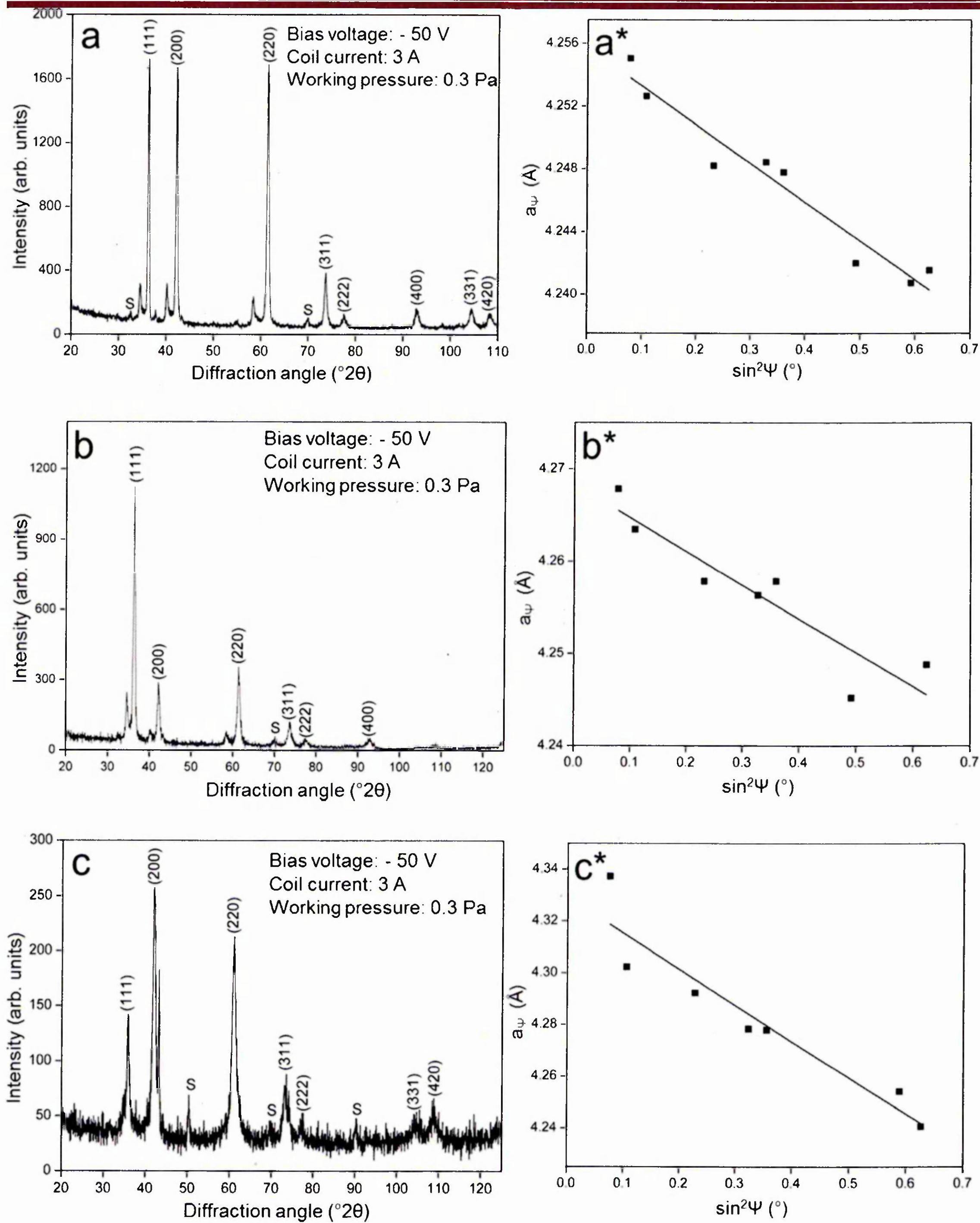

Figure 4.14 Glancing angle XRD pattern & Lattice parameter (a_Ψ) as a function of $sin^2\Psi$: (a & a*) 1HIPIMS + 3UBM; (b & b*) 2HIPIMS + 2UBM; (c & c*) pure HIPIMS (2HIPIMS)

Table 4.3. Residual stress in TiN coatings deposited with different source combination

TiN coating Source combination		Stress (GPa)
1HIPIMS + 3UBM	Bias Voltage: -50 V Coil current: 3 A	-2.394
2HIPIMS + 2UBM		-3.574
Pure HIPIMS		-10.460

The residual stress in the coatings increased with increasing degree of HIPIMS utilisation. The 1HIPIMS + 3UBM grown TiN coating exhibited the lowest residual stress of - 2.394 GPa which is a factor of ~ 1.5 to ~ 4.3 lower as compared to 2HIPIMS + 2UBM and pure HIPIMS grown TiN coatings. The increase in stress was attributed to the enhanced metal ion bombardment by increased number of HIPIMS sources used for the deposition.

4.7.2 Effect of coil current on residual stress in TiN coatings

The GA-XRD patterns and the least-squares fit of the plots (a_Ψ vs. $\sin^2 \Psi$) which were used for calculating the residual stress in TiN coatings deposited at different coil currents using different source combinations are shown in Fig. 4.14 (a, a*, b, b*, c & c*) and 4.15 (a, a*, b, b* c & c*). The residual stress in the coatings is listed in Table 4.4 and the Fig. 4.16 illustrates the same. The bias voltage and total pressure were kept constant at -50 V and 0.3 Pa respectively, for these experiments. The role of coil current during the deposition is explained in Sec. 4.1.2.

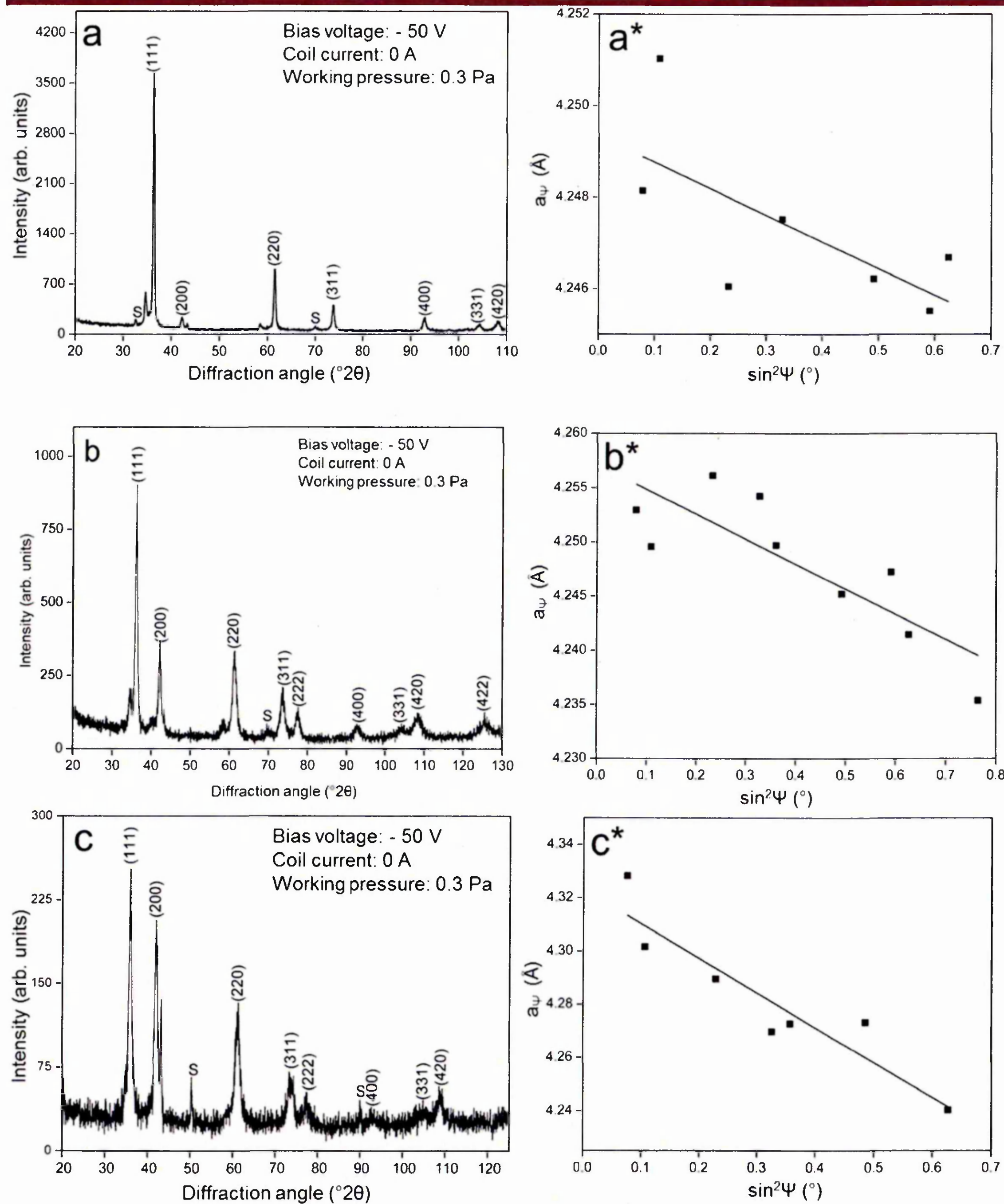

Figure 4.15 Glancing angle XRD pattern & Lattice parameter (a_Ψ) as a function of $sin^2\Psi$: (a & a*) 1HIPIMS + 3UBM; (b & b*) 2HIPIMS + 2UBM; (c & c*) pure HIPIMS (2HIPIMS)

The residual stress of TiN coatings increased with increasing coil current due to the enhancement in the degree of ionisation for all the three combinations [see table 4.4]. Analysis of stress gradients [see Fig. 4.12] showed that the pure HIPIMS grown TiN coatings exhibited the lowest value of 0.2 when increasing the coil current from 0 A to 3 A. In the case of 2HIPIMS + 2UBM and 1HIPIMS + 3UBM grown TiN

coatings, the stress gradient was found to be 0.75 and 0.73 respectively. The very low stress gradient for pure HIPIMS coatings indicated that the rate of change of stress in such coatings was much less as compared to the 1HIPIMS + 3UBM and 2HIPIMS + 2UBM grown coatings while increasing the coil current.

Table 4.4 Residual stress in TiN coatings deposited by different source combinations at different coil currents

TiN coating Source combination	Coil current (A)	Stress (GPa)
1HIPIMS + 3UBM Bias voltage: -50 V	0	-0.219
	3	-2.394
2HIPIMS + 2UBM Coil current: -50 V	0	-1.321
	3	-3.574
Pure HIPIMS Coil current: -50 V	0	-9.857
	3	-10.460

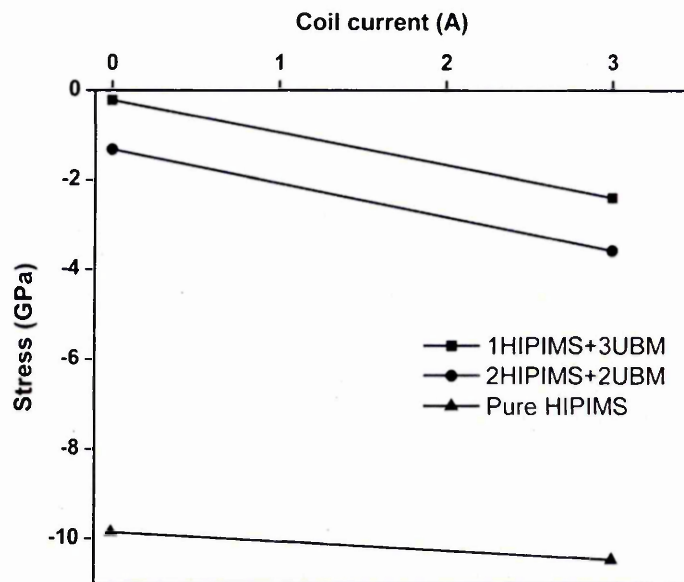

Figure 4.16 Effect of coil current on the residual stress of TiN coatings deposited with different source combinations

4.7.3 Effect of bias voltage on residual stress in TiN coatings

The GA-XRD patterns and the least-squares fit of the plots (a_{Ψ} vs. $\sin^2 \Psi$) which were used for calculating the residual stress in the coatings deposited at different bias

voltages using different source combinations are shown in fig. 4.14 (a, a*, b & b*), 4.15 (c & c*), 4.17 (a, a*, b, b*, c, c*, d, d*, e & e*) .The residual stress in the coatings is listed in Table 4.5 and Fig. 4.18 illustrates the same. For all the processes, the total pressure was 0.3 Pa. The coil current was 3 A for the 1HIPIMS + 3HIPIMS and 2HIPIMS + 2UBM combinations. The pure HIPIMS coatings were deposited at 0 A of coil current not to generate excessive compressive stress since any increase in the coil current [0 A to 3 A] would further increase the stress of the highly stressed pure HIPIMS coatings.

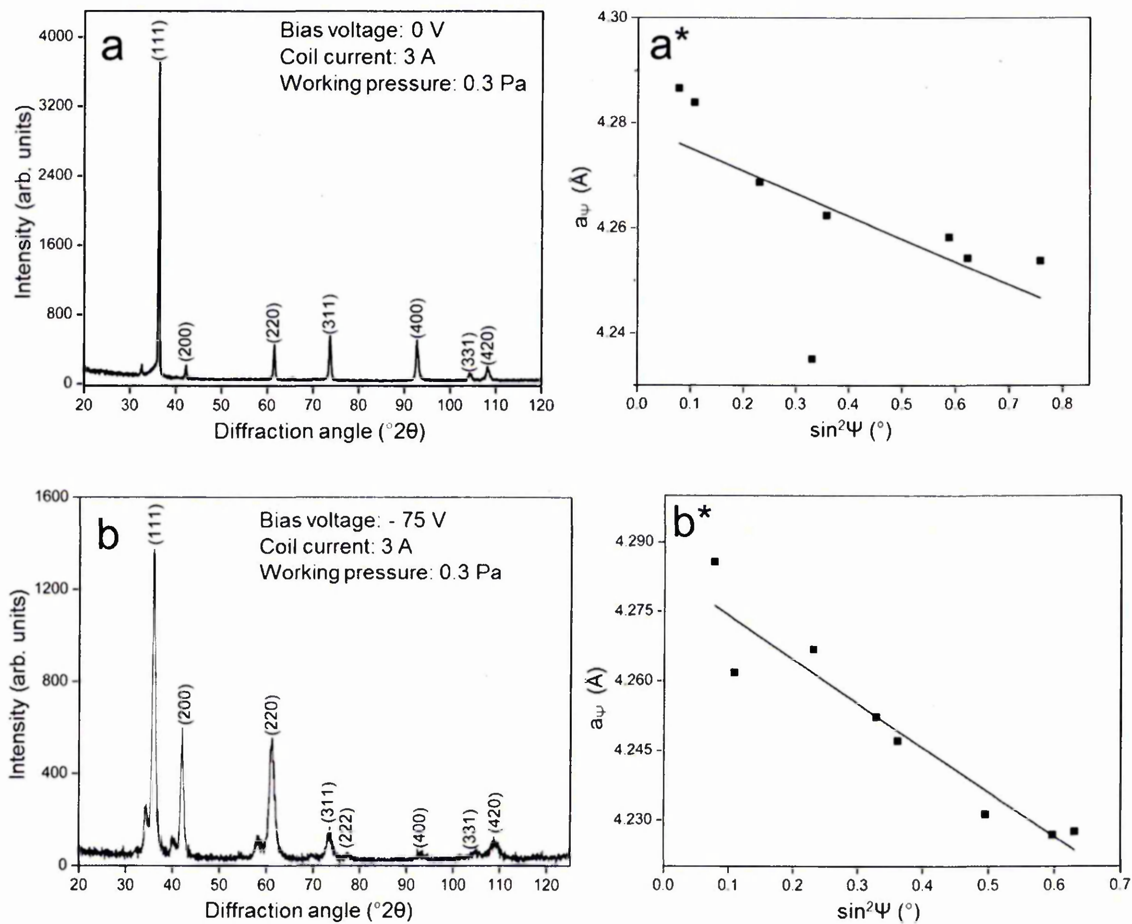

Figure 4.17 Glancing angle XRD pattern & Lattice parameter (a_Ψ) as a function of $\sin^2\Psi$: (a & a*) 1HIPIMS + 3UBM; (b & b*) 1HIPIMS + 3UBM

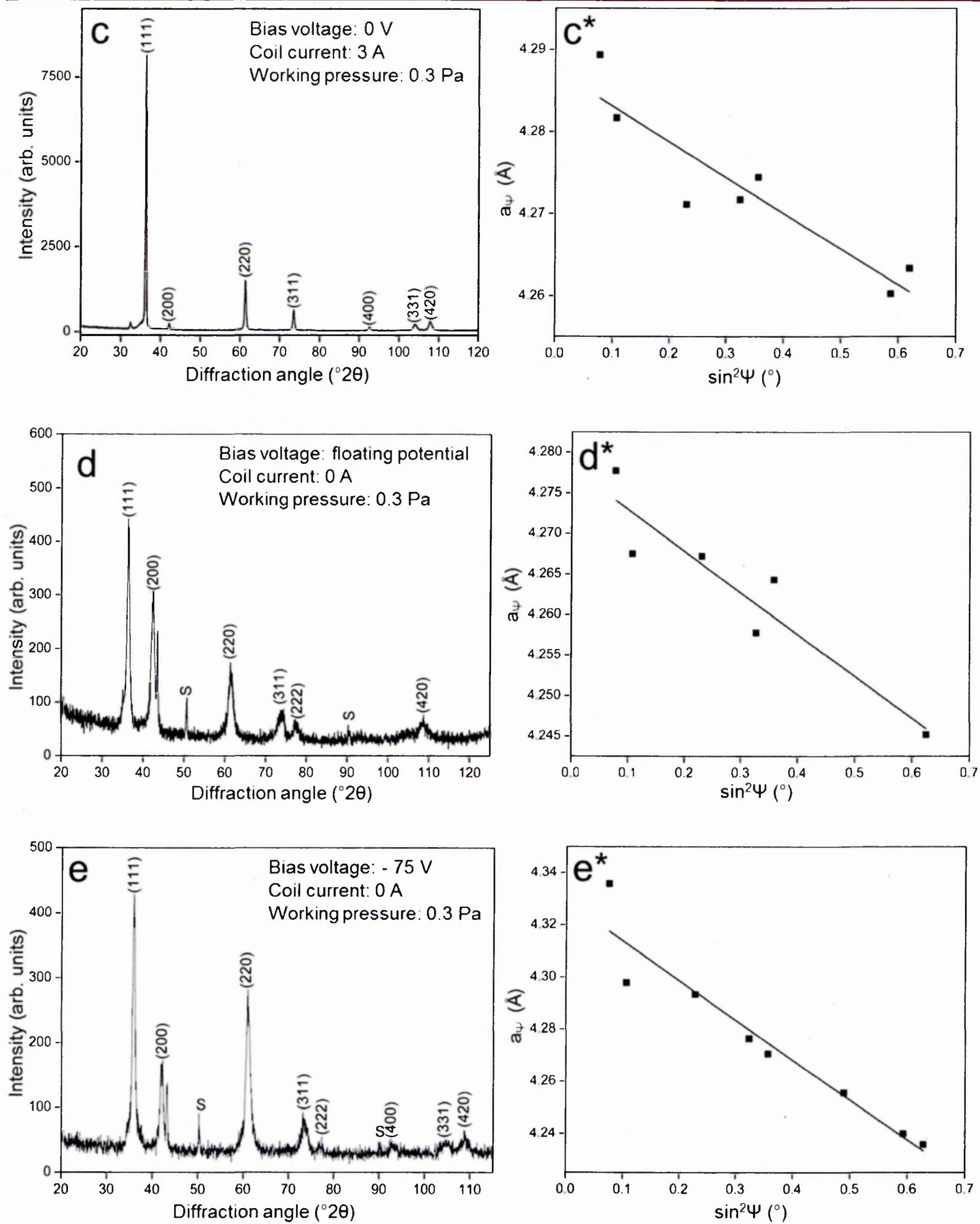

Figure 4.17 Glancing angle XRD pattern & Lattice parameter (a_Ψ) as a function of $\sin^2\Psi$: (c & c*) 2HIPIMS + 2UBM; (d & d*) pure HIPIMS (2HIPIMS); (e & e*) pure HIPIMS (2HIPIMS)

Table 4.5. Residual stress in TiN coatings deposited by different source combinations at different bias voltages

TiN coating Source combination	Bias voltage (V)	Stress (GPa)
1HIPIMS + 3UBM Coil current: 3 A	floating potential	-1.870
	- 50	-2.394
	-75	-8.890
2HIPIMS + 2UBM Coil current: 3 A	floating potential	-2.655
	-50	-3.574
Pure HIPIMS Coil current: 0 A	floating potential	-3.282
	-50	-9.857
	-75	-11.670

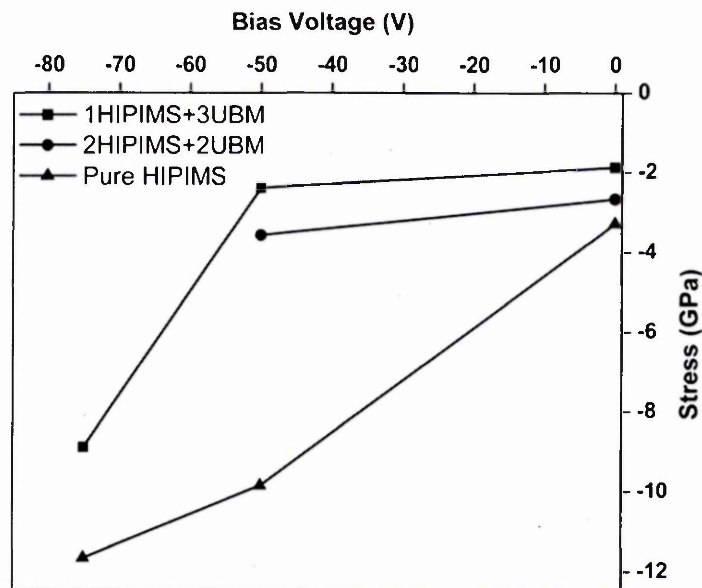

Figure 4.18 Effect of bias voltage on the residual stress in TiN coatings deposited with different source combinations

The residual stress of TiN coatings increased with increasing bias voltage due to the enhancement in the ion bombardment for all the three combinations [Table 4.5]. A detailed analysis of stress gradients [Fig. 4.18] showed that the stress gradient (0.07) of pure HIPIMS coatings deposited at - 50 V and - 75 V was a factor of ~ 1.85 lower than

the stress gradient (0.13) of the same coatings deposited at floating potential and - 50 V. In contrast, the stress gradient (0.26) of 1HIPIMS + 3UBM coatings deposited at - 50 V and -75 V was a factor of 26 higher than that of the stress gradient (0.01) of such coatings deposited at floating potential and -50 V. These results confirm that for pure HIPIMS coatings, the stress increases with bias voltage at a lower rate compared to the 1HIPIMS + 3UBM coatings. Similar behaviour for pure HIPIMS coatings was observed with increasing coil current also [Sec. 4.7.2].

4.8 Effect of bias voltage on the texture evolution of TiN coatings

The texture evolution of TiN coatings deposited by combined HIPIMS/UBM technology was analysed using X - ray diffraction (θ-2θ, BB geometry) technique. Fig. 4.19 and Fig. 4.20 show BB-XRD patterns of 1HIPIMS + 3UBM and 2HIPIMS + 2UBM grown TiN coatings at various bias voltages [working pressure: 0.3 Pa]. Table 4.6 shows the texture parameter of such coatings.

Table 4.6.Texture of TiN coatings deposited by combined HIPIMS/UBM technique

TiN coating Source combination	Bias voltage (V)	[111]	[200]	[220]	[311]	[222]
1HIPIMS + 3UBM Coil current - 3 A	floating potential	57.27	0.22	0.27	4.60	37.63
	-50	59.29	1.06	0.51	2.49	36.64
	-75	57.40	1.40	0.53	16.75	23.90
2HIPIMS + 2UBM Coil current - 3 A	floating potential	57.77	0.45	0.42	4.97	36.40
	-50	60.82	0.99	2.27	7.17	28.75

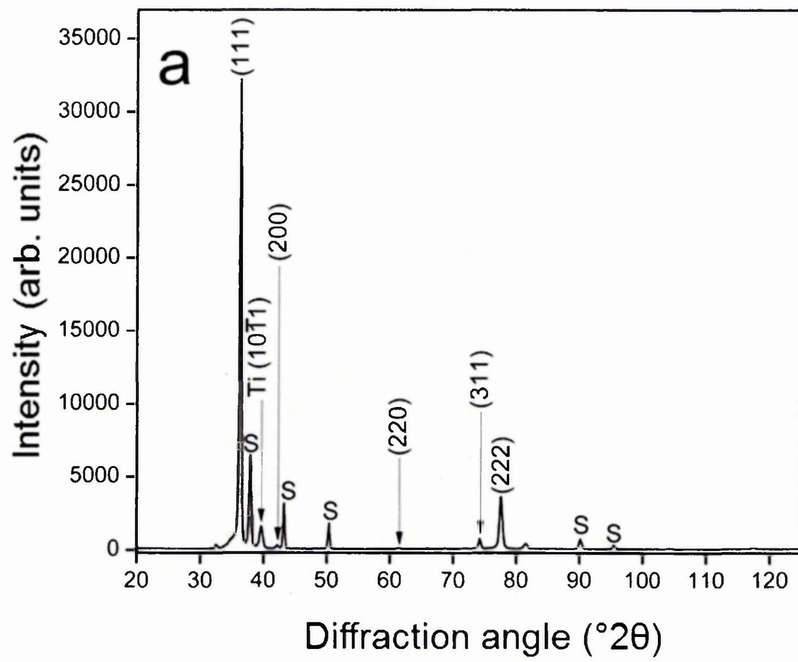

Figure 4.19 (a) BB XRD pattern of 1HIPIMS + 3UBM grown TiN coating (substrate bias: floating potential and coil current: 3A)

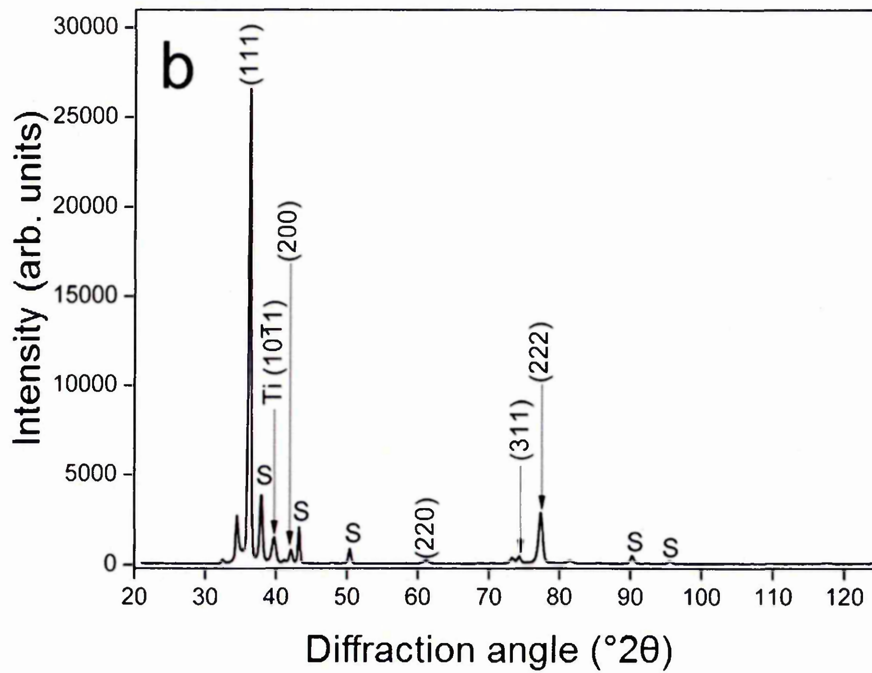

Figure 4.19 (b) BB XRD patterns of 1HIPIMS + 3UBM grown TiN coating (substrate bias: - 50V and coil current: 3A)

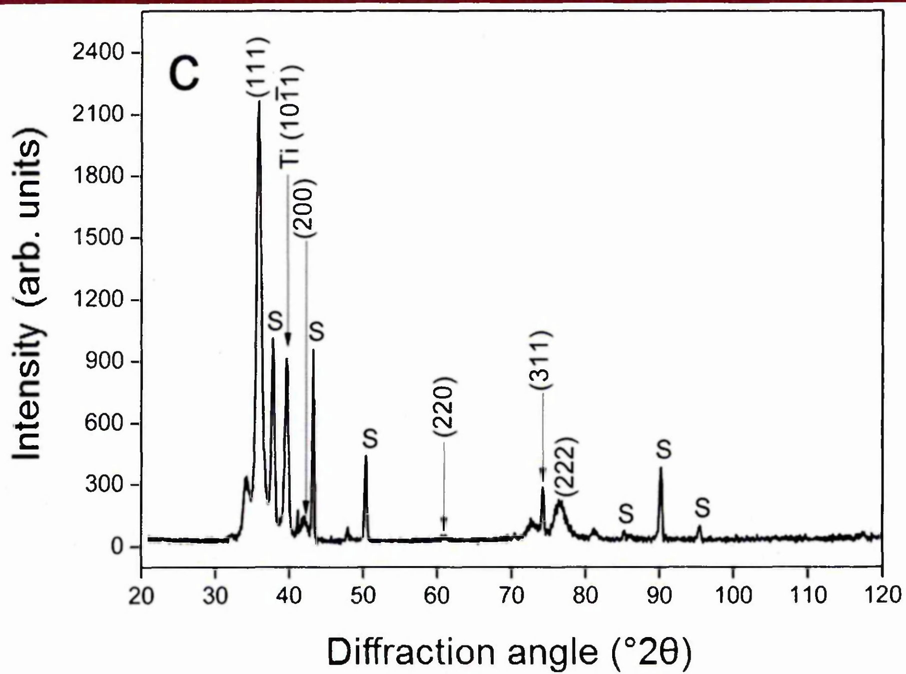

Figure 4.19 (c) BB XRD patterns of 1HIPIMS + 3UBM grown TiN coating (substrate bias: -75 V and coil current: 3A)

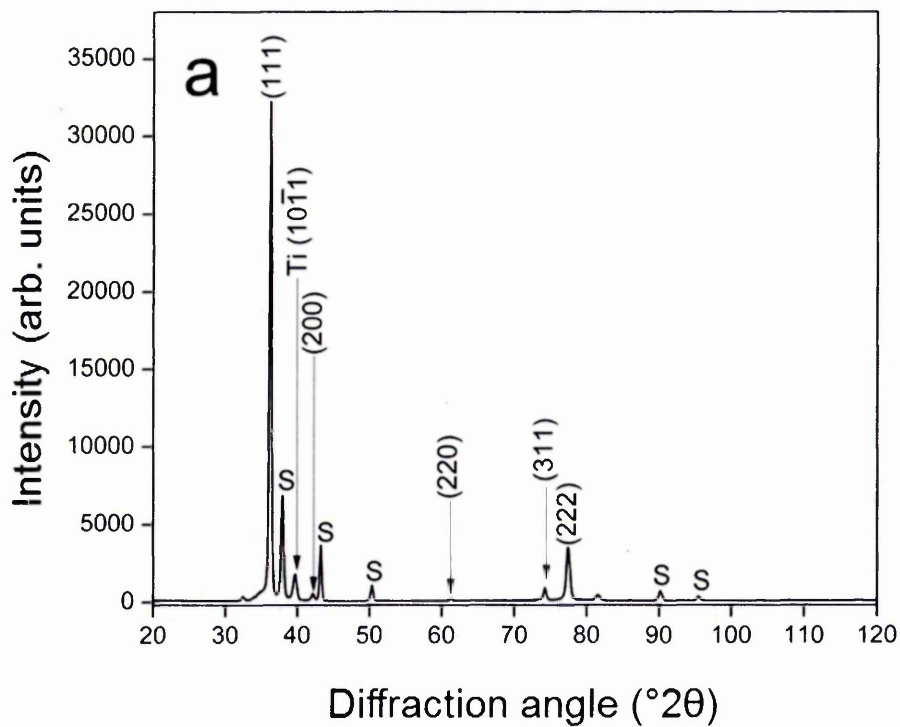

Figure 4.20 (a) BB XRD patterns of 2HIPIMS + 2UBM grown TiN coating (substrate bias: floating potential and coil current: 3A)

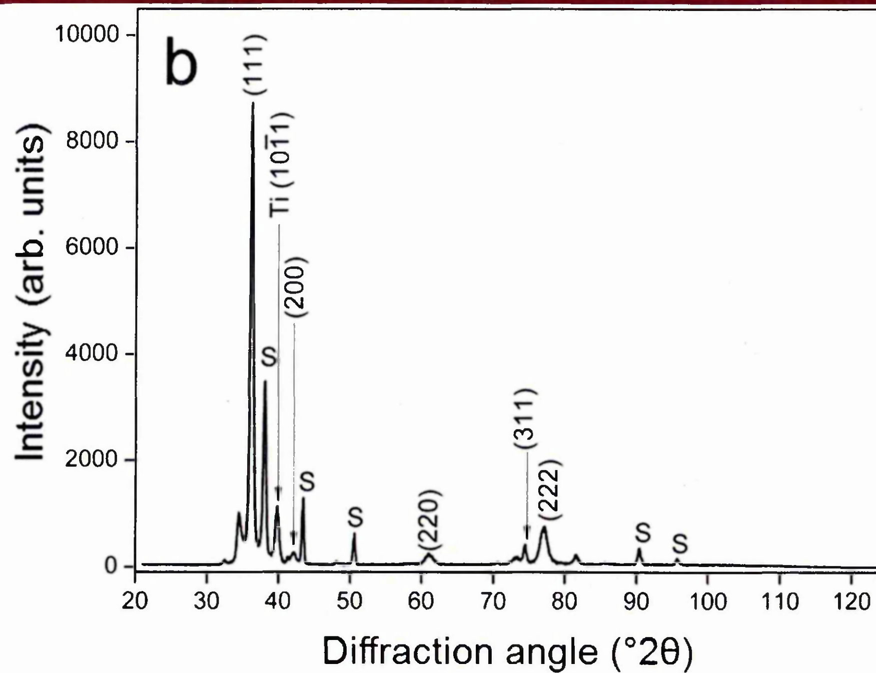

Figure 4.20 (b) BB XRD patterns of 2HIPIMS + 2UBM grown TiN coating (substrate bias: -50 V and coil current: 3A)

All of the coatings exhibited a strong [111] preferred orientation with a small volume fraction of [200], [220] and [311] grains. Moderate [222] texture (second order reflection from the plane [111]) was also found. It is quite usual that the TiN films exhibit [111] preferred orientation. However, coatings with [200] and [220] preferred orientations have also been reported. Several models have been proposed to explain the development of different crystallographic orientation in TiN coatings [9 - 12]. According to 'overall energy model', at small film thicknesses, the [200] texture develops with a minimum surface energy whereas at a large film thickness, the [111] texture develops with the lowest strain energy [9]. However, Mahieu et al. argue that the overall energy model is limited or incorrect [10]. Gall et al. found that the [111] oriented grain growth is favoured when the incident particles are only Ti atoms and N_2 molecules during the deposition. However, if the deposition flux contains a high density of atomic N, or collisionally dissociating N_2^+ ions, the corresponding increase in the steady state N coverage dramatically changed the texture changed to [001] [11].

The volume fraction of [200] orientation increased with increasing bias voltage for all of the coatings. It has been reported that the volume fraction of [200] in TiN film increases with increasing ion energy (substrate bias). However, when the ion to neutral ratio is ≤ 1, the ion energy required to complete the transition is > 800 eV [10]. Ehisarian et al. demonstrated that the preferred orientation of TiN coatings deposited by HIPIMS changed from [111] to [200] while increasing the peak current from 5 A to 30 A due to the increased ion flux and increased mobility on the surface [3]. It can be concluded that the volume fraction of [200] increased with increasing bias voltage and degree of HIPIMS utilisation.

4.9 Effect of degree of HIPIMS utilisation on the surface roughness of TiN coatings

The average surface roughness values (R_a) of TiN coatings deposited with increasing degree of HIPIMS utilisation [bias voltage: -50 V, coil current: 3 A and working pressure: 0.3 Pa] are listed in Table 4.7. These values can be correlated with the plan-view SEM images in Fig. 4.21.

Table 4.7. Surface roughness of TiN coatings deposited by various HIPIMS/UBM sources

Source combination	Average surface roughness (μm)
Pure UBM (4 UBM)	0.050
1HIPIMS + 3UBM	0.043
2HIPIMS + 2UBM	0.040
Pure HIPIMS (2HIPIMS)	0.037

The pure UBM coating was found to be the roughest with a R_a of 0.05 μm and Fig. 4.21 (a) also suggests the same with large numbers of craters on the surface. The R_a decreased with increasing degree of HIPIMS utilisation. The R_a for the pure HIPIMS coating was 0.037 μm. The surface morphology of TiN coatings deposited using

HIPIMS sources [Fig. 4.21 (b – d)] exhibited fewer craters as compared to the pure UBM coating. The R_a enhancement is attributed to the wider columns with smooth column tops (Sec. 4.6) due to the increased ad – atom mobility of the condensing species provided by the HIPIMS sources. It can be concluded that the surface roughness improves with increasing degree of HIPIMS utilisation.

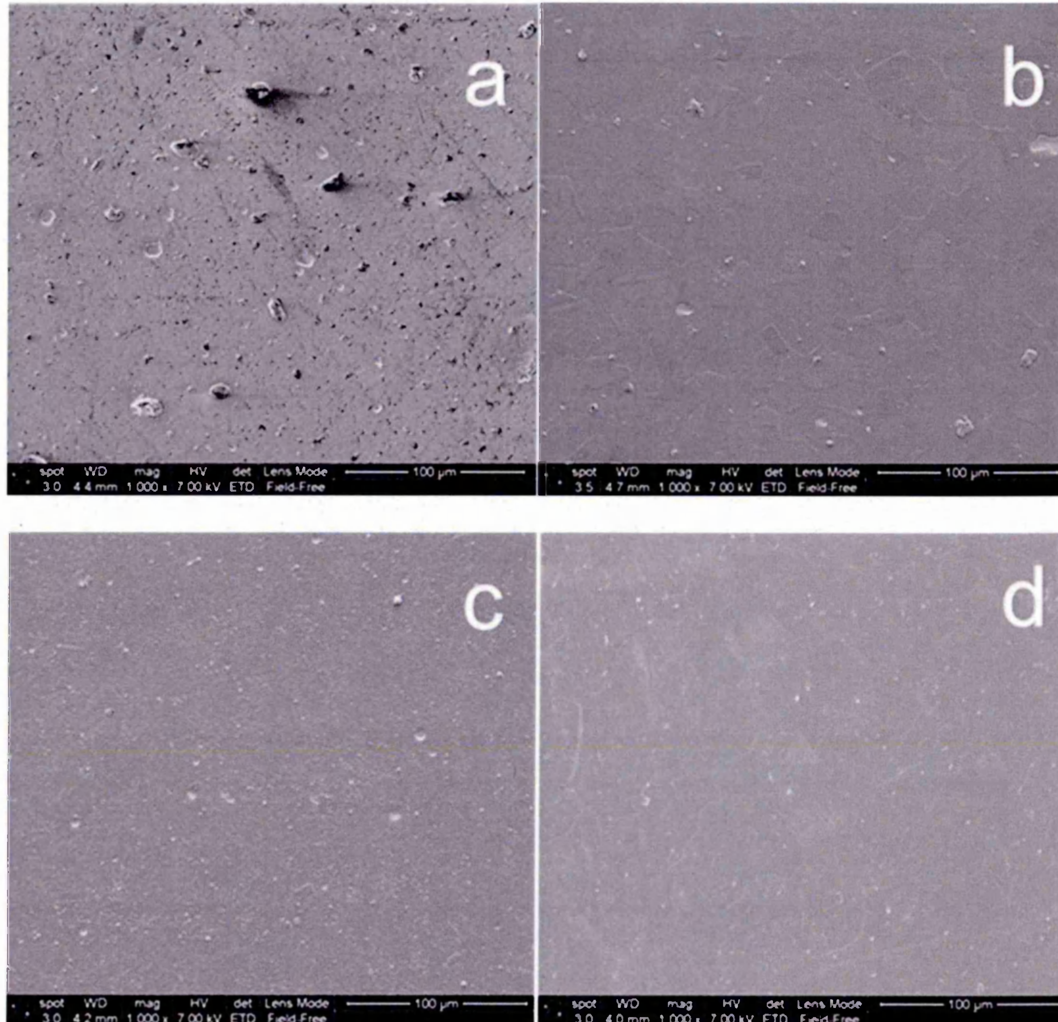

Figure 4.21 Plane view SEM images of as – deposited TiN coatings:
(a) pure UBM (4UBM); (b) 1HIPIMS + 3UBM; (c) 2HIPIMS + 2UBM;
(d) pure HIPIMS (2HIPIMS)

4.10 Effect of the degree of HIPIMS utilisation on corrosion resistance of TiN coatings

4.10.1 Potentiodynamic polarisation measurements

Fig. 4.22 shows the Tafel plots obtained for TiN coatings deposited with the four different HIPIMS/UBM source combinations [bias voltage: -50 V, coil current: 3 A and working pressure: 0.3 Pa].

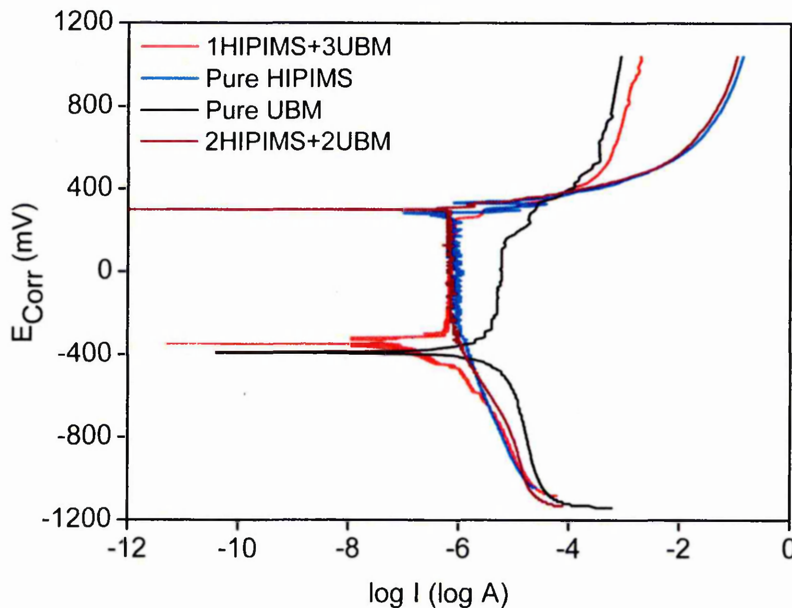

Figure 4.22 Potentiodynamic polarization curves of TiN coatings: (a) pure UBM (4UBM); (b) 1HIPIMS + 3UBM; (c) 2HIPIMS + 2UBM; (d) pure HIPIMS (2HIPIMS)

The E_{corr} for TiN coatings was found to be increased with increasing degree of HIPIMS utilisation. The E_{corr} for pure UBM and 1HIPIMS + 3UBM coating were about - 391 mV and - 348 mV respectively. The E_{corr} increased to about + 305 mV for 2HIPIMS + 2UBM and +282 mV for pure HIPIMS coating in the anodic range. The positive shift of the E_{corr} values suggested that the corrosion resistance of the coating improved with increasing degree of HIPIMS utilisation. This enhancement can be attributed to the extremely dense microstructure (Sec. 4.6) due to high energy ion bombardment (Sec. 4.1) on the surface of the growing film by HIPIMS sources. However the E_{corr} for 2HIPIMS + 2UBM coating is slightly higher than that of the pure

HIPIMS coating. The pure UBM and 1HIPIMS + 3UBM coatings exhibit a clear passive region and pitting potential in the anodic region. But a different corrosion mechanism was observed without them for the 2HIPIMS + 2UBM and Pure HIPIMS coatings. However the increased free corrosion potential values for these coatings confirm that they outperform the pure UBM and 1HIPIMS + 3UBM coatings. A similar behaviour was observed for CrN coating deposited by HIPIMS technique [5].

4.10.2 SEM investigation of corroded samples

To study the effect of corrosion on the microstructure, samples subjected to corrosion measurement were investigated under a scanning electron microscope. Fig. 4.23 shows the plan view SEM images of corroded samples deposited with various HIPIMS/UBM source combinations.

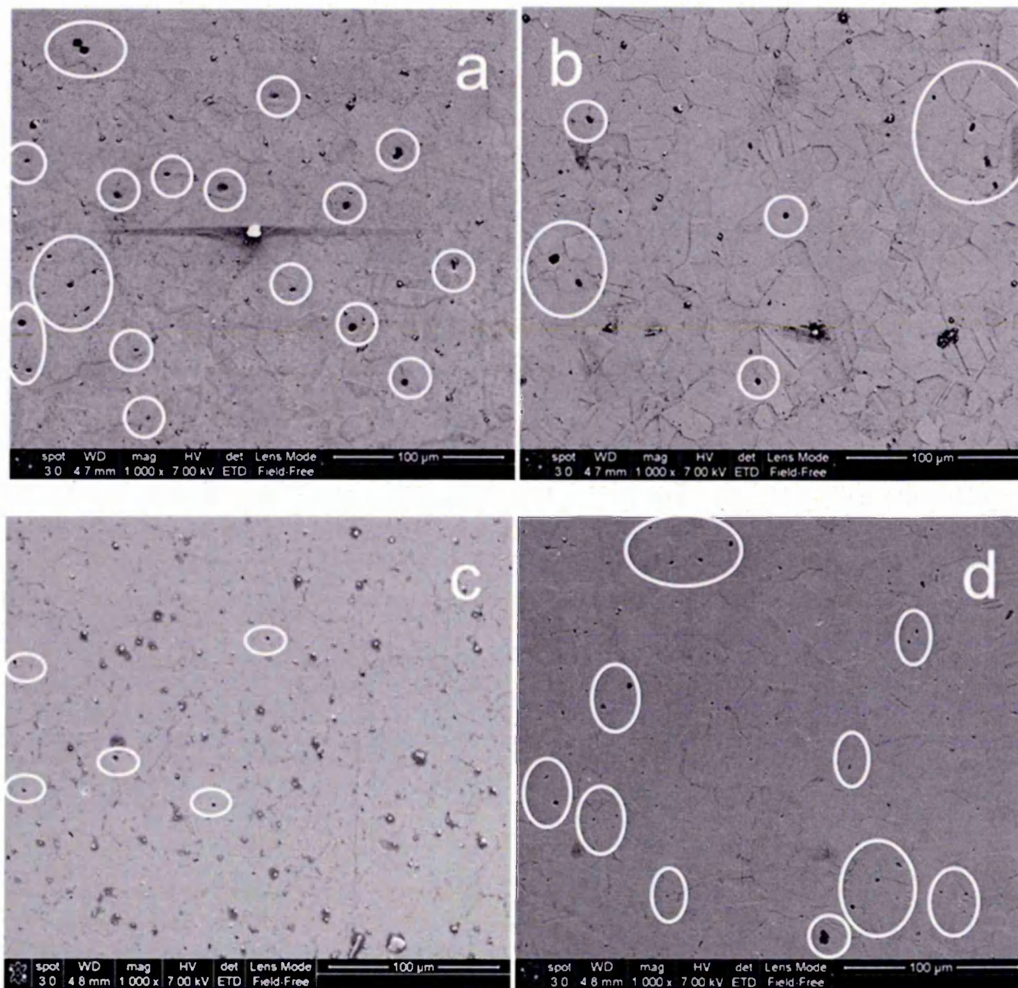

Figure 4.23 Plane view SEM images of TiN coatings after corrosion test: (a) pure UBM (4UBM); (b) 1HIPIMS + 3UBM; (c) 2HIPIMS + 2UBM; (d) pure HIPIMS (2HIPIMS)

The corrosion pits due to corrosion attack can be seen on all of the samples. These pits allow the electrolyte to react with the substrate, thus degrading the corrosion performance of the coatings. Interestingly pure UBM and 1HIPIMS + 3UBM coatings exhibited a large number of such pits than the other two coatings (2HIPIMS + 2 UBM and pure HIPIMS) which is a clear indication for poor corrosion resistance of UBM dominated coatings. These results can be correlated with the E_{corr} values of TiN coatings obtained using the potentiodynamic polarisation method.

4.10.3 Raman spectroscopy

Raman analysis has been done to study the effect of corrosion on the coating surface since it is very sensitive in detecting the surface oxide formation. It is well known that a thin passive layer of TiO_2 is formed over TiN which is believed to provide corrosion resistance under corrosive environment [14, 15]. Moreover elements from the underlying substrate can also be seen on the surface due to the substrate corrosion. TiN coatings deposited on SS 304 substrates were subjected to corrosion in this study. It has been reported that oxides, hydroxides, oxy hydroxides, nitrates, nitrides, sulphates, chlorides and oxy chlorides of Fe, Cr and Ni could be formed due to SS corrosion as they are being the major constituents of stainless steel. However Raman analysis of any passive film is quite difficult as it is very complex [16]. Fig. 4.24 shows the Raman spectra of as deposited and corroded TiN coatings. Table 4.8 shows the assignment of various Raman peaks of as-deposited and corroded TiN coatings deposited using different HIPIMS/UBM combinations.

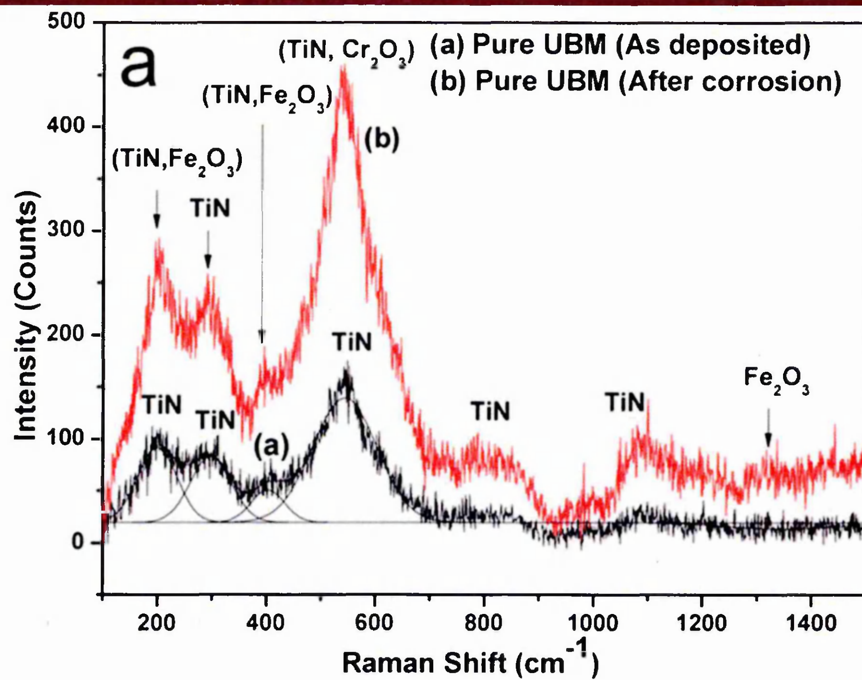

Figure 4.24 (a) Raman spectra of pure UBM TiN coating

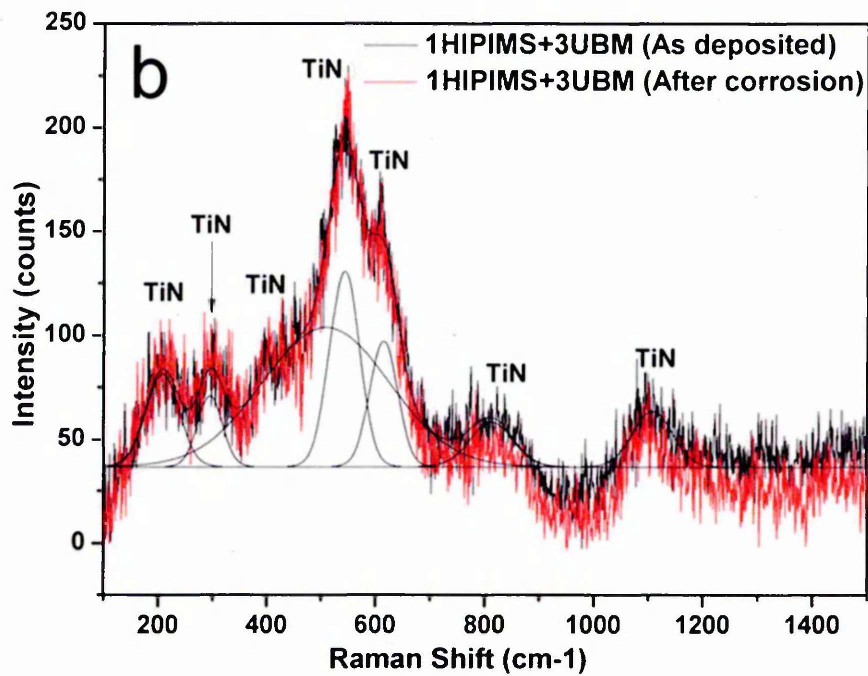

Figure 4.24 (b) Raman spectra of 1HIPIMS + 3UBM TiN coating

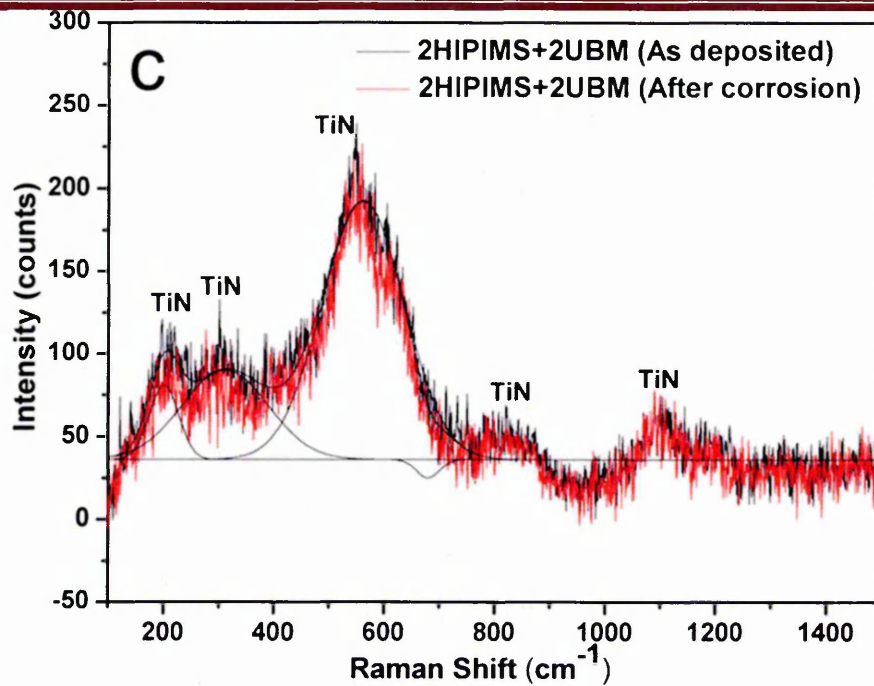

Figure 4.24 (c) Raman spectra of 2HIPIMS + 2UBM TiN coating

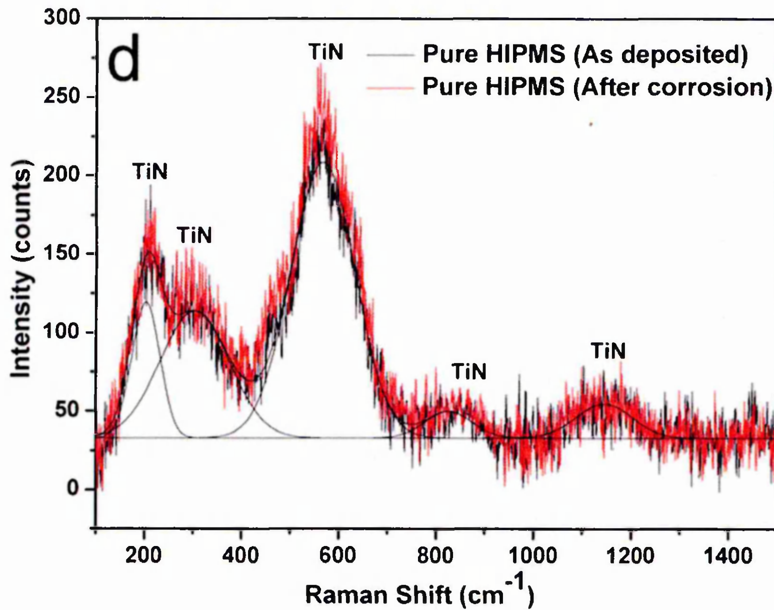

Figure 4.24 (d) Raman spectra of pure HIPIMS (2HIPIMS) TiN coating

Typical phonon bands of TiN were observed for all the as deposited coatings due to acoustic transitions in the 150-300 cm^{-1} region (LA and TA), optic modes in the 400-650 cm^{-1} region (LO and TO) and higher frequency spectral density via second - order transitions (A+O, 2O etc.). In the case of TiN coatings, scattering in the acoustic range is primarily determined by the vibrations of the Ti ions and in the optic range by vibrations of the N ions [17].

Table 4.8. Assignment of various Raman peaks of as-deposited and corroded TiN coatings deposited using different HIPIMS/UBM combination

	Peak Position (cm^{-1})	Peak Assignment
As deposited TiN	~ 200	TA/LA
(Pure UBM, 1HIPIMS + 3UBM,	~ 300	TA/LA
2HIPIMS + 2UBM, Pure	~ 410	2A
HIPIMS)	~ 550	TO/LO
	~ 610	TO/LO
	~ 800	A+O
	~ 1100	2O
Corroded pure UBM	~ 200	(TiN, Fe_2O_3)
	~ 300	TA/LA
	~ 410	(TiN, Fe_2O_3)
	~ 550	(TiN,Cr_2O_3)
	~ 800	(TiN, A+O)
	~ 1100	(TiN, 2O)
	~ 1310	(Fe_2O_3)
Corroded 1HIPIMS + 3UBM	same as as-deposited coating	
Corroded 2HIPIMS + 2UBM	same as as-deposited coating	
Corroded Pure HIPIMS	same as as-deposited coating	

For Pure UBM coating, the peak intensities are considerably increased after subjected to corrosion which could be due to the formation of a passive oxide layer and the corrosion products from the substrate. Similar increase in the intensity has been observed with thermally grown TiO_2 on TiN at different annealing temperatures [16]. Literatures suggest that Fe_2O_3 exhibits characteristic Raman peaks at ~ 200 , ~ 410 and ~ 1310 cm^{-1} and Cr_2O_3 has a peak at ~ 550 cm^{-1} [19 - 21]. However in this case it was not possible to differentiate them from TiN peaks as they overlap each other at the same position. Hence these peaks could be due to a mixture of TiN and the corrosion products. Moreover a new peak observed at ~ 1310 cm^{-1} is assigned to Fe_2O_3 due to the substrate corrosion [19]. Interestingly no peaks have been observed for TiO_2 and it has

been reported that a passive layer of TiO_2 is formed when TiN is polarised only at potential above +1 V with respect to a reference electrode [14, 15]. Raman spectra of as deposited and corroded TiN coating deposited by 1HIPIMS + 3UBM, 2HIPIMS + 2UBM and pure HIPIMS source combination exactly overlapped each other without any intensity change and without any peaks for corrosion products due to the substrate corrosion. In summary the pure UBM coating underwent intense corrosion as compared to the other three combinations as Raman study confirms the presence of corrosion products due to the substrate corrosion.

4.10.4 Transmission electron microscopy

The cross section TEM analysis has been done to understand the microstructure structure evolution of pure HIPIMS grown TiN coating [bias voltage: -50 V, coil current: 3 A and working pressure: 0.3 Pa]. Fig. 4.25 (a) shows the highly dense overall coating without any voids and pronounced column boundaries. This coating densification can be attributed to high energy ion irradiation which enhances adatom mobility during the initial nucleation of the films.

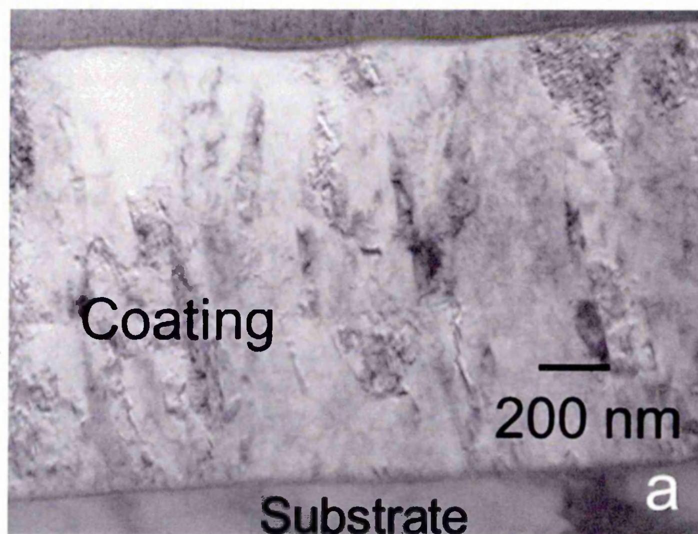

Figure 4.25 Cross-section TEM images of pure HIPIMS coating: (a) low magnification

Fig. 4.25 (b) shows high resolution image obtained from the top portion of the coating where the void free wider columns with flat column tops can be clearly seen

which is typical for nitride coatings subjected to high energy ion irradiation [22]. Moreover the grain renucleation is evident in the column boundaries (variation in the contrast) and is favoured when the growing film contains a high density of lattice defects. Similar results have been reported in the literature when TiN films were deposited in a laboratory scale HIPIMS sputtering machine [3].

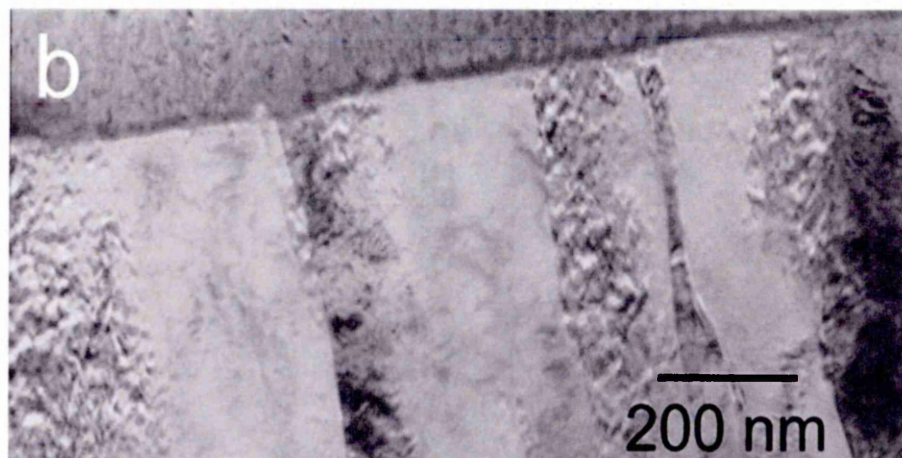

Figure 4.25 Cross-section TEM images of pure HIPIMS coating: (b) high magnification

4.11 Investigation of corrosion performance of TiN coatings deposited by arc evaporation and HIPIMS techniques

Thin film coatings deposited by cathodic arc evaporation method are embedded with macroparticles (droplets) which deteriorate the performance of the coatings such as corrosion resistance [23]. It has been reported that the droplets ejected from the cathode during arc evaporation undergo incomplete reaction with the reactive gas species en-route during the flight towards the substrate. Therefore, they are compositionally metal rich or N - deficient relative to the adjoining coating [23]. Furthermore, EDX measurements of TiN coatings embedded with droplets deposited by arc evaporation revealed that the core of the droplets was metal rich and the rim of droplets was nitrogen rich [24]. Thus, the droplet itself may be inhomogeneous in terms of its phase composition. Underneath each droplet, a voided region was observed.

In a droplet free coating, the pinhole defects present in the coating deteriorate the corrosion performance. A form of galvanic corrosion between the coating (cathode)

and substrate (anode) is created through the solution in the pinhole defects. On the other hand, a complicated corrosion mechanism was observed in the presence of droplets. Unlike droplet free coating, more than one galvanic couple was observed for coating with droplets since the droplets are compositionally nonhomogeneous. A detailed discussion of all of the corrosion mechanisms that determine the corrosion resistance of a coating with droplets can be seen in Ref. 23. In this work, the effect of metal- rich core of the droplets in corrosion of TiN coating deposited by arc evaporation is discussed in detail. The corrosion resistance of TiN coatings deposited by arc evaporation and HIPIMS technique is compared.

To better reveal the effect of metal- rich core of the droplets in corrosion of TiN coating, firstly, as-deposited TiN (arc) coating masked with bees wax to expose a surface area of 1 cm^2 was subjected to corrosion. Then the core of the droplets was deliberately exposed by gentle polishing of the as-deposited arc TiN coating. Subsequently, an un-corroded area of the polished coating was subjected to corrosion with previously corroded area masked with bees wax. Potentiodymanic polarisation was utilised (ACM instruments potentiostat, - 1 V to + 1 V) to study the corrosion behaviour of the coatings. Raman analysis was used to study the constituents of the corrosion product and to evaluate the corrosion damage. Scanning electron microscopy (SEM, planar view) was used to examine the as - deposited and corroded coating surfaces to define the morphological differences.

4.11.1 Potentiodynamic polarisation measurements of TiN coatings deposited using cathodic arc evaporation and 2HIPIMS + 2UBM source combination

Fig. 4.26 shows the Tafel plots obtained for Ti metal and TiN coatings deposited by cathodic arc evaporation and 2HIPIMS + 2UBM method. Table 4.9 summarizes the free corrosion potential (E_{corr}) obtained for Ti metal and TiN coatings deposited by arc evaporation and 2HIPIMS + 2UBM techniques. The E_{corr} values for as-deposited TiN

(arc) (-293.58 mV), polished TiN (arc) (-276.95 mV) and as-deposited TiN (2HIPIMS + 2UBM) (-286.34 mV) coatings were found to be slightly different from each other. A clear passive region was observed for all the three TiN coatings. Notably, the corrosion current density of as - deposited TiN (arc) coating was found to be lower than that of the polished TiN (arc) coating which confirms the better corrosion performance of the former. The corrosion current density of polished TiN (arc) coating was found to be the highest as compared to the other two coatings.

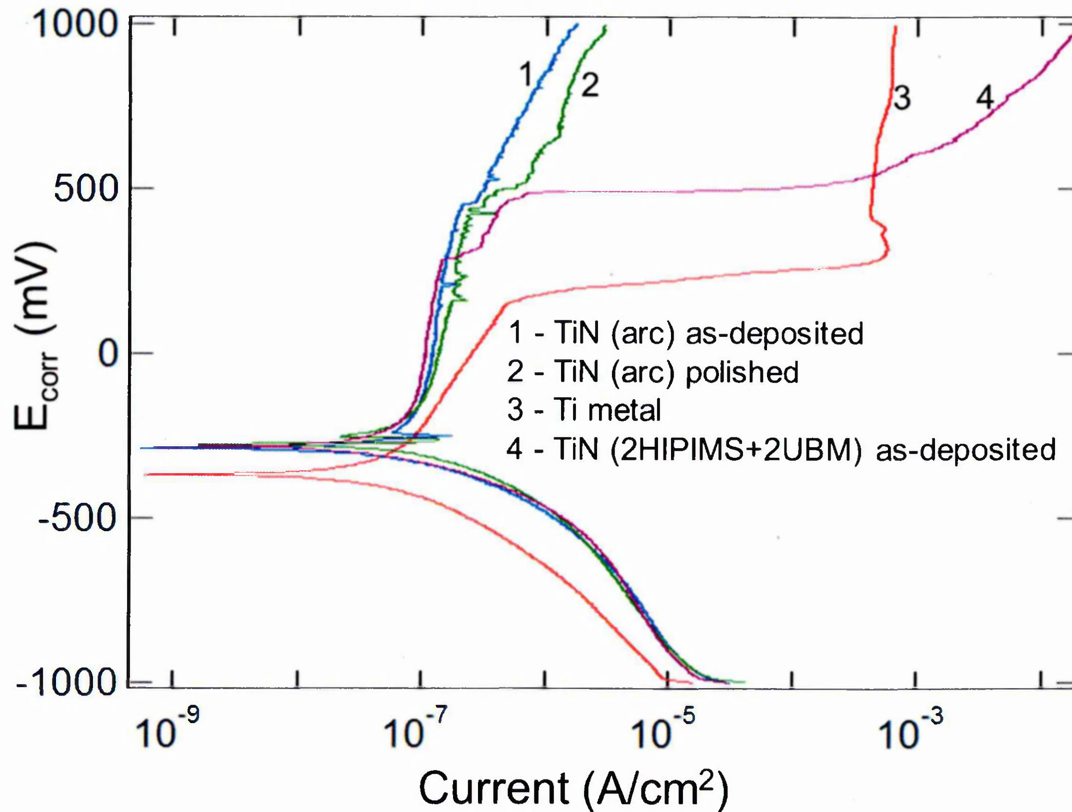

Figure 4.26 Potentiodynamic polarization curves of Ti metal and TiN coatings deposited by arc evaporation and combined HIPIMS/UBM techniques

The high corrosion current confirmed that the polished TiN (arc) coating corroded faster than the other two coatings. This could be attributed to the metal-rich droplet cores which were exposed after polishing. The metal rich core of the droplets, in this case Ti (anode) triggered the corrosion by forming a galvanic couple with the neighbouring TiN coating (cathode) along with the other corrosion mechanisms explained in Ref. 23. The corrosion in polished TiN (arc) coating initiates from the core

of the droplets since TiN coating is relatively inert to chemical attack as compared to Ti metal which is evident from the extremely low E_{corr} (~ 391.61 V) and high corrosion current of Ti metal.

Table 4.1 E_{corr} of Ti metal and TiN coatings deposited by arc evaporation and 2HIPIMS + 2UBM techniques

Source combination	E_{corr} (mV)
Ti metal	-391.61
TiN (arc) as-deposited	-293.58
TiN (arc) polished	-276.95
TiN (2HIPIMS + 2UBM) as-deposited	-286.34

The droplet free TiN coating deposited using 2HIPIMS + 2UBM source combination exhibited the lowest corrosion current density (Fig. 4.26) which confirms the superior corrosion resistance of such coating compared to the arc coatings (as-deposited & polished).

4.11.2 SEM analysis of TiN coatings deposited by arc evaporation method

Fig. 4.27 (a) shows the plan view SEM image of as-deposited TiN coating deposited by arc evaporation method. The droplets embedded in the coating can be clearly seen along with the small craters. The different contrast between the droplets and the neighbouring coating suggests their different chemical composition. In addition, the different contrast of each individual droplet suggests the variations in the compositions in the droplet itself [23]. The craters are believed to have appeared after the ejection of droplets embedded close to the film surface as a result of weak droplet-coating bonding due to the presence of voids beneath droplets [24].

Figure 4.27 (a) Plane view SEM image of as-deposited TiN (arc) coating

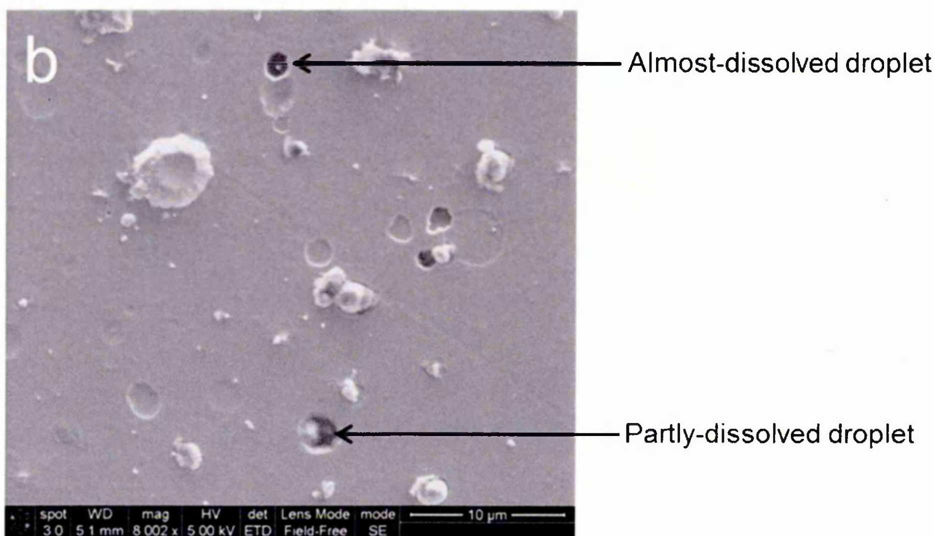

F Figure 4.27 (b) Plane view SEM images of corroded (unpolished) TiN (arc) coating

Fig. 4.27 (b) shows the plan view SEM image of corroded (unpolished) TiN coating deposited by arc evaporation. Some of the droplets were partly dissolved and few were almost dissolved due to the droplet corrosion. Interestingly, some the droplets were still completely intact and not affected by the corrosion. Each of the damaged droplets leaves a through-thickness hole or cavity as a consequence of the corrosion. This hole or cavity can be identified by different colour contrasts of such hole or cavity, the undamaged droplets and the neighbouring coating. The remains of a damaged droplet can be clearly seen in the high magnification image [Fig 4.27 (c)].

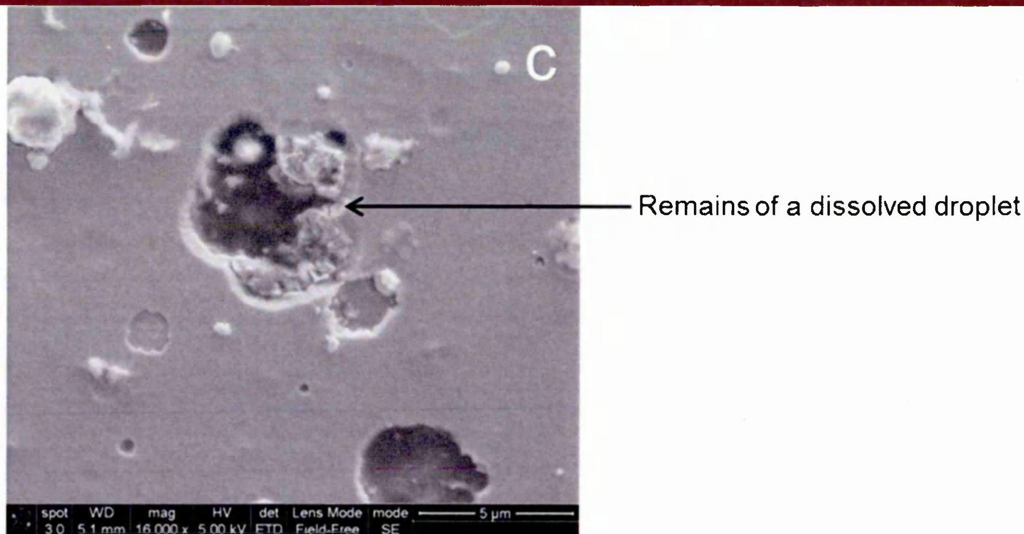

Figure 4.27 (c) Plane view SEM images of corroded (unpolished) TiN (arc) coating

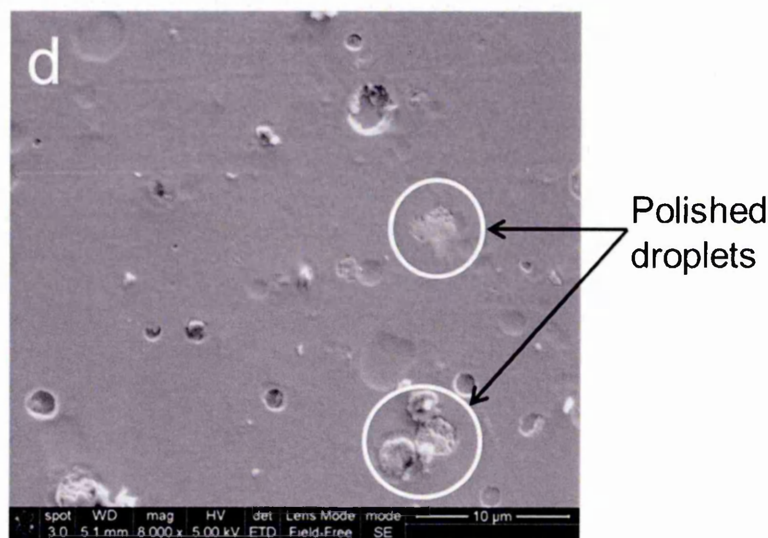

Figure 4.27 (d) Plane view SEM image of polished TiN (arc) coating (subjected to corrosion before polishing)

Fig. 4.27 (d) shows the plan view SEM image of polished (subjected to corrosion before polishing) TiN coating deposited by arc evaporation. It can be clearly seen that the droplets that were intact even after corrosion were either completely removed or cut during the polishing. The remains of partially-cut droplets (circled in white) confirm that the polishing effectively exposed the core of droplets. The partially-cut droplets due to the polishing exhibit a completely different contrast as compared to the corroded and un-corroded droplets.

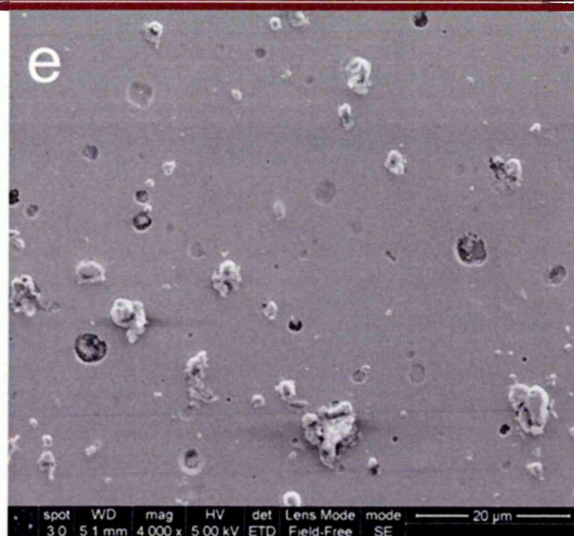

Figure 4.27 (e) Plane view SEM image of corroded TiN (arc) coating (polished before subjecting to corrosion)

The SEM image of corroded (polished) TiN coating [Fig. 4.27 (e)] also showed that the droplets were mainly affected by the corrosion. However, this observation using SEM couldn't be solely related to the polishing because even as-deposited droplets trigger corrosion. Nevertheless, these findings can be correlated with the potentiodynamic polarisation measurements.

4.11.3 Raman analysis of TiN coatings deposited by arc evaporation method and combined HIPIMS/UBM coating

Raman analysis has been done to demonstrate the effect of droplet corrosion in TiN coatings deposited by arc evaporation method. Fig. 4.28 shows the Raman spectra of TiN coating surface (as-deposited and corroded) and a droplet embedded in the coating (as-deposited and corroded). Characteristic phonon bands of TiN (Table 4.9) were observed for TiN as-deposited and corroded coating [Fig. 4.28 (a)]. A detailed description of the origin of these bands can be found in Sec. 4.10.3. Generally, TiN coatings are likely to form TiO_2 passive layer along with compounds such as oxynitrides when subjected to corrosion. In addition, compounds include oxides of Fe, Cr and Ni could be formed due to SS (substrate) corrosion (Sec. 4.10.3). No peaks due to the corrosion products were observed from corroded TiN coating surface. Therefore

it can be concluded from Fig. 4.28 (a) that the coating part remains unaffected by the corrosion.

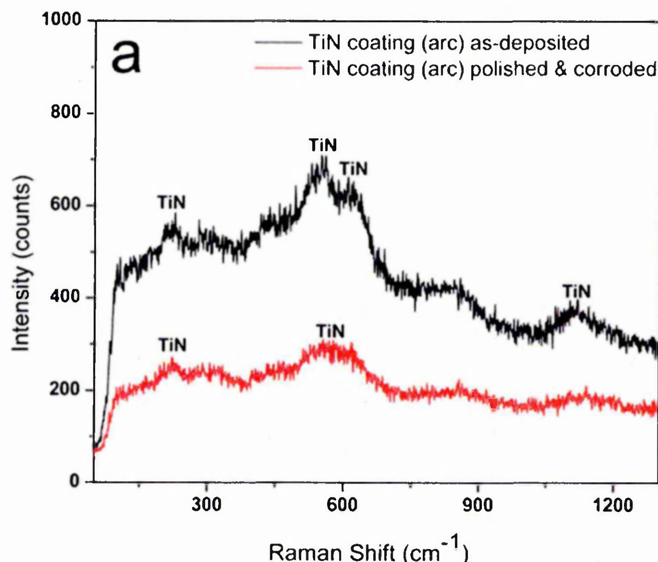

Figure 4.28 (a) Raman spectra of TiN coating (as-deposited and corroded) deposited by arc evaporation

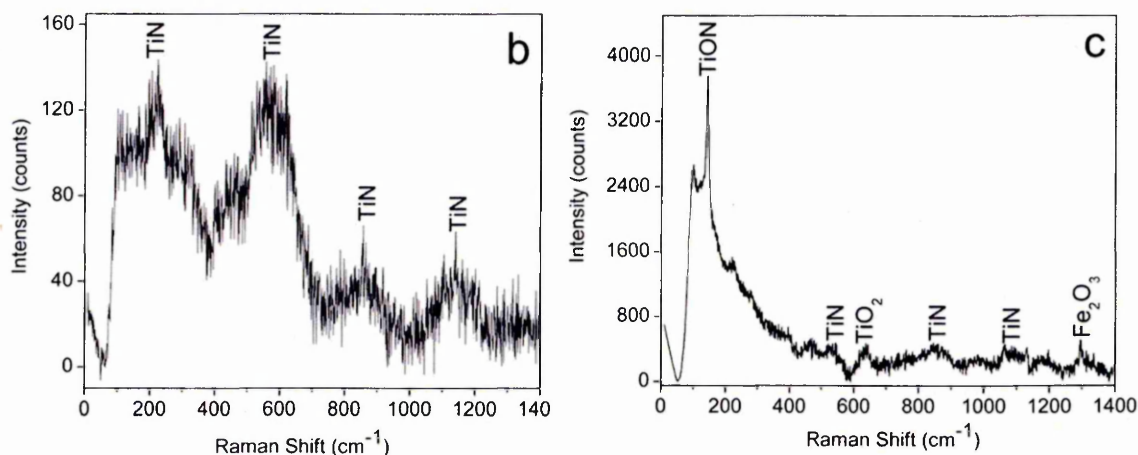

Figure 4.28 Raman spectra of a droplet embedded in TiN coating deposited by arc evaporation: (b) as-deposited; (c) corroded

For a droplet embedded in the as-deposited coating, typical phonon bands of TiN were observed. In contrast, the Raman spectra from a corroded droplet [Fig. 4.28 (b) & (c)] showed three new peaks around 150, 650 and 1300 cm^{-1}. These new peaks were assigned to the corrosion products such as TiON, TiO_2 and Fe_2O_3, respectively

[19, 25, 26]. These results illustrate that the droplets embedded in the coating were more susceptible to corrosion than the coating.

In summary, the potentiodynamic polarisation curves revealed the superior corrosion resistance of the 2HIPIMS + 2UBM grown TiN coating compared to the TiN (arc) coating (Fig. 4.26). In addition, Raman analysis of such coatings showed that the droplet free coating (2HIPIMS + 2UBM) was not affected by the corrosion [Fig. 4.26 (c)] and the droplets in TiN (arc) coating underwent aggressive corrosion. It can be concluded that the TiN coating produced by combined HIPIMS/UBM method showed superior corrosion resistant as compared to the coating produced by cathodic arc evaporation.

4.12 Summary of TiN coatings

OES measurements revealed that the ratio $\{Ti^{1+}\}:\{Ti^{0}\}$ was more than unity for 2HIPIMS + 2UBM (1.95) and pure HIPIMS (3.54) source combinations. The coil current, bias voltage and working pressure were 3 A, floating potential and 0.3 Pa, respectively for these measurements. This observation suggested that the highly active plasma can be generated by these combinations which could be useful for depositing good quality thin films coatings. In this case, the floating potential was measured to be approx. - 30 V. The ratio $\{Ti^{1+}\}:\{Ti^{0}\}$ for pure UBM (0.19) and 1HIPIMS + 3UBM (0.98) showed that these two combinations produced less metal ions as compared to the other two combinations. The ratio $\{Ti^{1+}\}:\{Ti^{0}\}$ increased with increasing coil current for all the source combinations. It was found that the structural density of the coatings increased with increasing degree of HIPIMS utilisation, bias voltage and coil current however with increased residual stress in the coatings. The excessive residual stress is undesirable for many applications as it causes coating delamination and stress induced corrosion. Therefore, TiN coatings deposited with increasing degree of HIPIMS utilisation at 3 A of coil current, - 50 V of bias voltage and 0.3 Pa of working pressure

has been considered for the further investigation. Pure UBM and 1HIPIMS + 3UBM TiN coatings exhibited rough columnar structure with intercolumnar voids which could be undesirable for many applications such as corrosion. However, 2HIPIMS + 2UBM and pure HIPIMS coatings were found to be highly dense without any voids which is one of the prerequisites for high corrosion resistance. The deposition rate of TiN coatings deposited using highly active plasma produced by 2HIPIMS + 2UBM and pure HIPIMS (2HIPIMS) source combinations were found to be 11.9 and 3.8 nm/min, respectively. The deposition rate of pure HIPIMS source combination is expected to increase up to 7.6 nm/min when four HIPIMS targets are used for the deposition. Metal ion (Ti^{1+}) etching by HIPIMS prior to the TiN coating deposition considerably increased the coating to substrate adhesion for all the four source combinations. Fig. 4.29 shows various coating characteristics as a function of source combination.

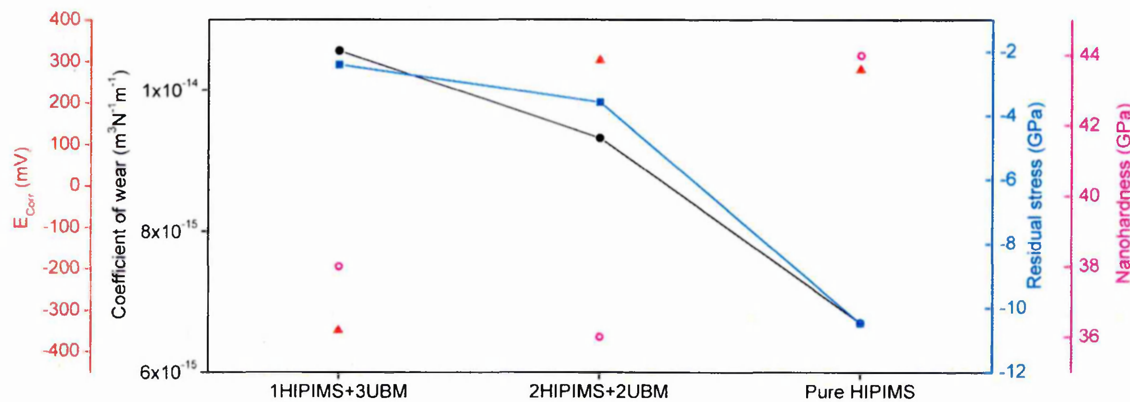

Fig. 4.29 Various coating characteristics as a function of source combination

The nanohardness of the coatings increased with increasing degree of HIPIMS utilisation. However, for 2HIPIMS + 2UBM source combination, it slightly decreased as compared to 1HIPIMS + 3UBM coating. The corrosion resistance of the coatings increased with increasing degree of HIPIMS utilisation as the E_{corr} values increased from - 391 mV to + 282 mV. The tribological properties improved with increasing degree of HIPIMS utilisation as the COW decreased from 1.145 x 10^{-14} $m^3N^{-1}m^{-1}$ to 6.705 x 10^{-15} $m^3N^{-1}m^{-1}$ and the COF decreased from 1.18 to 0.86 (not shown in

Fig. 4.29). These observations confirmed that thin film coatings can be deposited with enhanced mechanical, tribological and corrosion properties by increasing the degree of HIPIMS utilisation. However, the residual stress in TiN coatings also increased from - 2.394 GPa to -10.460 GPa with increasing degree of HIPIMS utilisation. Hence, it can be concluded that the 2HIPIMS + 2UBM source combination with coil current of 3 A, bias voltage of - 50 V and working pressure of 0.3 Pa appears to be the most advantageous in this research as it produces highly dense coatings with relatively low stress and enhanced coating properties at reasonably high deposition rates.

4.13 Characterisation of TiN/NbN multilayer coatings

4.13.1 Adhesion strength

Fig. 4.30 shows the optical images of indentations and scratch tracks of TiN/NbN multilayer coatings deposited utilising 1HIPIMS + 3UBM and 2HIPIMS + 2UBM source combinations. For all of the source combinations, no cracks, delamination and spallation of the coating were observed around the indents which showed the superior adhesion between the coating and the substrate. This excellent adhesion strength can be rated as grade HF1 according to the guidelines outlined by Ref. [2]. In addition, optical image of scratch track showed no coating failure such as spallation of the coating was observed up to 100 N load for 1HIPIMS + 3UBM and 2HIPIMS + 2UBM grown coatings. These results clearly showed the excellent adhesion strength between the coating and substrate. This behaviour is attributed well-defined crystal structure at the coating-substrate interface provided by HIPIMS metal ion etching.

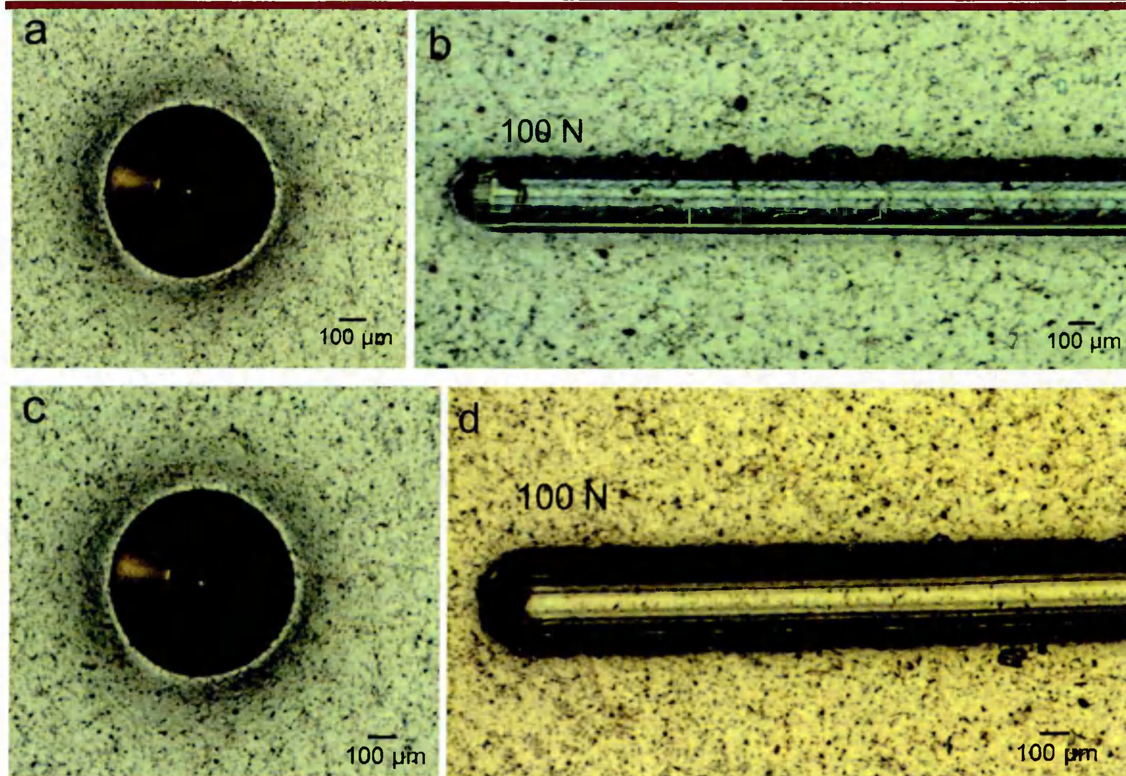

Figure 4.30 Optical images of Rockwell indentations and scratch tracks: (a, b) 1HIPIMS + 3UBM; (c, d) 2HIPIMS + 2UBM

4.13.2 X-ray diffraction analysis

Fig. 4.31 shows BB and GA XRD patterns of 1HIPIMS + 3UBM and 2HIPIMS + 2UBM grown TiN/NbN multilayer coatings. Both the BB and GA XRD patterns exhibited a high intensity peak centred at 2θ = 40.97° and it is assigned to NbN (200). Other high angle reflections for NbN such as (200), (311), (222) and (331) for TiN were very weak in BB XRD pattern, indicating that majority of the NbN grains were oriented along (200). However, some of the high angle reflections were prominent in GA XRD pattern.

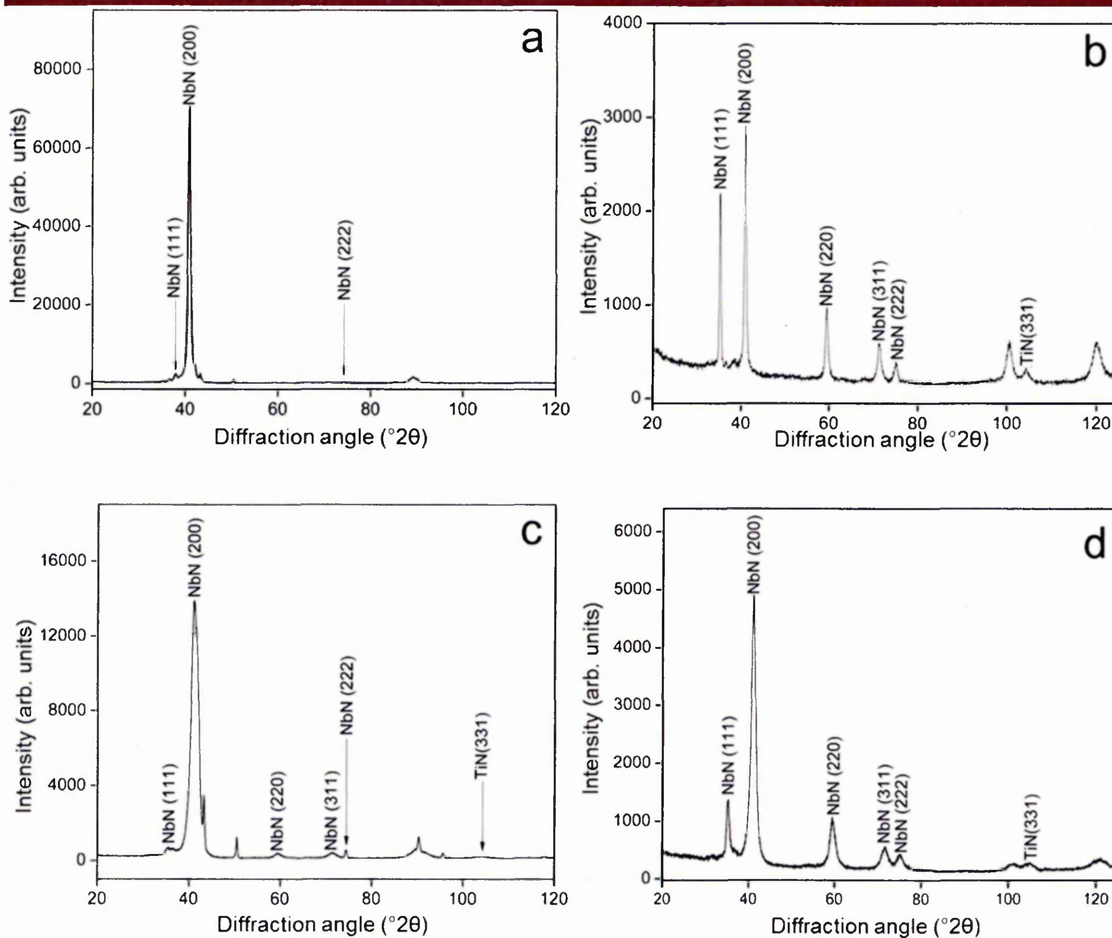

Figure 4.31 BB and GA XRD patterns of TiN/NbN multilayer coatings: (a & b) 1HIPIMS + 3UBM; (c & d) 2HIPIMS + 2UBM

4.13.3 Bilayer thickness

The bilayer thickness of the 1HIPIMS + 3UBM and 2HIPIMS + 2UBM grown TiN/NbN multilayer coatings was calculated using low angle XRD patterns shown in Fig. 4.32. For the same deposition conditions, the bilayer thickness of the 1HIPIMS + 3UBM and 2HIPIMS + 2UBM grown coatings was 3.54 and 2.33 nm, respectively. The bilayer thickness of 1HIPIMS + 3UBM grown coating was ~ 34% higher than that of the 2HIPIMS + 2UBM grown coating. The thickness reduction is attributed to the low sputtering rate due to the increased number of HIPIMS targets utilised for 2HIPIMS + 2UBM process.

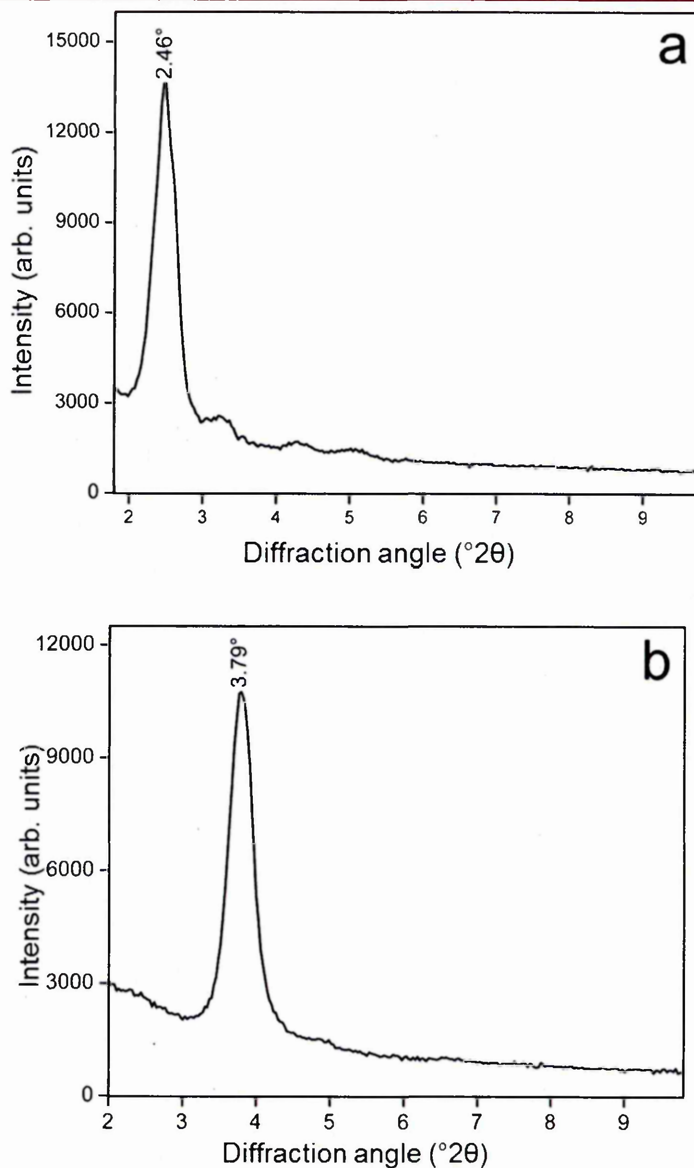

Figure 4.32 Low angle XRD patterns of TiN/NbN multilayer coatings:
(a) 1HIPIMS + 3UBM, (b) 2HIPIMS + 2UBM

4.13.4 Energy dispersive X-ray spectroscopy analysis

EDX analysis was carried out to analyse the elemental composition of 1HIPIMS + 3UBM grown TiN/NbN multilayer coatings. The EDX spectrum (Fig. 4.33) clearly showed well defined peaks of Ti, Nb and N. The percent composition of Ti, Nb and N in TiN/NbN multilayer coating was found to be 9.1, 40.46 and 40.43 at. %, respectively.

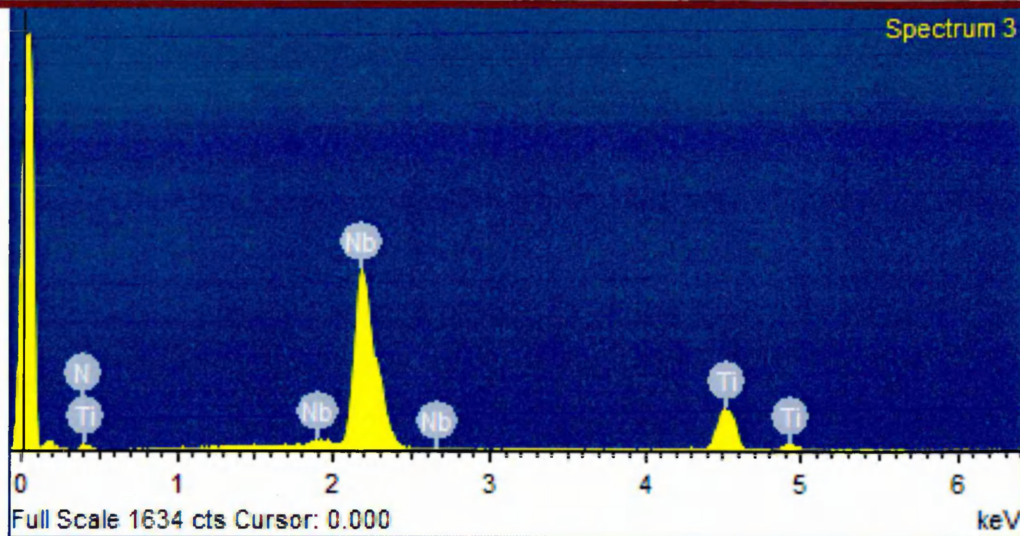

Figure 4.33 EDX spectra of 1HIPIMS + 3UBM grown TiN/NbN coating

4.13.5 Microstructure analysis

Fig. 4.34 depicts the SEM cross-section images of TiN/NbN coating deposited with 2HIPIMS + 2UBM source combination. The microstructure was columnar and the column tops were relatively smoother and wider without any voided region along the column boundaries. This type of microstructure can be attributed to the enhancement in the adatom mobility due to the relatively high ion to neutral ratio with sufficient energy by two HIPIMS sources involved in the process.

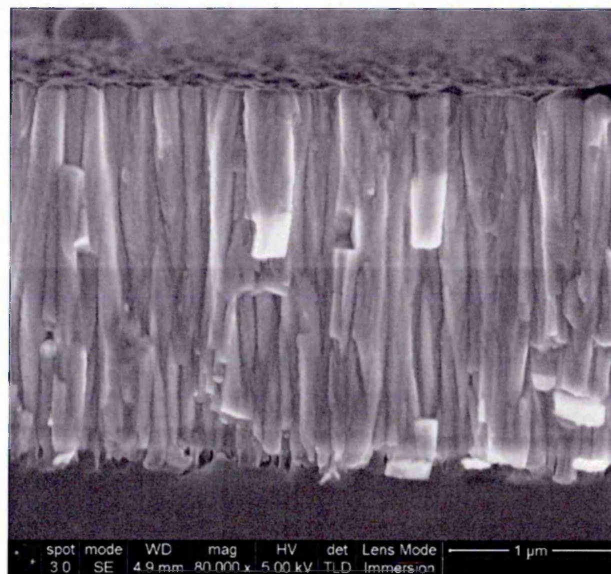

Figure 4.34 Cross-section SEM image of 2HIPIMS + 2UBM grown TiN/NbN multilayer coating

4.13.6 Mechanical and tribological properties

4.13.6.1 Nano-hardness test

The applied load for the nanoindentation test was 10 mN. The hardness of TiN/NbN multilayer coatings grown by 2HIPIMS + 2UBM process was found to be increased with increasing degree of HIPIMS utilisation as observed in TiN coatings. It increased from 27 GPa for 1HIPIMS + 3UBM to 30 GPa for 2HIIPIMS + 2UBM. The hardness enhancement is attributed to the microstructure densification and increased stress as discussed in Sec. 4.5.1.

4.13.6.2 Coefficient of friction and wear coefficient

Fig. 4.35 depicts the COF curves of different TiN/NbN coatings as a function of number of laps in dry sliding wear conditions. Both 1HIPIMS + 3UBM and 2HIPIMS + 2UBM coatings exhibited a COF (μ) of about 1.

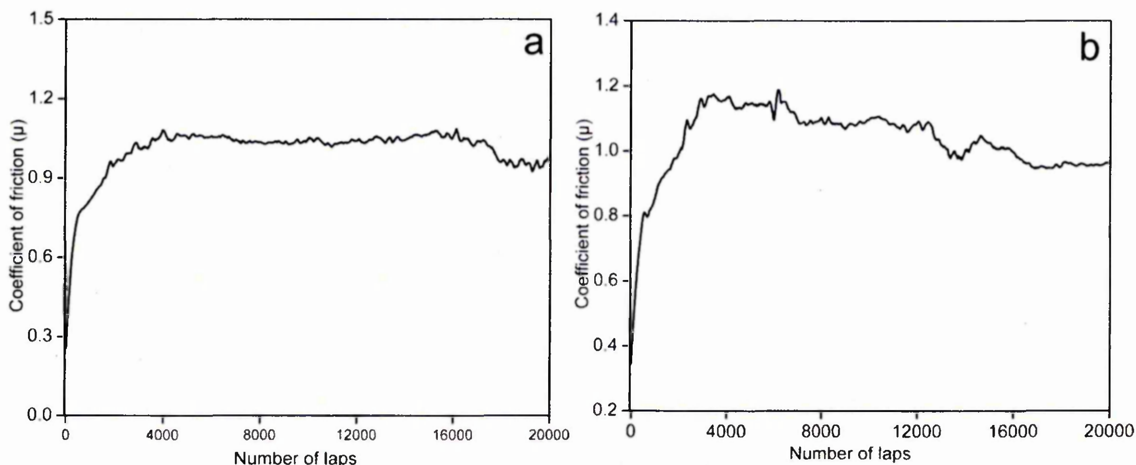

Figure 4.35 Coefficient of friction curves of TiN/NbN multilayer coatings: (a) 1HIPIMS + 3UBM; (b) 2HIPIMS + 2UBM

The wear profiles measured by the Dektak surface profiler after the tribology test are shown in Fig. 4.36. The COW values of multilayer TiN/NbN coatings decreased with increasing degree of HIPIMS utilisation. The COW of 1HIPIMS + 3UBM and 2HIPIMS + 2UBM grown TiN/NbN coatings was 1.08×10^{-14} and 9.09×10^{-15} $m^3N^{-1}m^{-1}$, respectively. The COW of 2HIPIMS + 2UBM deposited coating is one order of magnitude higher than that of the 1HIPIMS + 3UBM coating. This is

attributed to the layer by layer wear mechanism of the nano scale multilayer structure comprising a number of interfaces parallel to the surface and the sliding direction which has the effect of deflecting cracks initiated during the sliding process [4].

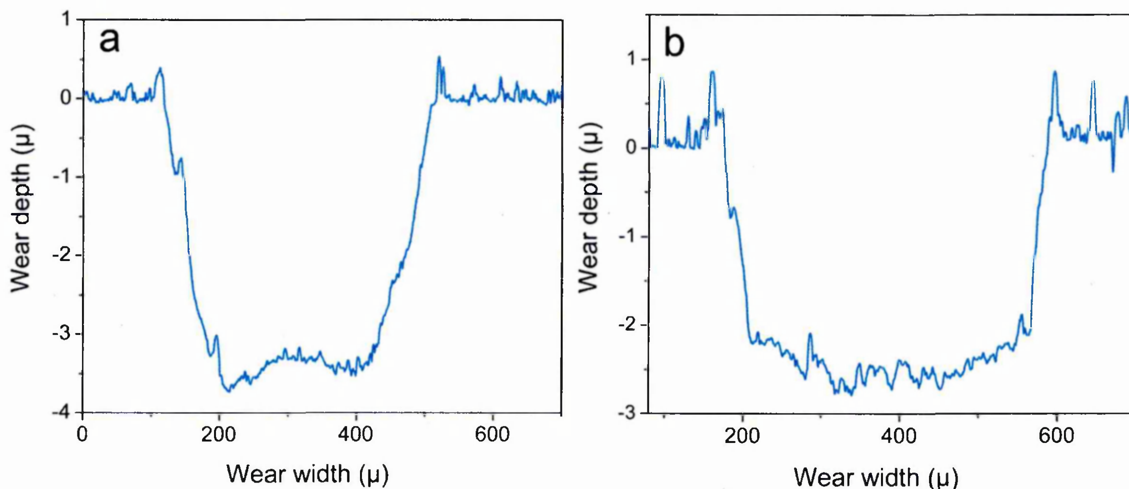

Figure 4.36 Wear depth and width profile of TiN/NbN multilayer coatings slid against Al_2O_3 ball (diameter of 6mm): (a) 1HIPIMS + 3UBM; (b) 2HIPIMS + 2UBM

4.13.7 Corrosion properties

The potentiodynamic polarization curves of the CoCr substrate and TiN/NbN multilayer coatings in 3.5% NaCl solution are presented in Fig. 4.37.

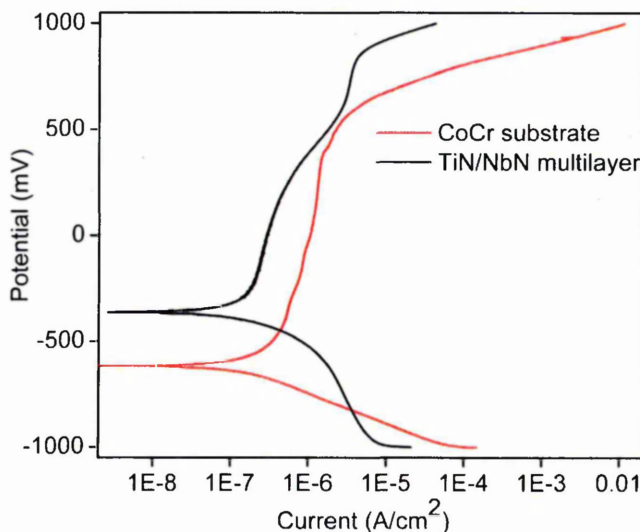

Figure 4.37 Potentiodynamic polarization curves of CoCr substrate and TiN/NbN multilayer (1HIPIMS + 3UBM) coating

The E_{corr} value for CoCr was about - 530 mV. The E_{corr} value for the multilayer coating was located in the nobler region than the substrate; about - 365 mV. It can be

clearly seen that the multilayer coating and the substrate showed passivation over a wide potential range. However, the thin film showed a wider passive region as compared to the substrate. In addition to a wider passive region the thin film showed a lower passive current. The high E_{corr}, wider passive region and lower corrosion currents demonstrated the excellent corrosion resistance of the TiN/NbN multilayer coatings. This performance is attributed to the several interfaces that present in the multilayers which act as barriers for corrosive ions to diffuse through the coating and reach the substrate. In addition, the diffusion of ions towards the substrate is inhibited due to the reduced number of pores present in the high dense coating due to HIPIMS. Better corrosion properties are expected with TiN/NbN (2HIPIMS + 2UBM) coating than the above discussed TiN/NbN (1HIPIMS + 3UBM) coating.

4.14 Characterisation of TiCN/NbCN multilayer coatings

4.14.1 X-ray diffraction analysis

Fig. 4.38 shows BB and GA XRD patterns of 1HIPIMS + 3UBM grown TiCN/NbCN multilayer coatings. The BB XRD pattern exhibited a high intensity peak centred at $2\theta = 42.3°$ and it is assigned to $Nb_xTi_xN_xC_x$ (200). Other reflections such as (111) and (220) were very weak, indicating that majority of the grains were oriented along (200). However, in GA XRD pattern the peak intensities for (111) and (200) reflections are almost same and prominent peaks were observed for other high angle reflections such as (220) and (311) also.

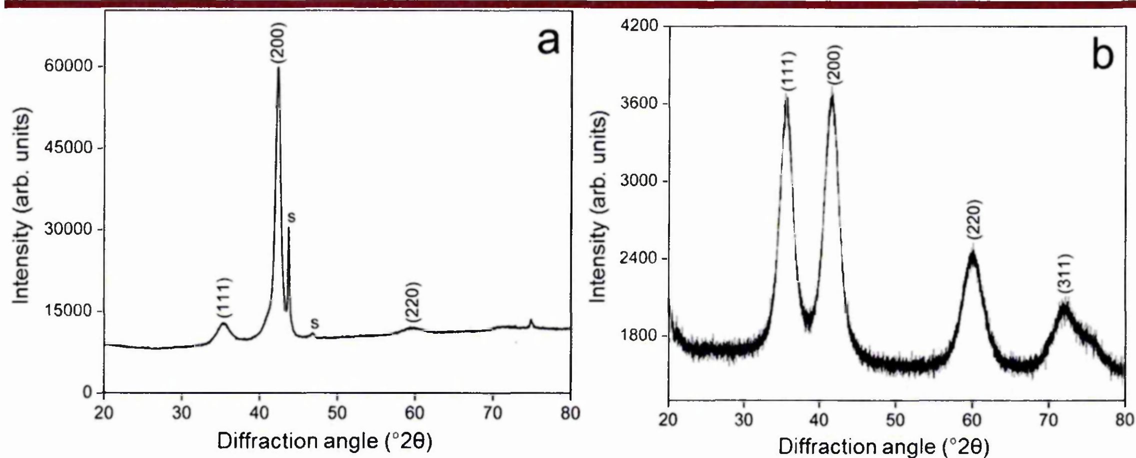

Figure 4.38 XRD patterns of TiCN/NbCN (1HIPIMS + 3UBM) multilayer coating: (a) BB geometry; (b) GA geometry

4.14.2 Bilayer thickness

The bilayer thickness of the TiCN/NbCN multilayer coating was calculated using low angle XRD pattern shown in Fig. 4.39. The calculated bilayer thickness of the coating was 3.72 nm.

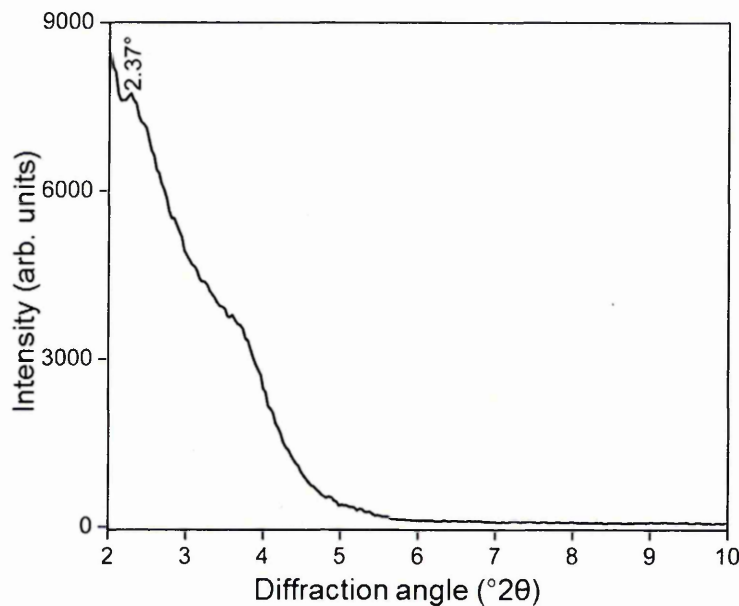

Figure 4.39 Low angle XRD pattern of TiCN/NbCN (1HIPIMS + 3UBM) multilayer coating

4.14.3 Energy dispersive X-ray spectroscopy analysis

EDX analysis was done to study the elemental composition of the TiCN/NbCN coatings. The EDX spectrum (Fig. 4.40) showed well defined peaks of Ti, Nb, N and C.

The percent composition of Ti, Nb, N and C in TiCN/NbCN multilayer coating was found to be 10.1, 19.12, 37.75 and 38.13 at. %.

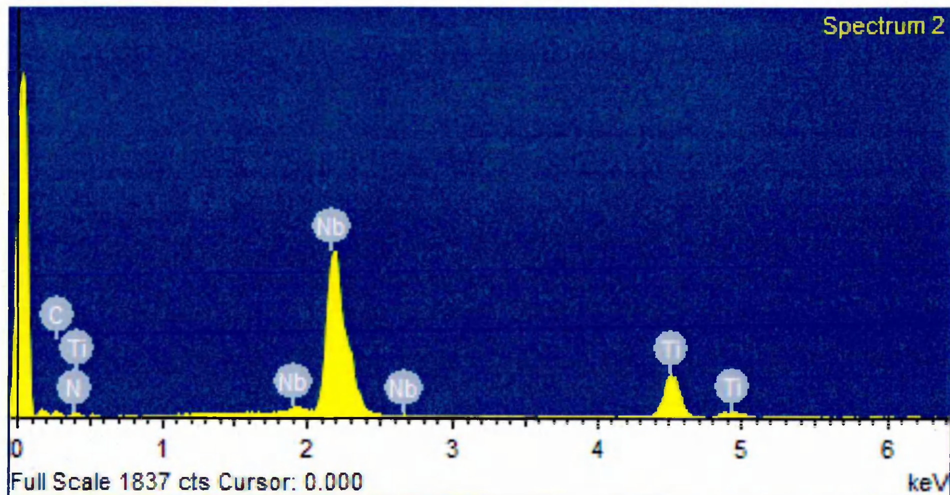

Figure 4.40 EDX spectra of TiCN/NbCN (1HIPIMS + 3UBM) multilayer coating

4.14.4 Mechanical and tribological properties

4.14.4.1 Nanohardness test

The applied load for the nanoindentation test was 10 mN. The nano hardness of CoCr substrate and TiCN/NbCN multilayer coating was 15 GPa and 28 GP, respectively. The Young's modulus of the substrate and TiCN/NbCN multilayer coating was 385 GPa and 357 GPa. The hardness of the multilayer coating was found to be a factor of about 1.9 higher than that of the CoCr substrate.

4.14.4.2 Coefficient of friction and wear coefficient

Fig. 4.41 shows friction curve of 1HIPIMS + 3UBM grown TiCN/NbCN multilayer coating as a function of number of laps in dry sliding wear conditions. The COF of CoCr substrate and TiCN/NbCN multilayer coating is given in Table 4.10. The average COF value of CoCr substrate and the multilayer coating was 0.69 and 0.43 respectively. It was very clear the from the COF values that the multilayer coating exhibited better COF than CoCr substrate. The low COF of TiCN/NbCN multilayer coating is attributed to the presence of carbon in the coating which produces a thin film

of solid lubricant during sliding which in turn contributes to a considerable reduction in the friction coefficient values [27].

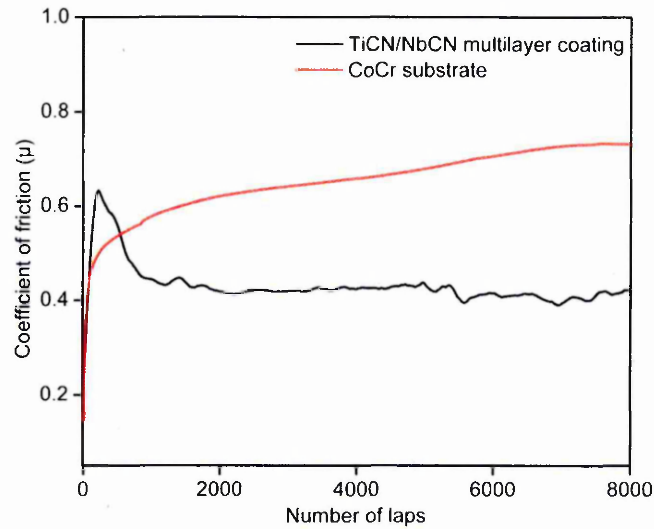

Figure 4.41 COF curves of CoCr substrate and TiCN/NbCN (1HIPIMS + 3UBM) multilayer coating

Table 4.20 COF of CoCr substrate and TiCN/NbCN multilayer coating

Material	Minimum COF (μ)	Mean COF (μ)	Maximum COF (μ)
CoCr	0.14	0.69	0.99
TiCN/NbCN multilayer coating	0.19	0.43	0.63

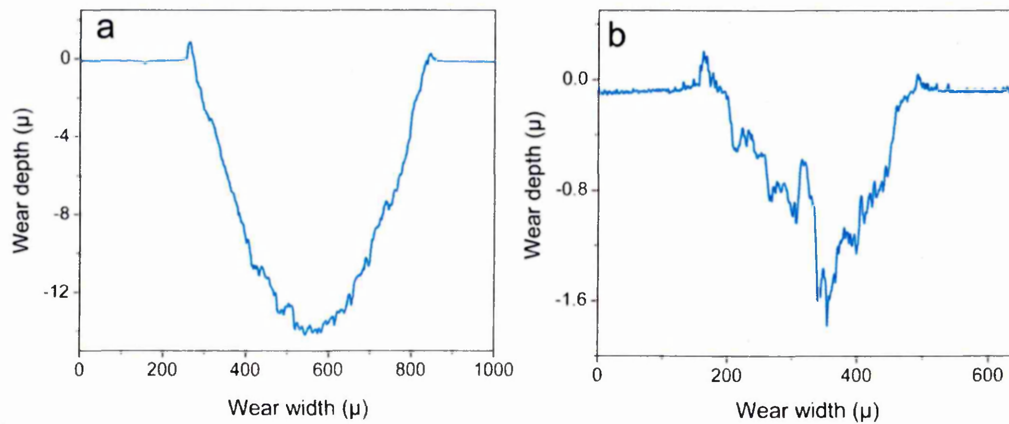

Figure 4.42 Wear depth and width profile (a) CoCr substrate; (b) 1HIPIMS + 3UBM grown TiCN/NbCN multilayer coating

The wear profiles of CoCr substrate and TiCN/NbCN multilayer coatings measured by the Dektak surface profiler after the pin on disc tribology test are shown in Fig. 4.42. The calculated COW of CoCr substrate and the TiCN/NbCN multilayer coating was found to be 1.00×10^{-13} and 3.57×10^{-15} $m^3N^{-1}m^{-1}$, respectively. The dry sliding COW of CoCr substrate was about two orders of magnitude higher than that of the COW of the multilayer coating. The lower COF and COW values of the multilayer coating demonstrated the superior tribological properties of such coating against the CoCr substrate. This performance is attributed to the special structure of the coating where carbon is segregated to form a low shear strength lateral phase promoting layer by layer wear mechanism on a nanoscale [28].

4.14.5 Corrosion properties

The potentiodynamic polarization curves of the CoCr substrate and 1HIPIMS + 3UBM grown TiCN/NbCN multilayer coating in 3.5% NaCl solution are shown in Fig. 4.43.

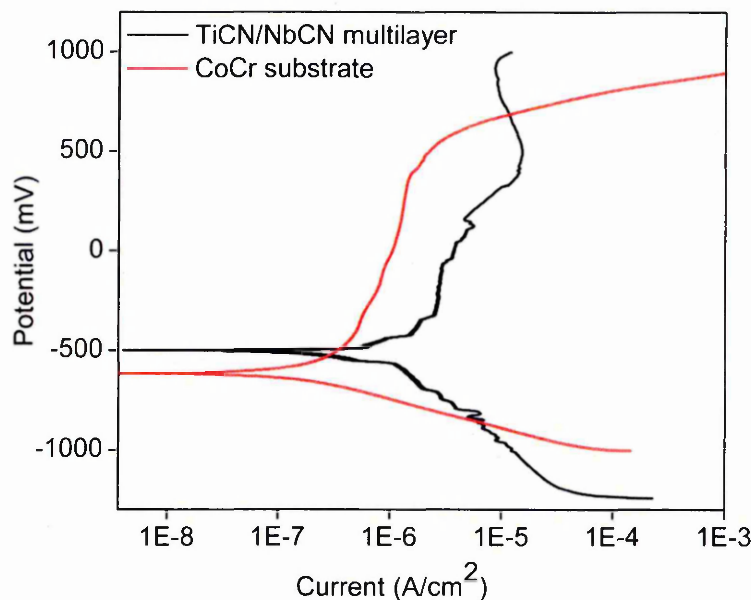

Figure 4.43 Potentiodynamic polarization curves of CoCr substrate and TiCN/NbCN (1HIPIMS + 3UBM) multilayer coating

The E_{corr} value for CoCr was about - 530 mV. The E_{corr} value for the multilayer coating was located in the nobler region than the substrate; about - 500 mV which

revealed the enhanced corrosion performance of the coating. In addition, the multilayer coating and the substrate showed passivation over a wide potential range. The passivation current density for the CoCr substrate was found to be low as compared to the coating. However, the corrosion current density value for the substrate was found to be increased rapidly over 600 mV. In contrast, the corrosion current density of the coating was almost constant. This observation along with the enhanced E_{corr} value demonstrated the improved corrosion behaviour of the coating than the underlying substrate. Note that, the corrosion resistance of this coating maybe further enhanced by increasing the degree of HIPIMS utilisation [2HIPIMS + 2UBM] as discussed in Sec. 4.10.

4.15 Characterisation of CrN/NbN multilayer coatings

4.15.1 Adhesion strength

Fig. 4.44 shows the optical images of indentation and scratch track of CrN/NbN multilayer coating deposited utilising 2HIPIMS + 2UBM source combination.

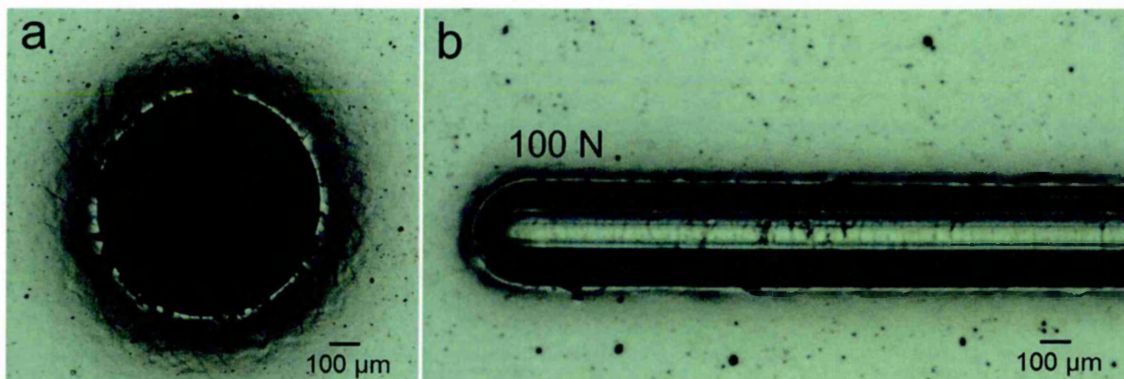

Figure 4.44 Optical images of Rockwell indentations and scratch tracks: 2HIPIMS + 2UBM grown CrN/NbN coating

No cracks, delamination and spallation of the coating were observed around the indent which showed the superior adhesion between the coating and the substrate. The adhesion strength of this coating can be rated as grade HF1 according to the guidelines outlined in Ref. [2]. In addition, optical image of scratch track showed no coating failure such as spallation of the coating was observed up to 100 N load. These results

confirmed the excellent adhesion strength between the coating and substrate due to HIPIMS.

4.15.2 X-ray diffraction analysis

4.15.2.1 Bragg Brentano and glancing angle

Fig. 4.45 shows BB and GA XRD patterns of 2HIPIMS + 2UBM grown CrN/NbN multilayer coatings.

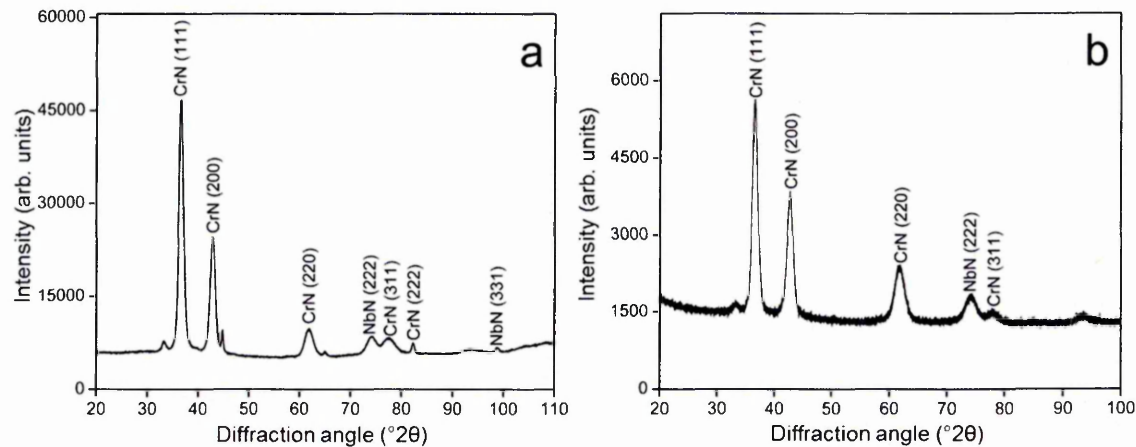

Figure 4.45 (a-b) BB and GA XRD patterns of 2HIPIMS + 2UBM grown CrN/NbN multilayer coating

Both the BB and GA XRD patterns exhibited a high intensity peak centred at $2\theta = 36.55°$ and it is assigned to CrN (111). Other high angle reflections for CrN such as (200), (220), (311), (222) and (222) and (331) for NbN were very weak in BB XRD pattern, indicating that majority of the CrN grains were oriented along (111). However, some of the high angle reflections were prominent in GA XRD pattern.

4.15.2.2 Bilayer thickness

The bilayer thickness of the CrN/NbN multilayer coating was calculated using low angle XRD patterns shown in Fig. 4.46. The calculated bilayer thickness of the coating was 2.99 nm.

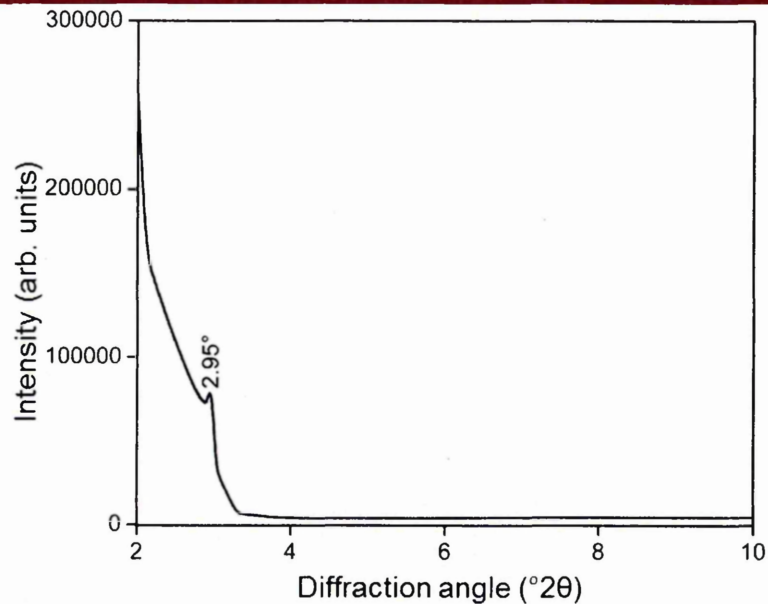

Figure 4.46 Low angle XRD pattern of CrN/NbN multilayer coating deposited using 2HIPIMS + 2UBM source combination

4.15.3 Energy dispersive X-ray spectroscopy analysis

EDX analysis was done to study the elemental composition of the CrN/NbN coatings. The EDX spectrum (Fig. 4.47) exhibited well defined peaks of Cr, Nb and N_2. The percent composition of Cr, Nb and N and C in CrN/NbN multilayer coating was found to be 35.32, 13.83 and 50.85 at. %, respectively.

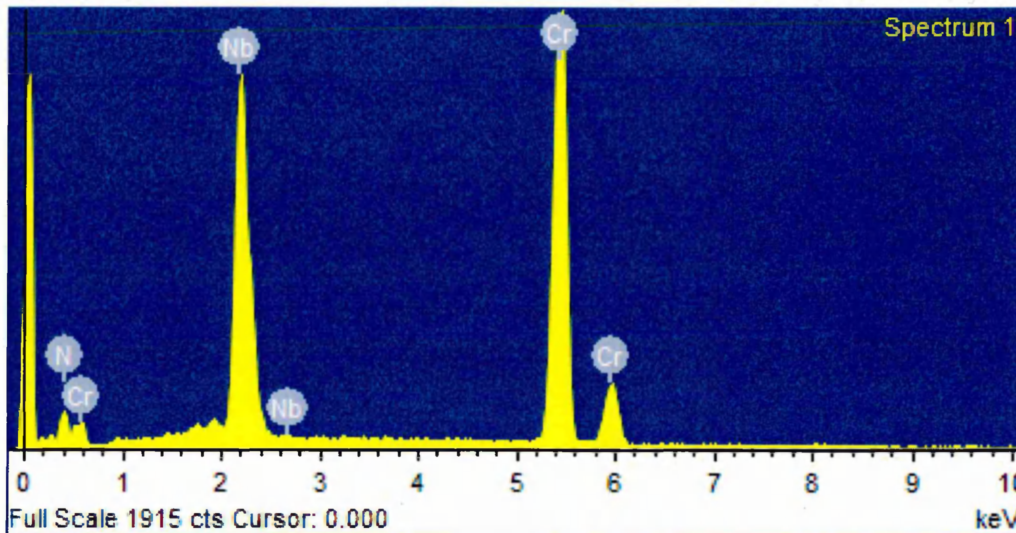

Figure 4.47 EDX spectra of 2HIPIMS + 2UBM grown CrN/NbN coating

4.15.4 Microstructure analysis

Fig. 4.48 depicts the SEM cross-section images of CrN/NbN coating deposited with 2HIPIMS + 2UBM source combination. The microstructure was columnar and the column tops were relatively smoother and wider without any voided region along the column boundaries. This type of microstructure can be attributed to the enhancement in the adatom mobility due to the relatively high ion to neutral ratio with sufficient energy by two HIPIMS sources involved in the process.

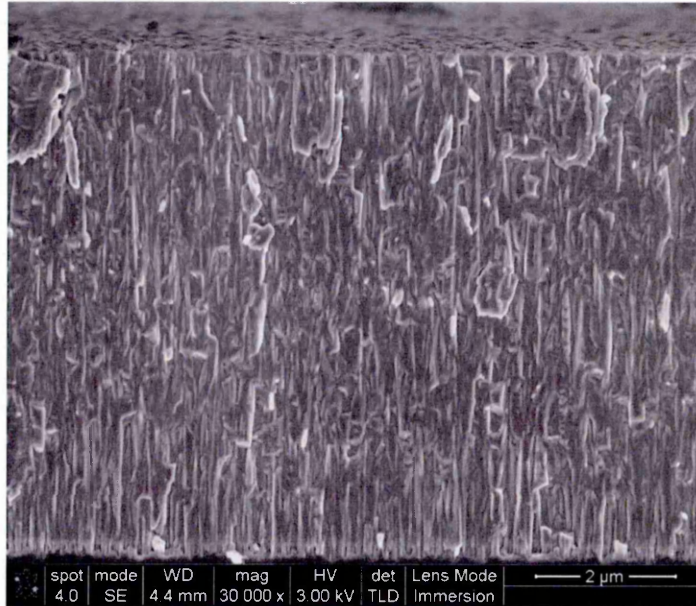

Figure 4.48 Cross-section SEM image of 2HIPIMS + 2UBM grown CrN/NbN multilayer coating

4.15.5 Investigation of thickness distribution across the sample holder

CrN/NbN multilayer coating was deposited on silicon wafers at different heights to study the thickness distribution across the sample holder. The coated samples were fractured and used for the thickness measurements by utilizing scanning electron microscopy. Fig. 4.49 shows the silicon samples kept at different heights across the sample holder in the chamber. One of the targets is also shown to demonstrate the relative height of the silicon samples to the target.

The 2HIPIMS + 2UBM source combination was used for the deposition. The deposition time was 4.5 hours for this experiment. The thickness values are listed in Table 4.11. The sample which was kept at position 2 exhibited the maximum thickness of 6.9 μm. The sample at position 3 showed a thickness value of 6.02 μm which is only about 13% less than the thickness of the sample at position 2.

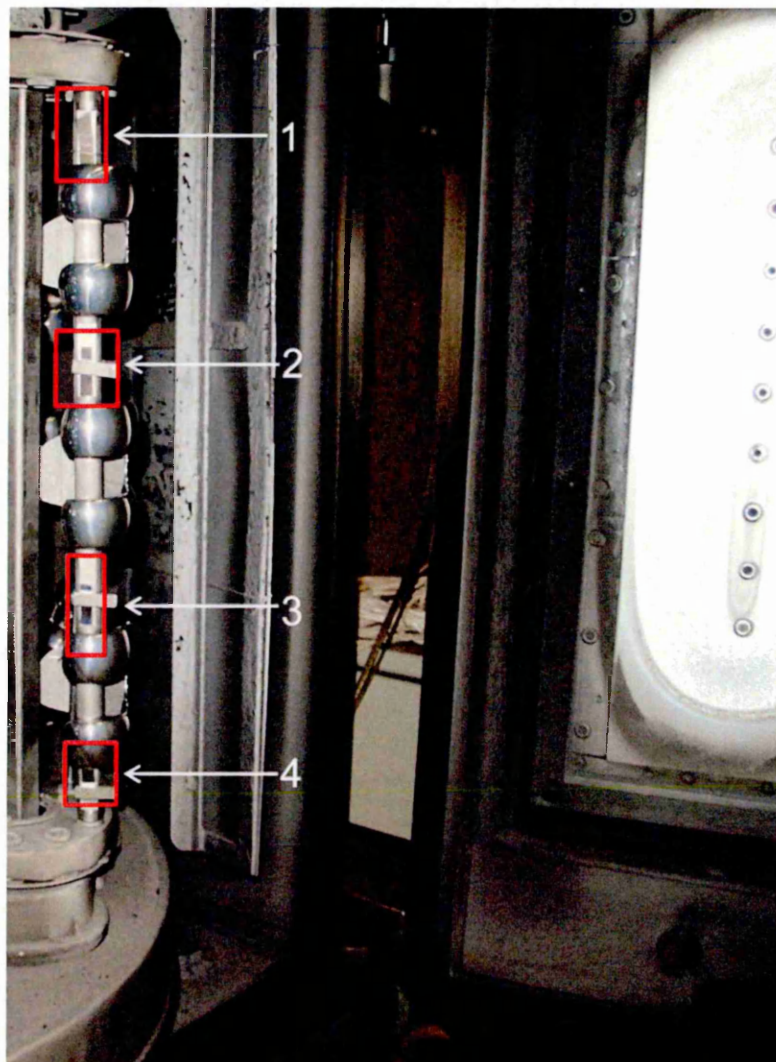

Figure 4.49 Silicon samples at different heights to study the thickness distribution across the sample holder

These results demonstrated that thin film coatings with near-uniform thickness can be deposited by keeping the sample at position 2 and 3. The thickness of the samples which were kept at position 1 (5.43 μm) and 4 (4.32 μm) is about 21% and 37% less compared to the thickness of the sample at position 2.

Table 4.3. Thickness of the CrN/NbN coating deposited on silicon substrates which were kept at different height across the sample holder

Sample position	Thickness (μm)
1	5.43
2	6.90
3	6.02
4	4.32

4.15.6 Mechanical and tribological properties

4.15.6.1 Nano-hardness test

The applied load for the nanoindentation was 10 mN. The nano hardness and Young's modulus of CrN/NbN multilayer coating was 40 GPa and 551 GPa, respectively. These values found to be higher than that of the same coating grown utilising 1HIPIMS + 3UBM source combination [29]. This observation is attributed to the densification of coating microstructure and the increased residual stress with increasing degree of HIPIMS utilisation as explained in Sec. 4.5.1.

4.15.6.2 Coefficient of friction and wear coefficient

Fig. 4.50 shows friction curve of 2HIPIMS + 2UBM grown CrN/NbN multilayer coating as a function of number of laps in dry sliding wear conditions. The COF values of the coating are given in Table 4.12.

Table 4.12 Coefficient of friction of CrN/NbN multilayer coating

Material	Minimum COF (μ)	Mean COF (μ)	Maximum COF (μ)
CrN/NbN multilayer coating	0.24	0.49	0.75

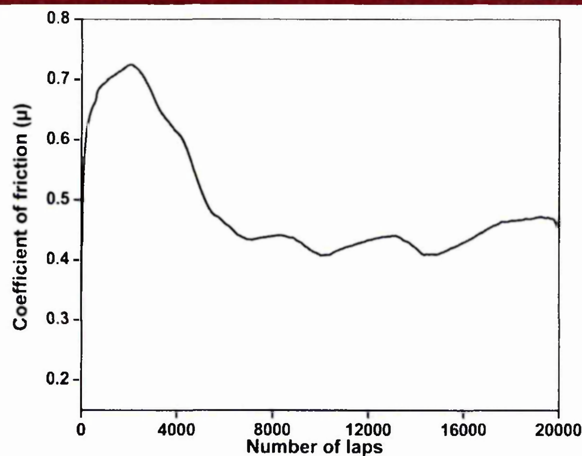

Figure 4.50 Coefficient of friction curve of 2HIPIMS + 2UBM grown CrN/NbN multilayer coating

The average COF of CrN/NbN multilayer coating was 0. 49. The wear profile of CrN/NbN multilayer coating measured by the Dektak surface profiler is shown in Fig. 4.51. The measured wear depth of the coating was found to be ~ 0.8 μm. The calculated COW of the coating was 8.33×10^{-16} $m^3N^{-1}m^{-1}$. This COW value is one order of magnitude lower as compared to the same coating grown utilising 1HIPIMS + 3UBM source combination [29].

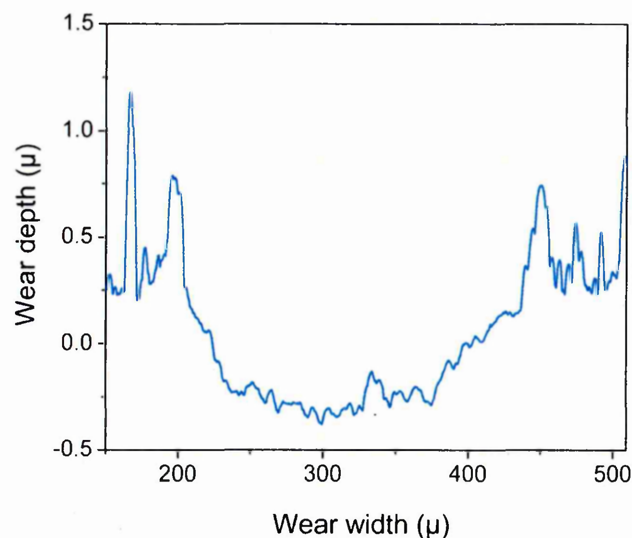

Figure 4.51 Wear depth and width profile of CrN/NbN multilayer coating slid against Al_2O_3 ball (diameter of 6mm)

4.15.7 Corrosion properties

The potentiodynamic polarization curves of the CoCr substrate and CrN/NbN multilayer coatings in 3.5% NaCl solution are presented in Fig. 4.52.

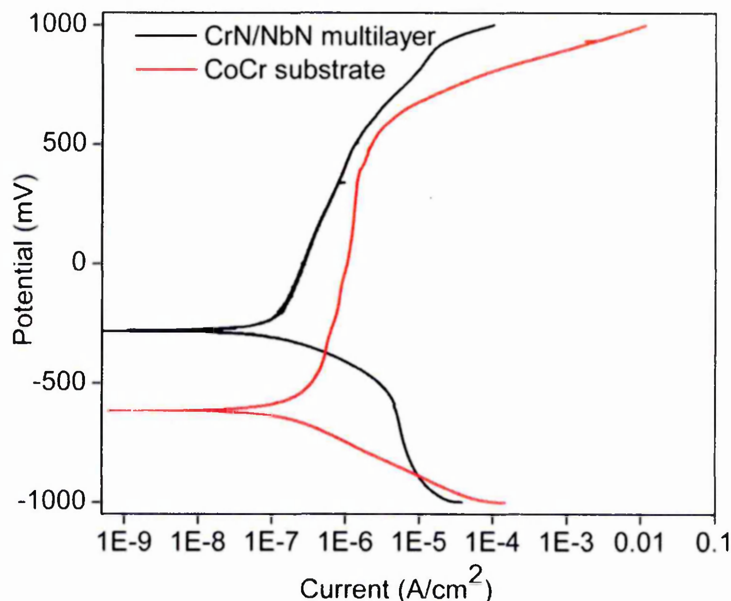

Figure 4.52 Potentiodynamic polarization curves of CoCr substrate and CrN/NbN multilayer (2HIPIMS + 2UBM) coating

The E_{corr} value for CoCr was about - 530 mV. The E_{corr} value for the multilayer coating was located in the nobler region than the substrate; about - 284 mV. It can be clearly seen that the multilayer coating and the substrate showed passivation over a wide potential range. Notably, the thin film showed a wider passive region as compared to the substrate. In addition to a wider passive region the thin film showed a lower passive current. The high E_{corr}, wider passive region and lower corrosion currents emphasized the enhanced corrosion resistance of the CrN/NbN multilayer coatings than the substrate. This performance is attributed to the several interfaces that present in the multilayers and enhanced density due to HIPIMS as explained in Sec. 4.12.7. Moreover, the E_{corr} (- 284 mV) is much higher as compared with the E_{corr} value (- 600 mV) of the same coating deposited utilising 1HIPIMS + 3UBM source combination [29].

4.16 Summary of multilayer coatings

TiN/NbN and CrN/NbN multilayer coatings exhibited excellent adhesion to the substrate. Both of them can be classified as HF1 grade indentation without any cracks, delamination and spallation. In addition, the scratch test also revealed the superior adhesion strength of the coatings as no coating failure such as spallation of the coating was observed up to 100 N. The cross section SEM analysis demonstrated that TiN/NbN (1HIPIMS + 3UBM), TiCN/NbCN (1HIPIMS + 3UBM) and CrN/NbN (2HIPIMS + 2UBM) multilayer coatings exhibited smooth, wider columnar structure without any voided region along the column boundaries. This type of microstructure is attributed to enhancement in the adatom mobility due to the increased metal ion flux with sufficient energy provided by HIPIMS sources involved in the process. TiN/NbN (2HIPIMS + 2UBM), TiCN/NbCN (1HIPIMS + 3UBM) multilayer coatings showed moderate hardness values of 30 and 28 GPa, respectively. In contrast, CrN/NbN (2HIPIMS + 2UBM) multilayer coating exhibited the highest hardness of 40 GPa. The tribological studies revealed that both the TiN/NbN (1HIPIMS + 3UBM and 2HIPIMS + 2UBM) coatings showed the highest COF of about 1. However, the coefficient of friction of TiCN/NbCN and CrN/NbN was found to be 0.432 and 0.49, respectively. The decreased COW of TiN/NbN multilayer coatings grown using 1HIPIMS + 3UBM (1.08×10^{-14} $m^3N^{-1}m^{-1}$) and 2HIPIMS + 2UBM (9.09×10^{-15} $m^3N^{-1}m^{-1}$) revealed that the tribological properties of such coatings improved with increasing degree of HIPIMS utilisation. TiCN/NbCN (1HIPIMS + 3UBM) multilayer coating showed a coefficient of wear of 3.57×10^{-15} $m^3N^{-1}m^{-1}$. The COW of (2HIPIMS + 2UBM grown CrN/NbN multilayer coating was found to be 8.33×10^{-16} $m^3N^{-1}m^{-1}$. Potentiodynamic polarisation test of multilayer coatings showed that these coatings effectively protect the underlying substrates.

References

1. COMBADIERE, L. and MACHET, J. (1996). Study and control of both target-poisoning mechanisms and reactive phenomenon in reactive planar magnetron cathodic sputtering of TiN. *Surface and coatings technology,* **82** (1–2), 145-157.
2. VDI - Association of German Engineers Guideline (3198).
3. EHIASARIAN, A. P., et al. (2011). Influence of high power impulse magnetron sputtering plasma ionization on the microstructure of TiN thin films. *Journal of applied physics,* **109**, 104314.
4. EHIASARIAN, A. P., et al. (2004). Comparison of microstructure and mechanical properties of chromium nitride-based coatings deposited by high power impulse magnetron sputtering and by the combined steered cathodic arc/unbalanced magnetron technique. *Thin solid films,* **457** (2), 270-277.
5. ZHOU, Z., et al. (2007). The role of the tribofilm and roll-like debris in the wear of nanoscale nitride PVD coatings. *Wear,* **263** (7–12), 1328-1334.
6. EHIASARIAN, A. P., et al. (2003). High power pulsed magnetron sputtered CrN_x films. *Surface and coatings technology,* **163–164**, 267-272.
7. HÅKANSSON, G., et al. (1987). Microstructure and physical properties of polycrystalline metastable Ti0.5Al0.5N alloys grown by d.c. magnetron sputter deposition. *Thin solid films,* **153** (1–3), 55-65.
8. DAVIS, C. A. (1993). A simple model for the formation of compressive stress in thin films by ion bombardment. *Thin solid films,* **226** (1), 30-34.
9. ZHAO, J. P., et al. (1997). Overall energy model for preferred growth of TiN films during filtered arc deposition. *Journal of applied physics D,* **30,** 5-12.
10. MAHIEU, S. and DEPLA, D. (2009). Reactive sputter deposition of TiN layers: Modelling the growth by characterization of particle fluxes towards the substrate. *Journal of applied physics D,* **42,** 053002.

11. GALL, D., et al. (2003). Pathways of atomistic processes on TiN (001) and (111) surfaces during film growth: An ab initio study. *Journal of applied physics,* **93,** 9086.

12. MAHIEU, S., et al. (2006). Biaxial alignment in sputter deposited thin films. *Thin solid films,* **515** (4), 1229-1249.

13. PETROV, I., et al. (2003). Microstructural evolution during film growth. *Journal of vacuum science and technology A,* **21** (5), S117-S128.

14. PIIPPO, J., ELSENER, B. and BÖHNI, H. (1993). Electrochemical characterization of TiN coatings. *Surface and coatings technology,* **61** (1–3), 43-46.

15. AZUMI, Kazuhisa, et al. (1998). Characterization of anodic oxide film formed on TiN coating in neutral borate buffer solution. *Corrosion science,* **40** (8), 1363-1377.

16. RAMYA, S., et al. (2010). Laser Raman microscopic studies of passive films formed on type 316LN stainless steels during pitting in chloride solution. *Corrosion science,* **52** (6), 2114-2121.

17. CONSTABLE, C. P., YARWOOD, J. and MÜNZ, W. -D (1999). Raman microscopic studies of PVD hard coatings. *Surface and coatings technology,* **116–119,** 155-159.

18. BARSHILIA, Harish C., et al. (2006). Superhard nanocomposite coatings of TiN/Si_3N_4 prepared by reactive direct current unbalanced magnetron sputtering. *Surface and coatings technology,* **201** (1–2), 329-337.

19. WEI, Qing, et al. (2009). Facile synthesis of α-Fe_2O_3 nanostructured films with controlled morphology. *Materials transactions,* **50,** 1351-1354.

20. MASLAR, J. E., et al. (2001). In situ Raman spectroscopic investigation of chromium surfaces under hydrothermal conditions. *Applied surface science,* **180** (1–2), 102-118.

21. SOUSA, P. M., et al. (2005). Morphological and structural characterization of CrO2/Cr2O3 films grown by laser-CVD. *Applied surface science,* **247** (1–4), 423-428.

22. PETROV, I., et al. (1989). Microstructure modification of TiN by ion bombardment during reactive sputter deposition. *Thin solid films,* **169** (2), 299-314.

23. WANG, H. W., et al. (2000). The corrosion behaviour of macroparticle defects in arc bond-sputtered CrN/NbN superlattice coatings. *Surface and coatings technology,* **126** (2–3), 279-287.

24. LJUNGCRANTZ, H., et al. (1994). Microstructural investigation of droplets in arc-evaporated TiN films. *Surface and coatings technology,* **63** (1–2), 123-128.

25. CHOI, Hyun Chul, JUNG, Young Mee and KIM, Seung Bin (2005). Size effects in the Raman spectra of TiO2 nanoparticles. *Vibrational spectroscopy,* **37** (1), 33-38.

26. P. PADMAVATHY, et al. (2011). Structural and electrochemical impedance spectroscopic studies on reactive magnetron sputtered titanium oxynitride (TiON) thin films. *Journal of applied electrochemistry,* **41,** 751-756.

27. BULL, S. J., BHAT, D. G. and STAIA, M. H. (2003). Properties and performance of commercial TiCN coatings. Part 2: Tribological performance. *Surface and coatings technology,* **163–164,** 507-514.

28. HOVSEPIAN, P. Eh, EHIASARIAN, A. P. and RATAYSKI, U. (2009). CrAlYCN/CrCN nanoscale multilayer PVD coatings deposited by the combined high power impulse magnetron Sputtering/Unbalanced magnetron sputtering

(HIPIMS/UBM) technology. Surface and coatings technology, 203 (9), 1237-1243.

29. PURANDARE, Y. P., STACK, M. M. and HOVSEPIAN, P. Eh (2006). Velocity effects on erosion–corrosion of CrN/NbN "superlattice" PVD coatings. *Surface and coatings technology,* **201** (1–2), 361-370.

Chapter 5

5 Conclusions

In this work, the effect of degree of HIPIMS utilisation on the plasma chemistry, microstructure, adhesion strength, nano hardness, tribological properties such as coefficient of friction and coefficient of wear and corrosion resistance of TiN, TiN/NbN, TiCN/NbCN and CrN/NbN was investigated. The following are the important conclusions that are drawn from this work.

- OES analysis revealed that the ratio $\{Ti^{1+}\}:\{Ti^{0}\}$ increased with increasing degree of HIPIMS utilisation as follows: pure UBM : 0.19, 1HIPIMS + 3UBM : 0.98, 2HIPIMS + 2UBM : 1.95 and pure HIPIMS : 3.54. The pure HIPIMS process generated a factor of ~ 19 higher metal ionisation ratio than the pure UBM process. This increase is related to the increased production of Ti^{1+} ions in the high peak power HIPIMS process.
- OES analysis carried out at different coil currents revealed that for pure UBM, the coil current showed negligible effect on $\{Ti^{1+}\}$ as fewer Ti^{1+} ions were produced as compared to Ti^{0} neutrals. For 1HIPIMS + 3UBM, 2HIPIMS + 2UBM and pure HIPIMS source combinations, the ratio $\{Ti^{1+}\}:\{Ti^{0}\}$ increased with increasing coil currents. However, in pure HIPIMS (2 HIPIMS), the change in $\{Ti^{1+}\}:\{Ti^{0}\}$ for coil currents above 3.5 A was negligible which could be due to reduced number of sources used for this process.
- OES analysis carried out with various nitrogen flows showed that the emission intensities of Ti^{0} and Ti^{1+} for all the source combinations decreased rapidly with increasing N_2 flow from 0 sccm to 120 sccm which can be attributed to the development of the target poisoning effect.

- EDX analysis of TiN coatings showed prominent peaks for Ti and N. The composition of the coatings was almost similar (near-stoichiometric) within the error of the measurement. However, TiN coatings grown by pure HIPIMS technique were over-stoichiometric with N: Ti ~ 1.5. EDX analysis of TiN/NbN, TiCN/NbCN and CrN/NbN coatings showed well defined peaks for constituent elements of such coatings.
- The deposition rate of TiN coatings increased with increasing degree of HIPIMS utilisation, as follows: pure UBM: 13.81 nm/min, 1HIPIMS + 3UBM: 13.62 nm/min, 2HIPIMS + 2UBM: 13.62 nm/min, pure HIPIMS (2 HIPIMS): 3.8 and 4 HIPIMS (extrapolated): 7.6 nm/min. These experiments clearly demonstrate that the combined HIPIMS/UBM processes bear a high potential for improved productivity. Furthermore, if followed, this approach might lead to a reasonable reduction of hardware costs as high quality coatings could be produced with smaller number of HIPIMS sources involved in the process provided that they deliver the necessary high plasma ionisation.
- Rockwell indentation test revealed that the TiN coatings deposited using four different source combinations and multilayer coatings exhibited superior adhesion (grade HF1). In addition, the scratch test revealed that such coatings exhibited excellent adhesion as no coating failures such as cracks, spallation and delamination were observed up to 100 N load.
- The nanohardness of TiN coatings increased with increasing degree of HIPIMS utilisation. The hardness of pure UBM, 1HIPIMS + 3UBM, 2HIPIMS + 2UBM and pure HIPIMS grown TiN coatings is as follows: 36, 38, 36 and 44 GPa, respectively. The hardness of TiN/NbN (1HIPIMS + 3UBM), TiN/NbN (2HIPIMS + 2UBM), TiCN/NbCN (1HIPIMS + 3UBM) and CrN/NbN (2HIPIMS + 2UBM) is 27, 30, 28 and 40 GPa, respectively.

- The tribological properties of the TiN and multilayer coatings improved with increasing degree of HIPIMS contribution. The COF and COW of TiN coatings were found to be decreased with increasing degree of HIPIMS utilisation. These results demonstrated enhancement in the tribological properties.
- The structural density of the coatings increased with increasing degree of HIPIMS utilisation. TiN and multilayer coatings deposited using 2HIPIMS + 2UBM and pure HIPIMS source combination showed a highly dense columnar microstructure with smooth column tops without any intercolumnar voids as compared to pure UBM and 1HIPIMS + 3UBM coatings.
- The residual stress in the coatings was found to be increased with increasing degree of HIPIMS utilisation, bias voltage and coil current. The combination of 2HIPIMS + 2UBM appears to be the most advantageous in this research as this provides a large bias voltage range where relatively low stress (σ = - 3.6 GPa) and highly dense [Fig. 4.11 (c)] coatings can be produced at reasonably high deposition rates. This is believed to be due to the optimal $\{Ti^{1+}\}$:$\{Ti^{0}\}$, 1.95 achieved with the process.
- TiN coatings exhibited a strong [111] preferred orientation with a small volume fraction of [200], [220] and [311] grains. Moderate [222] texture (second order reflection from the plane [111]) was also found. The volume fraction of [200] orientation increased with increasing bias voltage (ion energy) for the four combinations which is consistent with those published elsewhere in the literature.
- The surface roughness values that the surface roughness improved with increasing degree of HIPIMS contribution in the process. Plan-view SEM images of the coatings also confirmed the same.

- The corrosion resistance of the TiN coatings and multilayer coatings increased with increasing degree of HIPIMS utilisation. The E_{corr} value of TiN coatings increased with increasing degree of HIPIMS utilisation. However, the E_{corr} value of 2HIPIMS + 2UBM source combination was slightly higher than that of the pure HIPIMS coating. The E_{corr} value of pure UBM, 1HIPIMS + 3UBM, 2HIPIMS + 2UBM and pure HIPIMS grown TiN coatings was found to be - 391, - 348, + 305 and + 282 mV, respectively.
- Potentiodynamic polarisation test of TiN/NbN (1HIPIMS + 3UBM), TiCN/NbCN (1HIPIMS + 3UBM) and CrN/NbN (2HIPIMS + 2UBM) multilayer coatings revealed that the E_{corr} of such coatings was much higher compared to the CoCr substrate. The E_{corr} value of CoCr substrate, TiN/NbN (1HIPIMS + 3UBM), TiCN/NbCN (1HIPIMS + 3UBM) and CrN/NbN (2HIPIMS + 2UBM) coatings was found to be - 530, - 365, - 500 and - 284 mV, respectively. The enhanced E_{corr} values demonstrated the excellent corrosion resistance of multilayer coatings as compared to the substrate.
- Plan-view SEM images of corroded samples showed that the pitting corrosion was aggressive in pure UBM and 1HIPIMS + 3UBM grown TiN coatings as compared with 2HIPIMS + 2UBM and pure HIPIMS coatings.
- Raman analysis of as-deposited and corroded pure UBM grown TiN coating exhibited characteristic peaks for corrosion products such as Fe_2O_3 and Cr_2O_3 due to the substrate corrosion. In contrast, Raman spectra of as deposited and corroded TiN coating deposited by 1HIPIMS + 3UBM, 2HIPIMS + 2UBM and pure HIPIMS source combination exactly overlapped each other without any intensity change and without any peaks for corrosion products due to the substrate corrosion. These results together with E_{corr} values confirmed that the HIPIMS utilisation improves the corrosion resistance of the coatings.

- The droplets present in TiN (arc) coating deteriorated the corrosion performance of the coating. The corrosion resistance of the 2HIPIMS + 2UBM grown TiN coating was higher as compared to the TiN (arc) coating. Raman analysis of such coatings showed that the droplet free TiN coating (2HIPIMS + 2UBM) was not affected by the corrosion and the droplets in TiN (arc) coating underwent aggressive corrosion.
- The cross-section TEM analysis of pure HIPIMS grown TiN coating showed that the coating was extremely dense without any voids and pronounced column boundaries. This coating densification can be attributed to high energy ion irradiation which enhances adatom mobility during the initial nucleation of the films.

Finally, it can be concluded that CrN/NbN deposited using the 2HIPIMS + 2UBM source combination may be used as protective layer on knee implants. However, it is subject to further wear test using knee joint wear simulator, etc. Moreover, these coatings will perform even better when pure HIPIMS is used for the deposition. But the source combination should be decided considering other factors such as the deposition rate.

Future work

- Investigation of the effect of degree of HIPIMS utilisation on the microstructure of TiN coatings using TEM.
- Microstructural investigation of TiN/NbN, TiCN/NbCN and CrN/NbN multilayer coatings using TEM.
- Deposition of the above mentioned multilayer coatings on knee implants using HIPIMS.
- Characterisation of multilayer coatings deposited on knee implants.

Scientific Contributions

Publications

- Effect of the Degree of HIPIMS Utilisation on the Structure and Properties of TiN Films, Thin Solid Films, 562, 2014, 132-139.
- Effect of the Degree of HIPIMS Utilisation on the Corrosion Properties of TiN Films, 56th SVC Annual Technical Conference Proceedings, Providence, USA, 20 – 25 April 2013.
- High Performance Duplex Coatings for PEMFC metallic Bipolar Plates by CFUBMSIP and HIPIMS Technology, 40th International Conference on Metallurgical Coatings & Thin Films Proceedings, San Diego, USA, 29th April–3rd May 2013.

Presentations (Oral and Poster)

- Presented a poster on the **" Corrosion Properties of TiN Thin Films Grown by Combined HIPIMS/DCMS and Arc Evaporation Techniques"** at 5th International Conference on Fundamentals and Industrial Applications of HIPIMS 2014 held in UK.
- Received a **"Student Sponsorship Award"** to present an oral talk on the **"Effect of the Degree of HIPIMS Utilisation on the Corrosion Properties of TiN Films"** at 56th Annual SVC Technical Conference - 2013 held at Rhode Island, Providence, USA.
- Presented a poster on the **"Effect of the Degree of HIPIMS Utilisation on the Structure and Properties of TiN Films"** at 13th International Conference on Plasma Surface Engineering - 2012 held in Germany.